Hierarchical Hydrogen Storage in Clathrates of Ammonia Borane. Theoretical Study.

Alexander Viktorovich Abramov

Submitted for the degree of Doctor of Philosophy

Heriot-Watt University
School of Engineering and Physical Sciences – Chemistry
April 2010

Abstract

A brief overview of the dissertation given in this abstract is divided into five points showing its topicality, objective, goals, scientific novelty, and practical significance.

The topicality is reflected in a need for the replacement of the fossil fuels driven economy with economy oriented towards renewable sources of energy, in which hydrogen is used as an energy carrier. This need is dictated by three reasons: (i) ecological problems mostly induced by the carbon dioxide emission; (ii) limitedness of the reserves of hydrocarbons; (iii) political issues related to the localization of hydrocarbons in few places around the globe. In any implementation of hydrogen economy, which is a possible cure for the mentioned issues, the production and storage of hydrogen are the most challenging tasks to solve. The dissertation is focused on the problem of hydrogen storage. For today, none of the known materials meets all the requirements imposed on practical on-board hydrogen storage media.

The main idea proposed and explored in this dissertation is the "hierarchical storage of hydrogen". We envisage materials that would offer various means of reversible hydrogen binding. Each level of hydrogen storage would have different characteristics that become advantageous in different circumstances. A material with hierarchical hydrogen storage could be superior in comparison with conventional materials, in which hydrogen is bound at one level only. In particular, we explore materials in which a fraction of hydrogen is physically bound and the remaining part is chemically bound. The physical binding provides hydrogen that is kinetically easily accessible, whereas the chemical binding assures a high overall hydrogen density. We suggest that hydrogen clathrates of a high hydrogen content material, like ammonia borane, could serve as models of hierarchical hydrogen storage.

An objective of the dissertation is thus to validate the possibility of storage of molecular hydrogen in clathrates of ammonia borane using methods of theoretical chemistry and materials science.

The goals of the dissertation can be formulated as follows: (i) to identify possible structures of clathrates of ammonia borane; (ii) to estimate hydrogen capacity of the clathrates; (iii) to estimate pressure-temperature regimes required for the stabilization of these clathrates.

The scientific novelty of the dissertation includes: (i) formulation of the "hierarchical hydrogen storage" concept; (ii) formulation of construction principles for clathrates of ammonia borane and identification of their possible structures; (iii) estimation of hydrogen capacity of the clathrates; (iv) development of a model of clathrates phase equilibria, which is based on the energy of intermolecular host-guest interactions and the entropy of guest molecules enclosed in clathrate cages; (v) an estimation of the pressure-temperature stability zone for these clathrates.

The practical significance of the dissertation is in justification of further experimental works on clathrates of ammonia borane, for which the required stabilization pressure and temperature conditions are determined.

The work proposed and thoroughly explored hierarchical method of hydrogen storage and resulted in identification of stable cages and periodic structures of possible clathrates of ammonia borane. The most stable extended system of these clathrates was found to be more stable than molecular crystal of ammonia borane at low temperatures. Hydrogen capacity of this hypothetical clathrate structure was estimated to be 21 wt%. To predict the pressure-temperature stability zone of the material a model of clathrate phase equilibria has been formulated and tested on known hydrates. The model showed that clathrates of ammonia borane could be stabilized at ambient pressure when temperature is lowered to 77 K.

To whom it may concern.

Acknowledgments

I would like to acknowledge support of my supervisor Prof. Maciej Gutowski throughout the course of implementation of this work. I gratefully thank Dr. Garold Murdachaew for valuable help with the Symmetry-Adapted Perturbation Theory code. I express my deep thankfulness to Dr. Gregory Schenter for the velocity autocorrelation function construction and the Fourier transform codes. I appreciate explicit and implicit influence of other people with whom I interacted over the past three years and beyond.

Financial support for this project has been provided by the Marie Curie Actions. A portion of the computational work has been done on supercomputers of the Environmental Molecular Sciences Laboratory, a US national scientific user facility sponsored by the US Department of Energy's Office of Biological and Environmental Research and located at the Pacific Northwest National Laboratory.

Contents

List of Tables

List of Figures

List of Abbreviations

2,2,3-TMB	2,2,3-Trimethylbutane
AB	Ammonia Borane, NH_3BH_3
B3LYP	Becke 3-parameter exchange, Lee, Yang and Parr correlation
BP86	Becke exchange, Perdew 1986 correlation
BSSE	Basis Set Superposition Error
CC	Coupled Cluster
CCH	Cantitruncated Cubic Honeycomb
CCSD	Coupled Cluster method with Single and Double cluster amplitudes
CCSD(T)	Coupled Cluster method with Single, Double and non-iterative Triple cluster amplitudes
CHSM	Chemical Hydrogen Storage Medium
DFT	Density Functional Theory
DFT-D	Density Functional Theory with empirical Dispersion corrections
DOE	US Department of Energy
DZP	Double Zeta Polarized
GGA	Generalized Gradient Approximation
GTO	Gaussian-Type Orbital
HF	Hartree-Fock
HK	Hohenberg-Kohn
ISO	International Organization for Standardization
IPHE	International Partnership for the Hydrogen Economy
KS	Kohn-Sham

LDA	Local Density Approximation
MCH	Methylcyclohexane
MOF	Metal-Organic Framework
MP	Møller-Plesset
MTBE	Methyl Tert-Butyl Ether
NSHF	Not Shared Hexagonal Faces
NSOTF	Not Shared Octagonal and Tetragonal Faces
NSTF	Not Shared Tetragonal Faces
NSTFE	Not Shared Tetragonal Faces and Edges
OCH	Omnitruncated Cubic Honeycomb
PA	Proton Acceptor
PBE	Perdew-Burke-Ernzerhof exchange and correlation
PD	Proton Donor
PEM	Polymer Electrolyte Membrane
PT	Pressure-Temperature
SAPT	Symmetry-Adapted Perturbation Theory
SCF	Self-Consistent Field
SHF	Shared Hexagonal Faces
SIESTA	Spanish Initiative for Electronic Simulations with Thousands of Atoms
STO	Slater-Type Orbital
SWNT	Single Wall Carbon Nanotube
TBAB	Tetra-n-Butylammonium Bromide
THF	Tetrahydrofuran
VASP	Vienna *Ab-Initio* Simulation Package

Chapter 1

Introduction

1.1 Hydrogen Economy and Hydrogen Storage

To undermine dependence on fossil fuels and to eliminate anthropological emission of carbon dioxide and other pollutants a concept of hydrogen economy was proposed, see for example [1, 2]. Within the concept molecular hydrogen is used as an energy carrier and one of the most difficult technological bottlenecks in implementation of hydrogen economy, the problem of hydrogen storage, arises from the physical properties of molecular hydrogen. The gas is characterized by very weak intermolecular interactions and thus is very bulky even under extreme conditions of pressure and temperature. The problem is further complicated by the fact that the dependence on liquid hydrocarbons mostly results from transportation. The transportation sector consumes about 30% of the total energy production and about 70% of produced oil [3, p. B-59]. The need for on-board storage results in additional constrains on volume of storage tanks due to limited space available on a car. Automotive industry has set up hydrogen storage targets required to be satisfied in order not to change significantly the design of modern cars. Among the most important targets are volumetric and gravimetric densities of hydrogen to be contained in a storage system (targets for storage material itself are thus more demanding) which are 81 g/L and 9 wt%[1], respectively [4]. These targets are expected to be satisfied by 2015. If we compare what is desired with what pure hydrogen could offer in compressed, 40 g/L at 700 bar, or liquefied, 70 g/L at 20 K, forms [5], we arrive at the conclusion that the storage problem could only be solved with hydrogen engaged in stronger interactions, for example being chemically bound in materials. Moreover, storage of hydrogen in its pure form is also unsafe due to the possibility of formation of an explosive mixture with oxygen. A safe and efficient way of hydrogen storage has become an actual topic of current research in many groups around the world [6, 7].

[1]Here and further on, if not stated otherwise gravimetric and volumetric densities are given for hydrogen.

In addition to physical storage options, the above mentioned pressurization or liquefaction, which are accompanied with significant energy losses, there are essentially two technics to store hydrogen in materials: (i) physisorption using materials with very high specific surface area and (ii) storing hydrogen chemically bound in metal hydrides or other chemical compounds. The first type of materials can be represented by carbon nanotubes [8], Metal-Organic Frameworks (MOFs) [8, 9], and hydrogen hydrates [10]. This option offers reversible storage and fast hydrogen release but hydrogen uptake at ambient temperature is very low (about 1 wt%). A reasonable capacity is achieved under cryogenic conditions and elevated pressure only (6–7.5 wt% at 77 K and 30–40 bar). Metal hydrides [11, 12, 13], on the other hand, offer high hydrogen density (10.5 wt% for $LiAlH_4$) but the temperatures required for hydrogen release are high (more than 385°C for complete dehydrogenation of $LiAlH_4$ and more than 300°C for MgH_2) and the relase is slow. Thus physical (weak) binding (MOFs, carbon nanotubes, hydrates) provides poor gravimetric and volumetric density but hydrogen is easily accessible, while chemical (strong) binding, e.g. metal hydrides, is characterized by high hydrogen density but slow kinetics. Obviously, the goal is to identify materials with high hydrogen density *and* fast kinetics.

Among the materials which bind hydrogen chemically, Ammonia Borane, NH_3BH_3 (AB) looks particularly attractive from the gravimetric and volumetric points of view with the hydrogen density of 19.6 wt% and 150 g/L, respectively [14]. AB is a very unique material. On one hand it is isoelectronic with ethane which, in principle, could mean similar properties. On the other hand, unlike to ethane, it forms of solid under normal conditions. The stronger intermolecular interactions between AB molecules result from a difference in electronegativity between B and N. In consequence, the AB molecules are quite polar (dipole moment is 5.216 D [15]), and so called intermolecular dihydrogen bonds [16] stabilize the crystal of AB. AB is water and air stable, which are desirable properties. Unfortunately, it releases hydrogen slowly at temperatures below 85°C. The release at this temperature would be suitable for utilization of heat generated by Polymer Electrolyte Membranes (PEMs) of the fuel cells. Significant effort has been devoted to improve kinetics of hydrogen release from AB in the desirable temperature range. The dehydrogenation reaction has been catalyzed with the pincer-type diphosphinito complexes of iridium in Tetrahydrofuran (THF) solution of AB [17]. One equivalent of hydrogen has been released in 14 min with 0.5 mol% concentration of the catalyst at room temperature, which is considered to be unprecedented rate. Other method of improving kinetics of hydrogen release from AB is to replace organic solvents with ionic liquids. In [18] 1-butyl-3-methylimidazolium chloride was shown to suppress the induction period and significantly accelerate hydrogen release in comparison with solid ammonia borane. Improvement of reaction kinetics could also be achieved by loading AB

into mesoporous silica [19]. Another approach, explored in this dissertation, is to design new materials based on AB, in which at least a part of the stored hydrogen is kinetically easily accessible. This hydrogen would be in molecular form and its accessibility would result from weak binding forces like those present in clathrates.

1.2 Overview of Clathrate Materials

The combination of weak and strong forces binding hydrogen in one material is known in nature [20]. Hydrogen clathrates of water have molecular hydrogen enclosed in water cages, while other hydrogen atoms are constituents of water molecules. The latter hydrogen is not accessible in on-board applications due to unfavourable thermodynamics. This deficiency could be removed by replacing water with another host material. The desirable host material should by itself be a medium for hydrogen storage. In addition, it should have an ability to form hydrogen or dihydrogen bonds in order to assemble itself into extended clathrate frameworks. Both required characteristics are fulfilled by AB making it an interesting candidate for a host in clathrates. This reasoning leads to the central questions addressed in this dissertation:

1. Are hydrogen clathrates of ammonia borane feasible?

2. Under which conditions could they exist?

In general, clathrates are solid materials constituting of two or more compounds bound together by non-covalent interactions such as hydrogen bonding or van der Waals forces. These host-guest combinations have been known for about 200 years. Clathrates made of water are called hydrates and were described in 1811 by Sir Humphry Davy [21] with chlorine as a guest molecule. The composition of these compounds was originally determined by Michael Faraday in 1823 [22]. Even earlier reports on inclusion compounds may be found in literature. According to [23] it was Priestley who in 1777 had an honour to observe "anomalous ice" existing at positive temperatures. These materials, which initially were considered as esoteric, eventually received deserved attention from industry and scientific community. They became tightly bound with the energy future of humankind. Gas hydrates were widely studied during the previous century mainly because of their implications in petroleum and petrochemical industry [24, 25]. Gas hydrates create serious problems when they are formed in pipelines or equipment as they clog them. On the other hand, these found in permafrost regions or on seabed are abundant sources of natural gas. A significant breakthrough in clathrate chemistry has been made in 1948 by H. Powell [26], who determined structures and established terminology. In 1999 hydrogen hydrates were discovered [20, 10]. Along with the fact that guest

molecules could form clusters this discovery showed that clathrates could play a role of hydrogen storage media.

Because of the abundance of gas hydrates the term clathrates is strongly linked with water. It is well known that water is in possession of many interesting properties, it has an unusually high melting point, unusually high viscosity, high heat of vaporization, it shrinks on melting, and others [27], but an ability to form clathrates is not limited to water. For example the following materials are known to act as host species: hydroquinone [28, 29, 30, 31], Hofmann's compounds [32], and Dianin's compounds [33, 34]. Intermolecular interactions are critical to the stability of clathrates. They are responsible for the formation of cages from the host species, and they contribute through host-guest interactions to the stability of these low-density materials.

For the relevant to this work case of hydrogen clathrates, the presence of chemically and physically bound hydrogen in one material gives rise to storage hierarchy. The new type of clathrates, where the host material is chosen as a hydrogen storage material, offers a possible solution to the challenge of the hydrogen storage. In a concept of hierarchical hydrogen storage we suggest clathrates, in which the host component contains chemically accessible hydrogen whereas molecular hydrogen acts as the guest component. In this work we implement the concept using AB as the host component and we verify feasibility of the concept using theoretical methods.

1.3 Layout of Dissertation

The dissertation is organized as follows. It contains nine chapters and four appendices. The first chapter introduces the concept of hydrogen economy and the challenge of hydrogen storage, and develops a concept of hierarchical hydrogen storage that leads to a hybrid material, which contains both weakly and strongly bound hydrogen. The literature review is given in the second and the third chapters. The second chapter covers most of the hydrogen storage methodologies currently known. The third chapter gives a detailed overview of clathrate materials with special emphasis on hydrates. It covers experimental and theoretical studies. In this chapter we also show that the known statistical model of hydrate phase equilibria is not applicable to hydrogen hydrates and hydrogen clathrates in general. The fourth chapter describes and substantiates theoretical and computational methods of chemistry and materials science used in the work. In chapters five to eight original results on possible structures of clathrates of AB are reported and a statistical model of clathrate phase equilibria, which takes into account quantum effects experienced by guest molecules entrapped in nanosize cages of host molecules, is summarized. In chapter five we formulate a concept of hierarchical hydrogen storage and we eval-

uate the suitability of AB to act as a host in hydrogen clathrates. In chapter six we formulate construction principles for clathrates of AB and we identify stable cages. We also estimate hydrogen capacity of these cages. In chapter seven we identify and explore periodic structures of clathrates of AB and estimate their hydrogen capacity. In chapter eight we develop a statistical model of clathrate phase equilibria. The model is then tested on known hydrates and applied to clathrates of AB to estimate their pressure-temperature stability zone. In chapter nine we summarize the work and give conclusions.

Chapter 2

Hydrogen Storage Methodologies

2.1 Desirable Hydrogen Storage Targets

In a book "The Mysterious Island", published in 1874, Jules Verne in words of an engineer Cyrus Smith predicts that water will be the coal of the future. To our best knowledge this may be considered as the first written formulation of the idea of hydrogen economy. It took more than one hundred years to realize that this idea requires further study. Nowadays hydrogen programs exist in many countries including Iceland, Switzerland, France, Germany, United Kingdom, United States, Russia, and many others which form the so-called International Partnership for the Hydrogen Economy (IPHE). Massively financed systematic research towards practical implementation of hydrogen economy with a rigorous set of goals was initiated by a US President in 2003. This research was headed for targets formulated by the US Department of Energy (DOE) on the basis of automotive industry wishes. The targets are comprehensive and include several requirements for on-board hydrogen storage systems such as gravimetric capacity, volumetric capacity, cost, durability/operability, charging/discharging rates, fuel purity, environmental health and safety [4]. The most important targets are summarized here:

- By 2010, develop and verify on-board hydrogen storage systems achieving 2 kWh/kg (6 wt%), 1.5 kWh/L (45 g/L), and $4/kWh;
- By 2015, develop and verify on-board hydrogen storage systems achieving 3 kWh/kg (9 wt%), 2.7 kWh/L (81 g/L), and $2/kWh.

These goals are for an overall on-board storage system including supplementary equipment. The storage medium itself ought to provide better characteristics. Among the most crucial qualities of a storage medium are gravimetric and volumetric densities of hydrogen, which means that in developments of new storage materials it is desirable to exceed 9 wt% and 81 g/L.

2.2 High Pressure and Cryogenic Tanks

Traditional methods of dealing with gases in order to increase density are not efficient for hydrogen due to its very weak intermolecular interactions. Hydrogen remains in gas phase down to temperature of 20 K [5]. In consequence of weak intermolecular interactions extreme physical conditions are required for compression or liquefaction [35], and special materials and technologies have to be used to withstand high pressures or/and low temperatures [36]. High pressure tanks made of composite materials based on carbon fibres have been developed, which can withstand pressure up to 700 bar [37]. Despite of usage of expensive composites these tanks and accompanying equipment are heavy, bulky, and intrinsically unsafe. Among other drawbacks of this technology are insufficient energy density (less than 1.5 kWh/kg [37]) and high cost (around \$18/kWh [4]; for a comparison for chemical hydrides the cost is \$5–\$8/kWh).

The density of gaseous hydrogen can also be improved by its condensation but because of the low required temperature the liquefaction of hydrogen is coupled with an energy penalty of around 30% of its lower heating value [4]. Moreover, the most common approach to support a cryogenic temperature of liquefied hydrogen is its own evaporation, which is realized through constant boil-off of the gas. The boil-off losses may be reduced to some extent by a hybrid technology based on cryo-compressed tanks [38, 39]. Still, at the current level of technological development, hydrogen storage capacity of pressurized and cryogenic tanks is in a range 3.4–4.7 wt% and 14–28 g/L [4], thus much lower than the DOE targets.

2.3 Solid State and Liquid Materials

2.3.1 Metal Hydrides

Storage of hydrogen in metal hydrides is promising in terms of gravimetric and volumetric density. Its on-board application engenders engineering challenges related to thermal management during charging and discharging processes. On the basis of the enthalpy change ($\triangle H$) of the refueling reaction $M + H_2 \rightarrow MH_2$, storage options may be subdivided into on-board and off-board regenerable [7]. When $\triangle H$ is in a range –(20–25) kJ/mol H_2 the regeneration is easily done. When $\triangle H$ exceeds –(60–100) kJ/mol H_2 the regeneration can only be done off-board. The intermediate interval –(25–60) kJ/mol H_2, which is typical for many metal hydrogen systems, requires high-performance heat exchangers that would add to the weight of the storage system. Apart from thermal management issues, hydrogen storage materials should work in a certain range of pressure 1–10 atm and temperature 25–120°C dictated by operating conditions of PEM fuel cells [7]. More practical upper limit for the temperature range is even lower, about 70°C [36]. In addition, gravimetric density

requirements must be fulfilled which exclude from consideration simple interstitial metal hydrides like FeTiH [40] and $LaNi_5H_6$ [41] and limits available options to hydrides of metals from the first three periods of the periodic table. For $LaNi_5H_6$ the gravimetric density is not the only limitation. The cost of La, \$5/g [42], is far too high for mass automotive applications.

Other metal hydrides with theoretically high hydrogen capacity are lithium tetrahydridoaluminate ($LiAlH_4$) [6, 11, 43], sodium tetrahydridoaluminate ($NaAlH_4$) [11, 43, 44], sodium tetrahydridoborate ($NaBH_4$) [7, 45, 46], mixture of lithium tetrahydridoborate ($LiBH_4$) [47] and magnesium dihydride (MgH_2) [13], and aluminium trihydride (AlH_3) [48].

The dehydrogenation of aluminum hydrides typically occurs in a three step mechanism [6]. High temperatures of hydrogen release and poor kinetics may be suppressed when materials are catalyzed by Ti dopants [43]. $LiAlH_4$ is metastable at room temperature and upon heating it decomposes in three steps, as shown in equation 2.1.

$$\begin{aligned} 3LiAlH_4 &\rightarrow Li_3AlH_6 + 2Al + 3H_2, \\ Li_3AlH_6 &\rightarrow 3LiH + Al + \frac{3}{2}H_2, \\ 3LiH &\rightarrow 3Li + \frac{3}{2}H_2 \end{aligned} \tag{2.1}$$

The temperature measured to complete the second step was 200°C [11]. The total amount of hydrogen released over the first two steps was 7.9 wt%. Due to an unfavorably high equilibrium pressure of hydrogen, even at room temperature, spent $LiAlH_4$ cannot be regenerated. Its sodium analog undergoes dehydrogenation according to a similar mechanism, equation 2.2.

$$\begin{aligned} 3NaAlH_4 &\leftrightarrow Na_3AlH_6 + 2Al + 3H_2, \\ Na_3AlH_6 &\leftrightarrow 3NaH + Al + \frac{3}{2}H_2, \\ 3NaH &\rightarrow 3Na + \frac{3}{2}H_2 \end{aligned} \tag{2.2}$$

The first two steps release 5.6 wt% of hydrogen at 280°C [11]. Doping with Ti improves kinetics of hydrogen release and reduces the dehydrogenation temperature down to 160–200°C [43, 44]. The rehydrogenation conditions for the doped material are 150 bar and 170°C. The temperatures required for dehydrogenation/ rehydrogenation of the doped material are still too high and the gravimetric density of hydrogen is too low for practical applications.

The direct thermal decomposition of sodium tetrahydridoborate according to a

reaction shown in equation 2.3 requires temperatures higher than 400°C [7].

$$NaBH_4 \rightarrow NaH + B + \frac{3}{2}H_2 \tag{2.3}$$

A hydrolysis reaction of the hydride with water may be used instead, equation 2.4.

$$NaBH_4 + 2H_2O \rightarrow NaBO_2 + 4H_2 \tag{2.4}$$

The reaction is controlled by pH and use of catalysts such as Ru or nickel-cobalt-boride [45]. A non-catalytic process is possible with application of steam [46]. One half of the released hydrogen is due to water and low concentrations of $NaBH_4$ are used to prevent precipitation of $NaBO_2$, which reduces the system storage capacity to 4 wt% [6]. Sodium metaborate $NaBO_2$ can only be regenerated off-board with required energy of 900 kJ/mol [6].

Partial dehydrogenation of $LiBH_4$ according to a reaction presented in equation 2.5 requires temperatures more than 400°C at 1 bar pressure [47].

$$LiBH_4 \rightarrow LiH + B + \frac{3}{2}H_2 \tag{2.5}$$

Addition of MgH_2 to $LiBH_4$ in the presence of $TiCl_3$ stabilizes the right side of the reaction, equation 2.5, or destabilizes its left side, and reduces the required temperature to 225°C at 1 bar pressure, equation 2.6 [47].

$$LiBH_4 + \frac{1}{2}MgH_2 \leftrightarrow LiH + \frac{1}{2}MgB_2 + 2H_2 \tag{2.6}$$

The reversible storage of 8–10 wt% of hydrogen has been demonstrated for this system, although, apart from poor kinetics, the decomposition temperature still remains too high for vehicular applications. Pure magnesium dihydride has also been studied as a hydrogen storage medium. It releases hydrogen slowly at temperatures larger than 300°C. It was shown that in nickel catalyzed MgH_2 faster release of hydrogen could be expected at about 160°C [13].

AlH_3 may be dehydrogenated by modest heating at temperature less than 200°C. It has been shown that the temperature may be tuned by particles size and by addition of LiH [48]. The desorption temperature may be lowered to 125°C and more than 7 wt% of hydrogen may be released below 175°C, although regeneration of spent material cannot be done on-board. Off-board regeneration involves organometallic synthesis which is too expensive for automotive applications [6].

Most hydrides with appreciable hydrogen density are thermodynamically stable at standard conditions and require temperatures more than 200°C to release hydrogen. Some metal hydrides, like AlH_3, are less stable, which creates problems with on-board regeneration. There are numerous issues with metal hydrides that have to be resolved before their practical usage as hydrogen storage media would become

possible. Lowering the dehydrogenation temperature and the amount of heat released during rehydrogenation, improving kinetics and hydrogen density are among the most crucial problems.

2.3.2 Ammonia Borane and Related Compounds

AB is a high capacity hydrogen storage material which is a solid at ambient conditions although it is isoelectronic with ethane, which is a gas. Melting point of the material is 114°C and the release of hydrogen at temperatures below 100°C is slow [19]. Without structural details, considering stoichiometry only, its thermal decomposition can be described by a three-step reaction, equation 2.7.

$$\begin{aligned} &NH_3BH_3 \rightarrow NH_2BH_2 + H_2, \\ &NH_2BH_2 \rightarrow NHBH + H_2, \\ &NHBH \rightarrow NB + H_2 \end{aligned} \tag{2.7}$$

The complete three-step decomposition results in 19.6 wt% of hydrogen released into the gas phase with the first two steps producing 13.1 wt%. The reaction rates and products formed depend on reaction conditions [15, 49, 50, 51]. If the structure of products is taken into account then the decomposition of AB may be thought to occur along two different routes: (i) "polymeric" and (ii) "cyclic". The products of the polymeric route are polymeric aminoborane $[\text{-}H_2N\text{-}BH_2\text{-}]_n$ (polyaminoborane), polymeric iminoborane $[\text{-}HN{=}BH\text{-}]_n$ (polyiminoborane), and cubic boron nitride (c-BN). The products of the cyclic route are cyclotriborazane ($H_6N_3B_3H_6$), borazine ($N_3B_3H_6$), and hexagonal boron nitride (h-BN). The dehydrogenation typically proceeds simultaneously along both routes and production of undesirable compounds like borazine and improvements in kinetics of hydrogen release may be achieved by appropriate tuning of the conditions. One example is thermolysis of ammonia borane contained within a mesoporous silica scaffold [19], where the hydrogen release was pushed to proceed along the preferred polymeric route and the required temperature was lowered to 80°C, although kinetics still remains an issue.

It should be emphasized that the dehydrogenation of AB is overall exothermic. Therefore the development of energy efficient regeneration methods of spent material is of critical importance [15]. In addition, improvements in kinetics of hydrogen release at working temperatures of PEM are required. The issue with kinetics of hydrogen release has already been addressed by a few groups. Significant progress has been made in catalytic release of H_2 from a THF solution of AB [17]. When the pincer-type diphosphinito complex of iridium in concentration of 0.5 mol% is used as the catalyst for the dehydrogenation reaction one equivalent of hydrogen is released in 14 min at room temperature. If concentration of the catalyst is increased to 1.0 mol% the same one equivalent of hydrogen is released in just 4 min. It was

also suggested to replace organic solvents with ionic liquids in order to improve kinetics of the dehydrogenation reaction [18]. An equal by weight mixture of 1-butyl-3-methylimidazolium chloride and AB releases one equivalent of hydrogen in about 3 hours when heated to 85°C. The same amount of hydrogen at the same temperature is released from solid AB in about 16 hours. Moreover, the induction period for hydrogen release is reduced from 3 hours for solid AB at 85°C to zero in the ionic liquid at the same temperature.

2.3.3 Organic Liquid Carrier

From a practical view point, a very attractive approach for hydrogen storage is to use an organic liquid carrier. The method has been investigated by Air Products and Chemicals, Inc. [52] and by other independent researchers [53]. The philosophy behind the approach is to remove spent (dehydrogenated) carrying liquid from a car and replace it with fresh (hydrogen-rich) carrier at a refueling station. The regeneration of spent carrier would be performed off-board. Molecular hydrogen is thus excluded from the supply chain and the existing petrol infrastructure can be utilized. Many candidates have been tested as possible liquid carriers with two being the most promising. The first, N-ethylcarbazole ($C_{14}H_{13}N$) could be hydrogenated catalytically to form perhydro-N-ethylcarbazole at 130–200°C and 35–83 bar. Hydrogen release is achieved upon heating to 200°C. Theoretical hydrogen capacity of the material is 5.7 wt% and 54 g/L. Performed cyclic studies demonstrated that little or no degeneration in the hydrogen capacity could be expected. The second liquid carrier, 4,7-phenanthroline ($C_{12}H_8N_2$) is hydrogenated to form perhydro-4,7-phenanthroline with a theoretical hydrogen capacity of 7.2 wt% and 69 g/L. A significant disadvantage of these liquid carriers is a relatively high dehydrogenation temperature of around 200°C.

2.3.4 Physisorption

High gravimetric capacities of metal hydrides and other materials mentioned so far are coupled with thermal management issues, elevated temperatures, and poor kinetics of hydrogen release. High surface area materials offer low binding energies (adsorption enthalpy is smaller than 10 kJ/mol H_2 [54]) and fast kinetics at the expense of low hydrogen capacity. Due to weak intermolecular interactions, formation of several layers of adsorbed hydrogen can only be expected at temperatures less than the critical point temperature of 33 K, where condensation of hydrogen can be observed [35]. At higher temperatures only a monolayer of adsorbed hydrogen should be expected. For a monolayer adsorption the amount of gas stored in a material is directly proportional to its specific surface area. Materials with high specific surface area considered as potential hydrogen storage media are nanoporous

activated carbons, carbon nanotubes, covalent-bonded graphenes, and MOFs.

Carbon-Based Microporous Materials

Nanoporous activated carbons are materials with a high specific surface area. For example, granular AX-21 has a specific surface of 2800 m^2/g and a density of 0.3 g/cc [8]. They may be steam or chemically activated in order to produce a very porous structure. More than 20 carbonaceous materials have been systematically studied at 77 K and 1 bar [55]. Apart from surface area, the amount of hydrogen stored was found to be dependent on size and volume of micropores. Wider pores are less favorable for hydrogen storage than smaller pores due to inability of hydrogen to form several layers at this temperature. Tuning the pore size and shape is considered to be a way to improve the hydrogen storage capacity of these materials, although there are natural limitations. An estimation of potential storage capacity of porous carbons, with the density of hydrogen in the pores approaching that of liquid hydrogen, shows that a maximum of about 8 wt% of excess hydrogen can be reached at 77 K and 40 bar and larger values are only achievable at lower temperatures [8].

Carbon nanotubes are allotropes of carbon. A Single Wall Carbon Nanotube (SWNT) is a one-atom thick sheet of graphite rolled up into a seamless cylinder with a diameter on the order of a nanometer. The ends of the cylinder are closed with fullerene like caps and an oxidative or ultrasonic treatment may be applied to open up the caps. There were controversial reports about the SWNTs hydrogen storage capacity up to 10 wt% at ambient conditions. Unfortunately these results could not be reproduced and were attributed to experimental difficulties [56, 54]. Under ambient conditions the amount of hydrogen adsorbed in SWNTs is less than 1 wt%, whereas at 77 K a value of 4.6 wt% can be obtained after acid and heat treatments. If pressure is risen further and the same cryogenic temperature is preserved values of 6 wt% at 2 atm and of 8 wt% at 40 atm could be reached [8].

Covalent-bonded graphenes are made of graphite sheets acting as walls for regular or irregular three dimensional structures, which resemble honeycombs. The sheets are bonded together to form stable porous 3D structures by means of sp^3 hybridized carbon atoms. The storage capacity of the pure and titanium decorated material was investigated theoretically [57, 58]. An estimated storage capacity reaching 4 wt% of hydrogen is not outstanding and the synthesis of the titanium decorated material has not been demonstrated yet.

A characteristic feature of the carbon-based microporous materials is that hydrogen density of around 8 wt% can only be achieved at elevated pressures up to 40 bar and at cryogenic temperatures of about 77 K. On the other hand, full reversibility and cyclic storage are among natural advantages. Despite of severe limitations, these porous materials deserve further studies, as recognized by some authors [54].

Metal-Organic Frameworks

MOFs are nanostructures of transition metals bridged by organic ligands. They are very strong competitors of other materials used to physisorb hydrogen [59]. MOFs also have very high specific surface areas (up to 6000 m^2/g [8]), but they are different from microporous carbons in the way that systematic strategies could be developed to design new materials [9, 59, 60]. In addition to appropriate porosity and pore size, impregnation, catenation, and open metal sites have been suggested as possible options for these strategies [9]. Impregnation is implemented by including large molecules such as C_{60} into MOFs in order to reduce free volume of the pores and introduce additional adsorptive sites. Catenation in form of interpenetration or interweaving of the frameworks leads to reduction of the free volume of the pores and could be used to tune this parameter to maximize hydrogen capacity. Open metal sites could be created by removing some of terminal ligands by heating. This might lead to a distortion of the framework or to a more profound rearrangement. Other possibilities available to adjust properties of MOFs to practical needs are the incorporation of light metals and functionalization of linkers [9].

With thousands of MOFs reported and only a fraction studied for the purpose of hydrogen adsorption, the area still remains in an early stage of development [54, 9]. The structural richness of MOFs creates a lot of space, in which the holy grail of hydrogen storage might be hidden. The limitations of MOFs are of the same nature as for other materials relying on physisorption of hydrogen, including porous carbons, and storage characteristics of MOFs are manifestation of this kinship. At 295 K a reversible hydrogen uptake of less than 1 wt% was demonstrated and the value increases to 6–7.5 wt% at 77 K and 30–40 bar [8]. The challenge is to demonstrate that the capacity achievable at a cryogenic temperature could be reached at ambient temperatures [54].

2.3.5 Other Materials

Materials, which potentially could be used as a hydrogen storage medium but have not been covered in previous sections or which have not found wide recognition due to low hydrogen density, improper operating conditions, high cost, hazard, or a combination of these factors, are receiving tribute in this section.

Ammonia (NH_3) could be used to store hydrogen chemically. Being a liquid already at -33°C at ambient pressure or at 25°C at 10 bar [61], it has a high hydrogen density by mass and volume (17.7 wt% and 108 g/L, respectively [62]). Among the reasons which stop it from becoming a very good hydrogen storage material are: energetically expensive production process, its toxicity to PEM fuel cells, and safety issues. Production of ammonia is accomplished over a surface of iron catalyst at temperatures 400-500°C and pressures above 100 bar, which implies a significant

energy cost of 1.5 GJ/t [62]. Ammonia cannot be used directly in low temperature fuel cells, such as PEM fuel cells, and its decomposition into hydrogen and nitrogen is needed. The reaction is equilibrium limited and traces of ammonia should be expected in the products. As ammonia reacts with an acidic electrolyte of PEM fuel cells, hydrogen feed to PEM fuel cells must not contain ammonia at concentrations more than 1 ppm to prevent deactivation of the electrolyte [62]. The International Organization for Standardization (ISO) dictates even a more strict limitation of 0.1 ppm [7]. Ammonia is harmful not only to fuel cells but also to humans and in addition to its toxicity it is explosive. It was proposed to use metal ammine complexes for safe storage of ammonia. The salt $Mg(NH_3)_6Cl_2$ could store 9.1 wt% of hydrogen reversibly, but requires a high temperature of 620 K to operate [63].

Other materials which share the same problem of ammonia contamination of hydrogen feed to fuel cells are amide/imide compounds of light elements. Two systems have been studied for the purpose of hydrogen storage Ca-N-H and Li-N-H, with the latter showing better characteristics [64]. At 285°C and atmospheric pressure, a reversible reaction, equation 2.8, has been observed, in which 6.5 wt% of hydrogen can be stored.

$$LiNH_2 + LiH \leftrightarrow Li_2NH + H_2 \tag{2.8}$$

It was also demonstrated that partial substitution of Li by Mg destabilizes lithium amide/hydride system and lowers the reaction temperature to 200°C [65]. In another reaction, equation 2.9, 4.5 wt% of hydrogen can be stored reversibly.

$$2LiNH_2 + MgH_2 \leftrightarrow Li_2Mg(NH)_2 + 2H_2 \tag{2.9}$$

Apart from ammonia contamination of hydrogen fuel, other deficiencies of amide-imide compounds are low hydrogen density, high temperature of hydrogen release, and low hydrogen pressure at working conditions of PEM fuel cells (less than 0.5 MPa) [6].

Reversible chemical storage of hydrogen can also be accomplished in phosphinoborane ($(C_6H_2Me_3)_2P(C_6F_4)B(C_6F_5)_2$, Me is methyl) which reacts with H_2 at 25°C and 1 atm to form $(C_6H_2Me_3)_2PH(C_6F_4)BH(C_6F_5)_2$. The latter compound looses hydrogen at temperatures above 100°C to form the initial material. A small hydrogen storage capacity of less than 0.25 wt% [66] and a high dehydrogenation temperature are the main limitations of the material.

Incorporation of transition metals into light weight materials is thought of as a method to increase hydrogen capacity. For example, a theoretical investigation of Ti-decorated cis-polyacetylene demonstrated that the material is capable to store reversibly 7.6 wt% of hydrogen at the conditions of adsorption and desorption of 30 atm, 25°C and 2 atm, 100°C, respectively [67]. Later on it was emphasized that

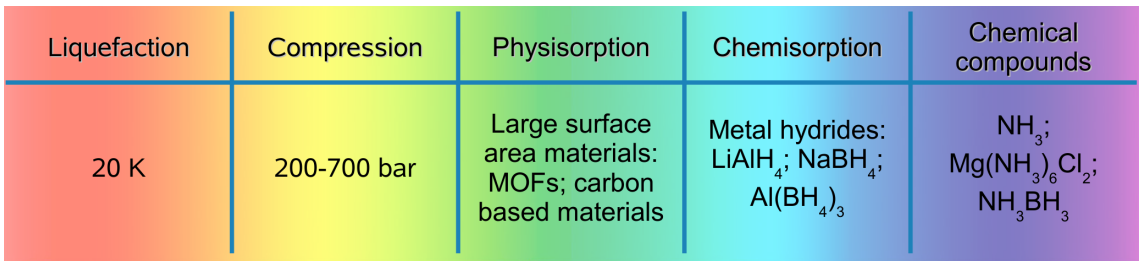

Figure 2.1: Quasicontinuous spectrum of hydrogen storage methodologies.

the Ti atoms in Ti-decorated cis-polyacetylene tend to form clusters, which reduces the predicted hydrogen storage capacity by more than 50% [68].

An intriguing hydrogen storage option was presented at the 13th annual Green Chemistry and Engineering Conference by Erman Senoz working in a group of professor Richard P. Wool at the University of Delaware. The researcher suggests to store molecular hydrogen in carbonized chicken feather fibers. When a protein keratin of the feathers is heated it forms cross-links increasing surface area. As a result of this structural change hydrogen capacity of the feathers could reach that of the carbon nanotubes.

The storage of hydrogen in hydrates is based on weak physical interactions between host and guest molecules. The stored hydrogen is kinetically easily accessible, but the material is stable only at extreme conditions and the hydrogen density is low. A detailed description of hydrate materials is given in the next chapter.

2.4 Conclusions

As of today, there are three main methodologies having potential to be used in practical applications to store hydrogen: (i) traditional physical methods such as compression and liquefaction; (ii) physisorption of hydrogen in materials with high specific surface area; (iii) storage of hydrogen in chemical compounds like metal hydrides or ammonia borane. These methodologies and representative compounds are summarized in a form of a quasicontinuous spectrum shown in figure 2.1. The left hand side and the central part of the spectrum corresponds to technologies (compression and liquefaction) and materials (high surface area materials) with easy access to stored hydrogen. This side is also characterized by low hydrogen density on storage system basis for technologies and on material basis for materials. The right hand side of the spectrum (chemisorption and chemical compounds) normally corresponds to materials with high hydrogen density (except for some interstitial hydrides) but with somewhat hindered access to stored hydrogen due to the need to overcome energy barriers in order to release stored hydrogen. It illustrates well the challenge of on-board hydrogen storage. The desirable material should display the kinetics of hydrogen release and uptake matching the left and central part of

the spectrum while the hydrogen density should be as high as on the right side of the spectrum. For the time being, such a material remains unknown. In the proceeding chapters we propose a family of compounds that might have these desirable properties. A particular attention is paid to clathrates built from ammonia borane frameworks and loaded with molecular hydrogen.

Chapter 3

Clathrate Materials

3.1 Historical Overview

An evidence of mentioning clathrates in literature dates back to 1777. Many outstanding chemists have been involved in studies of these materials including Priestley, Davy, Faraday, and le Chatelier [23]. Non-stoichiometric composition of these compounds and very long interatomic distances were difficult to reconcile with contemporary chemical theories. It was Herbert Powell who, when studying compounds of hydroquinone and small molecules (SO_2, H_2S, HCl, and some others), realized in 1948 [26] that the need for stoichiometry is not necessary for the stability of clathrates, because not all cavities are required to be filled. This conclusion came from understanding of supramolecular nature of the compounds, from a discovery that molecules of one type form a lattice, in which molecules of another type may be encapsulated. Structures of the materials were determined and organizational principles of the host and guest arrangements have been proposed. Powell showed that formation of clathrates is not based on conventional chemical bonds between guest and host molecules, but rather on proper matching in size and shape between guest molecules and cavities within the host structure. The name "clathrate", without which now we could not imagine the whole branch of supramolecular chemistry, was also thoughtfully selected by Professor Powell. The word reflects imprisonment of guest molecules in the host structure. A Latin word "clatratus" means closed or protected by the cross bars of trellis [69]. Many modern definitions of clathrates reflect this Latin meaning. The structural information encoded in the word "clathrate" normally implies formation of 3D cages of host lattice and one common name of clathrates are host-guest compounds or inclusion compounds. Clathrates may also be defined formally as solid materials constituting of two or more compounds bound together by non covalent interactions such as hydrogen bonding or van der Waals forces. Other species, called clathrates as well, are channel compounds (e.g. urea adducts and zeolites) and sandwiched compounds (e.g. graphite and silica complexes).

The success of Powell in understanding the nature of clathrates was to a large extent prepared by many scientific titans, on the shoulders of which he was standing. To get a complete historical perspective and to see what influenced Herbert Powell it is necessary to mention several other scientists, who came across clathrate materials in their efforts to perceive this mystery of nature as well as their successors, who still refine our knowledge about it.

As we already saw, host-guest compounds have been known for more than 200 years. An anomalous ice forming at positive temperatures was observed by Priestley in 1777 [23]. Clathrates made of water are called hydrates and were described in 1811 by Sir Humphrey Davy with chlorine as a guest molecule [21]. The composition of these compounds was initially determined by Michael Faraday in 1823 [22]. Hydrates of natural gas were widely studied during the previous century, mainly because of their implications in petroleum and petrochemical industry [24]. Structures, pressure-temperature stability regions, and some possible ways of practical utilization were determined [25].

The breakthrough work of Powell was based on clathrates of hydroquinone, which were of interest to many chemists before and after him. Firstly, hydroquinone was found by Wohler and Clemm to trap H_2S and SO_2 [29, 30]. An ability of hydroquinone to trap carbon monoxide was reported by Mylius in 1886 [31]. Afterwards, hydroquinone was found to trap Xe, Kr, O_2, CH_4, and many other molecules including fullerenes C_{60} and C_{70} [70]. Hydroquinone forms three kinetically stable modification alpha, beta, and gamma, with alpha being thermodynamically stable at ambient conditions. The gamma structure does not have cavities of molecular size and does not form clathrates. The alpha structure could be stable without guests, whereas the beta structure requires some cavities to be filled in order to be stable. To accommodate large molecules, such as fullerenes, hydroquinone adapts an expanded and modified beta structure, with one of two self-penetrating frameworks being removed. This modification, which cannot exist with vacant cavities, is known as delta structure. Hydroquinone plays special role in the chemistry of clathrates, because it served as a model host material in early studies of host-guest interactions [70].

In 1897 Hofmann synthesized clathrates obeying a general formula $M(NH_3)_2 \cdot M'(CN)_4 \cdot 2G$, where an octahedral metal M is Ni, Fe, Co, Zn, Cu, Mn, or Cd; a square planar metal M' is Ni, Pd, or Pt; G is a guest molecule C_4H_4S, C_4H_4NH, C_6H_6, C_6H_5OH, or $C_6H_5NH_2$ [32]. Hofmann concluded that the role of G is to fill up space during formation of the compound. This view point is very similar to that of Powell, but precedes it by half a century. In recognition of Hofmann's achievement Iwamoto, who extensively studied these materials since 1966, proposed to call them Hofmann-type clathrates [71]. In Hofmann-type clathrates the host consists of a layered framework of metal atoms, most commonly square planar Ni

and octahedral Cd, bridged by the CN ligands. The layers are separated by ammonia or dimethylamine $(CH_3)_2NH$ molecules coordinated to the Cd atoms. Large enough cavities, capable to accommodate molecules as large as benzene, are formed between the layers and coordination groups [72]. There is no doubt that the conclusion of Hofmann on the role of guest molecules influenced many chemists working in the area of inclusion compounds and paved the way for further developments.

Dianin's type compound ($C_{18}H_{20}O_2$) was discovered in 1911-1914 [33, 34]. Dianin found that the compound can capture some amount of a solvent (diethyl ether, benzene, chloroform, acetic acid), from which it has been crystallized. Six molecules of $C_{18}H_{20}O_2$ form an hourglass-shaped cage which is held together at the top and bottom by a hydrogen-bonded ring of six phenolic hydroxyl groups. These compounds could be stable with or without guest molecules [73], allowing a separate study of the framework and comparative studies of different guests within it. This feature of the material opened a unique way of investigation of variations in guest-host behaviours and resulting physical properties [74, 75].

Following structural determinations of clathrates of hydroquinone in the end of the 40s, the early 50s were marked by resolution of structures of hydrates [76, 77, 78]. It appeared that structural rules formulated for ice [79, 80] were also valid for hydrate frameworks.

Another interesting virtue of clathrates, an ability to store clusters of guest molecules, has been unveiled at the very end of the 20th century, firstly for nitrogen [81] and then for hydrogen guests. In 1999 hydrogen hydrates were synthesized by Yu. Dyadin and co-workers [20]. In the large cage of these hydrates four hydrogen molecules form a tetrahedral cluster. Since the initial discovery other experimental works attempted to estimate hydrogen storage capacity of the material, with the most optimistic result being 5 wt% of hydrogen and having from one to four molecules stored in a single cage [82, 83]. This discovery linked clathrate materials with hydrogen economy [10].

3.2 Clathrates of Water

3.2.1 Properties, Occurrence, and Structures of Hydrates

Water clathrates or hydrates are formed as a result of physical combination of water molecules, which are arranged into cages, and suitably sized nonpolar or slightly polar guest molecules occupying cages and stabilizing an overall structure by means of weak host-guest intermolecular interactions. The cage-like structure built from hydrogen bonded water molecules is unstable without guest molecules. Moreover, appropriate conditions of temperature and pressure are required to stabilize the clathrate structures even when it is filled with guests. High pressure and low temperature are favorable conditions for the formation of hydrates. These appropriate

conditions could be met in nature or in a laboratory.

On the earth, hydrates are found on oceanic beds and in permafrost regions. Suitable conditions for the formation of hydrates also exist in space. A high content of certain volatile species (CO, Ar, Kr, Xe) in comets was explained as a result of enclathration of these molecules in hydrates [84]. A deficiency of nitrogen with respect to the CO content in comets was shown to be due to the relative ease of formation of carbon monoxide hydrates in comparison with nitrogen hydrates. The existence of a clathrate reservoir on Enceladus, the 500-kilometer-diameter moon of Saturn, was hypothesized based on an observation of a plume produced by possible degassing of the reservoir [85]. Apart from water vapor the plume contained gases CH_4, N_2, and CO_2 at concentrations, which are close to the water-to-guest ratio in clathrates and which could not be explained by their solubility in liquid water. The existence of appropriate conditions for the formation of carbon dioxide hydrates on Mars was known since 1970 [86]. A high atmospheric CO_2 content and low surface temperature could result in formation of large deposits of the hydrates. The dissociation of these deposits may be partially responsible for the formation of chaotic terrain, outflow channels, and dynamic behavior of Martian polar caps. It is also possible that hydrates played an important role in the development of the solar system itself. They probably trapped volatile molecules in ice structures, which then aggregated along with other materials into larger bodies of early solar nebula.

Clathrates in space are not technologically accessible but gas hydrates occurring on the earth are considered as a potential energy source. Their energy equivalent is approximately twice as large as that of all other fossil fuels [25, 87]. Natural gas hydrates are mainly formed by methane, which is believed to have buffering effect during glacial periods as it is a strong greenhouse gas (24 times stronger than carbon dioxide [25]). In the context of climate change, gas hydrates could be used to sequestrate carbon dioxide on sea beds, as hydrates formed by CO_2 are heavier than water. At the same time, natural gas hydrates create a potential danger as they could release methane upon heating due to global warming and thus magnify anthropological alteration of the temperature. In petroleum and chemical industry gas hydrates present a problem as they can form blockages in pipelines and treatment facilities. Hydrates could be formed at temperatures above zero (15°C and 10 MPa) and could contain up to 15 mole% of guest molecules [88]. Hydrates exclude impurities from their structure and prefer to trap heavy molecules from the gas phase. These properties were proposed as a possible basis for water purification or even desalination and gas separation technologies [25].

Water is known to form three common gas hydrate structures [88]. They are structure I, structure II, and structure H, figure 3.1. Structure I is formed with small guest compounds like methane and carbon dioxide. Structure II is formed with intermediate sized guest compounds like propane or butane. Structure H requires large

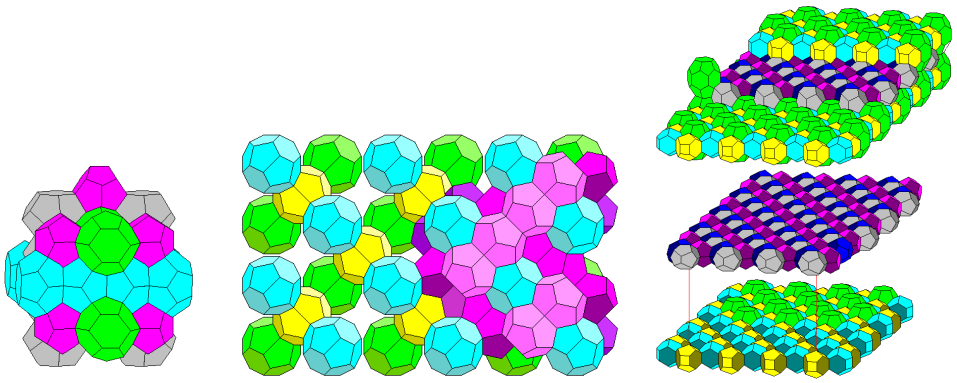

(a) Structure I (b) Structure II (c) Structure H

Courtesy of Prof. Steve Dutch, University of Wisconsin-Green Bay [89].

Figure 3.1: Structures of gas hydrates.

Characteristic*	I		II		H		
	Small	Large	Small	Large	Small	Medium	Large
Specification	5^{12}	$5^{12}6^2$	5^{12}	$5^{12}6^4$	5^{12}	$4^35^66^3$	$5^{12}6^8$
Coordination number (H_2O per cage)	20	24	20	28	20	20	36
Cages per unit cell	2	6	16	8	3	2	1
Mean cage radius, Å	3.95	4.33	3.91	4.73	3.94	4.04	5.79
Guest radius†, Å	1.8-2.2	1.8-2.7	1.8-2.2	2.8-3.1	1.8-2.2	1.8	3.5-4.3
Some guests	Ar, CO_2, N_2, CH_4	CO_2, C_2H_6	Ar, O_2, N_2, CH_4	C_3H_8, $(CH_3)_3$·CH	Ar, O_2, N_2, CH_4	CH_4	$(CH_3)_3$·CC_2H_5, C_6H_{12}
Lattice	Body-centred cubic		Face-centred cubic		Hexagonal		
Space group	Pm3n		Fd3m		P6/mmm		
Unit cell‡, Å	a = 12.03		a = 17.31		a = 12.26, c = 10.17		
Theoretical unit cell formula†	$(S)_2(L)_6 46H_2O$, S: small guest, L: large guest		$(S)_{16}(L+)_8 136H_2O$, S: small guest, L+: larger guest		$(S)_5(L++)34H_2O$, S: small guest, L++: largest guest		
H_2O per unit cell	46		136		34		

*[90]; †[27]; ‡[88].

Table 3.1: Characteristics of hydrate structures and cages.

molecules along with small ones in order to be formed. Each mentioned structure is made of different cages. These cages are polyhedrons with water molecules placed at each vertex and forming hydrogen bonds with the nearest neighbors. Structure I consists of small and large cages. The small cage constitutes of twelve pentagonal faces (5^{12}). The large cage composes of twelve pentagonal faces and two hexagonal faces ($5^{12}6^2$). Structure II also consists of small and large cages. The small cage is the same as that of structure I but its large cage has twelve pentagonal faces and four hexagonal faces ($5^{12}6^4$). Structure H consists of small, medium, and large cages. The small cage is the same as in structures I and II. The medium cage consists of three tetragonal faces, six pentagonal faces, and three hexagonal faces ($4^35^66^3$). The large cage composes of twelve pentagonal faces and eight hexagonal faces ($5^{12}6^8$).

Hydrates do not have fixed chemical formulae as they are nonstoichiometric compounds. That is because not all cages are required to be filled in to stabilize the

structure. As a result the ratio of guest to water molecules is not a constant [90, pp. 72–92]. In general, large guest molecules cannot occupy small cages. Small guest molecules or clusters of them can occupy some large cages in the hydrate structure, e.g. hydrogen hydrates. A molecule which is slightly bigger than the cage could deform the cage and fit into it. In structure I, small molecules, e.g., methane or nitrogen, fill in small cages and could fill in some large cages. If large molecules are present they fill in majority of the large cages. Structure II is sensible to the availability of intermediate sized molecules, which can be replaced by clusters of small molecules. The structure will not form in the absence of these intermediate sized entities. For the structure H to be stable its small and intermediate cages should be filled in with small molecules and its large cages should be filled in with large molecules. Gas hydrates formed from two types of guest molecules are referred to as double gas hydrates. Sometimes they are called ternary gas hydrates [10]. Information about three common structures of gas hydrates is conveniently summarized in table 3.2.1.

3.2.2 Hydrogen Hydrates

Experimental Studies

As it was shown in 1999 by Dyadin et al. [20], molecular hydrogen and water could be crystallized into the structure II of hydrates, if appropriate conditions of pressure and temperature are met. An interesting feature of these clathrates – an ability to encapsulate clusters of guest molecules – disclosed a scientific delusion that hydrogen could not form hydrates because of the small size of these molecules. Even if hydrogen molecules are too small, conglomerates of them have a sufficient size to support a hydrate structure. A chemical formula of the unit cell $(H_2)_{16}(4H_2)_8 136H_2O$ at estimated maximum hydrogen capacity shows that the 16 small cages are occupied by one hydrogen molecule per cage and the 8 large cages are occupied by four hydrogen molecules each. The stability margin of hydrogen hydrates is far from ambient conditions and different occupancies of hydrate cages were also reported. An initial estimation of hydrogen capacity done in the group of Mao [82] attributed two hydrogen molecules to the small cage. Further study, done by Lokshin and Zhao in collaboration with Mao's group [83], showed that only one molecule could be stored in the small cage. In the group of Mao, formation of the hydrate was observed at 180-220 MPa and 249 K. Lokshin and Zhao's work further detailed this data providing a phase diagram for hydrogen hydrates and demonstrated that the cages remain filled with the maximum number of hydrogen molecules up to the temperatures 70 K at 1 atm and 190 K at 2000 atm. The maximum occupancy gives 3.8 wt% of molecular hydrogen stored in the material.

From a technological viewpoint, the conditions at which hydrogen hydrates are

stable are not appropriate. Pressures of thousands of atmospheres and cryogenic temperatures are arduous to create even in a stationary research equipment, not mentioning mobile applications. Two methods have been proposed to mitigate these requirements. First, an additional guest or promoter molecule can be introduced. The widely studied and successful promoter THF could reduce pressure for hydrate formation by a factor of 30 (to 7 MPa at 280 K) [91, 10]. In these binary hydrates the large cages are filled in with THF and small cages with hydrogen. Partial filling of the large cages with H_2 is also possible. Another approach to get additional degree of tunability of equilibrium conditions is to introduce a second host molecule. These structures are called semiclathrates. Chemical species with hydrogen-bonding abilities (e.g. Tetra-n-Butylammonium Bromide (TBAB)) can be involved into the network of water molecules and form complex composites [92, 10]. Both these attempts to stabilize hydrates at near ambient pressure and temperature have one common drawback. They lead to the reduction of hydrogen storage capacity, which is low even in the pure material.

Apart from practically important implications of introducing additional guests, mixing of hydrogen with other molecules not only moderates conditions for the formation of structure II, but also promotes formation of other hydrate structures. For example, structure I of hydrates could be formed when hydrogen is mixed with carbon dioxide, which when present in excess determines the favorable structure [93]. In this case, hydrogen occupies small cages and carbon dioxide occupies large cages. On the other hand, the H structure is formed when hydrogen hydrates are formed in the presence of large molecules like Methyl Tert-Butyl Ether (MTBE), Methylcyclohexane (MCH), 2,2,3-Trimethylbutane (2,2,3-TMB) [94] (these molecules form the same hydrate structure with methane or xenon). The occupation of cages obeys the same logic as for the mixed carbon dioxide hydrates. Hydrogen remains in the small and medium cages of structure H and large molecules stay in the large cages.

Theoretical Studies

Theoretical studies of hydrogen clathrate hydrates mostly aimed to predict their thermodynamic stability with respect to different occupation of cages and were performed for both gas phase and periodic systems. These studies vary in theoretical approaches applied and utilize electronic structure calculations [95, 96, 97], methods of statistical mechanics [95, 96], lattice dynamics calculations [98], classical molecular dynamics [99], and quantum dynamics of a hydrogen molecule inside the hydrate cages [100, 101, 102].

In the work [95] authors combined electronic structure calculations and a statistical mechanical model to estimate the number of hydrogen molecules, which could be stored in each cage at different pressure-temperature conditions. The model pre-

dicted two molecules in the small cage (double occupancy) and four molecules in the large cage (quadruple occupancy) at 250 K and a pressure larger than 1000 bar. The work also resulted in the construction of MP2/DZ spherical potentials for a hydrogen molecule inside rigid cages of the hydrate structure. The potentials were then used to study quantum effects. It was demonstrated that quantum treatment results in a 14% increase in the calculated equilibrium constants for the reaction of enclathration of deuterium, which in turn may result in an increase of the decomposition temperature by up to 20 K at ambient pressure [96]. A similar type of study, but based on the local density approximation to electron correlation and exchange effects and performed for periodic structures I and II, came to the same conclusion that 2 and 4 hydrogen molecules could be stored in the small and large cages of the hydrates, respectively [97]. The stabilities of structure II with one and two hydrogen molecules per small cage were found to be similar. Further lattice dynamics calculations were performed for structure II of hydrates with different occupancies of the cages. Two different empirical potentials for the guest-guest interactions were employed, but the results proved to be insensitive to the details of the potential [98]. The work predicted the equilibrium pressure of hydrogen hydrates in good agreement with the experimental data of Lokshin and Zhao [83].

Classical molecular dynamics simulations aiming to investigate the stability of structure II as a function of occupation of both types of cages confirmed that the small cage is singly occupied [99]. In addition, the work indicated that if the cage was doubly occupied a tetragonal distortion of the unit cell would take place, which was not observed experimentally. The single and quadruple occupancies of the small and the large cages, respectively, were also shown to provide the closest agreement with the experimental values of lattice constants.

A more rigorous quantum mechanical treatment of the dynamics of a hydrogen molecule inside the hydrate cages was reported in series of papers done in a group of Zlatko Bačić [100, 101, 102]. In these studies the cages were assumed to be rigid and the transrotational dynamics of a rigid hydrogen molecule inside the cages was described in a five dimensional space. The variables were the position of the center of mass and two polar angles defining its orientation. The 5D H_2-cage potential energy surface was constructed by summation of all pairwise interactions between water molecules of the cage and the encapsulated hydrogen molecule, and applying an *ab-initio* potential energy surface for the H_2-H_2O complex. As a result, the translational-rotational energy levels and wave functions of a confined hydrogen molecule have been obtained. The temperature dependence of the average translational-rotational energy has been calculated from the obtained energy levels for one hydrogen molecule in the small cage. The probability of a hydrogen molecule to be in the ground state at 150 K was shown to be only 17.5%. The potential energy surface for H_2 in the small cage was found to be rather flat in the central region

whereas in the large cage it has a pronounced maximum at the center. This maximum localizes a wave function of H_2 away from the cage center and gives rise to excited translational-rotational states.

3.3 Statistical Theory of Hydrate Phase Equilibria

Problems which hydrates present during normal operation of petroleum and petrochemical industry inspired the development of methods that aim to predict the so-called hydrate stability zone, a pressure-temperature region on the Pressure-Temperature (PT) phase diagram, where hydrates are a thermodynamically stable phase in comparison with liquid water, ice, and gas. In addition, some models may account for the presence of a liquid hydrocarbon phase and salts. The model which proved to be the most successful and which serves as a basis for more modern techniques is that of van der Waals and Platteeuw [103], although in a comprehensive work of Sloan and Koh [90] we find that an initial formulation of the model was proposed in 1957 by Barrer and Stuart. Before discussing the model it is beneficial to overview briefly first of all experimental and then other predictive techniques available to calculate the hydrate stability zone [90].

There are visual and graphical experimental methods to detect hydrate formation and dissociation, with the graphical method being the most reliable. In the graphical method an experimental cell is charged with a test fluid and then it is cooled down until hydrates are formed. The formation is characterized by a significant pressure drop. The cell is then heated up until hydrates are decomposed. Upon decomposition a pressure rise is significant and after the dissociation of hydrates any further rise is only due to the thermal expansion of the gas, which is very slow. A cross point of the straight lines fitted into the initial parts of the cooling and heating curves is taken as the dissociation point for a given composition of the test fluid. It is essential that sufficient time is allowed to reach equilibrium at each temperature step.

Apart from the statistical model, a gas gravity method and a distribution coefficients method are used to predict the hydrate stability zone. In the first approach the gas gravity is found as a ratio of the molar weight of a given mixture of hydrocarbon gases to the molar weight of air. The value found determines a hydrate dissociation curve on a predefined PT diagram. In the distribution coefficients method the vapor-solid distribution coefficients K_{vsi} for each component i of the gas mixture are defined according to equation 3.1, where y_i is the mole fraction of i in the water-free vapor; x_{si} is the mole fraction of i in the water-free solid hydrate.

$$K_{vsi} \equiv y_i / x_{si} \tag{3.1}$$

The K_{vsi} values for natural gases are presented graphically as a function of pressure and temperature. The PT conditions for hydrate formation are thought to be met when equation 3.2, analogous to the dew point condition in vapor-liquid equilibrium, is satisfied. To use the method the composition of the gas phase of interest, i.e. all $y_i, i = 1, 2...n$, should be known.

$$\sum_{i=1}^{n} \frac{y_i}{K_{vsi}} = 1.0 \tag{3.2}$$

The predictive techniques outlined so far are essentially of empirical nature. The gas gravity charts and distribution coefficients diagrams cannot be constructed without significant experimental input. In contrast, the statistical theory is less experiment dependent and, for example, its reliance on experimental intermolecular potentials may be eliminated by usage of intermolecular potentials obtained from *ab-initio* calculations. The theory is based on the assumption that the stability of hydrates can be predicted from the motion of guest molecules inside rigid cages of water molecules. To describe the model we briefly outline its main assumptions and major equations [90]. Four assumptions upon which the model is built are: (i) The free energy of the lattice of host molecules is independent of the occupation of the cavity (guest molecules do not distort the cage); (ii) Each cavity can contain at most one guest molecule; (iii) There are no interactions between encaged molecules; (iv) No quantum effects are needed and classical statistical thermodynamics is valid.

In the statistical model all thermodynamical quantities are derived from the grand canonical partition function for water, equation 3.3.

$$\Xi = \exp\left(-\frac{A^{\beta}}{kT}\right) \prod_{i} \left(1 + \sum_{J} q_{J,i}\lambda_J\right)^{\upsilon_i N_W} \tag{3.3}$$

In equation 3.3 A^{β} is the Helmholtz free energy of the empty host lattice; k is the Boltzmann's constant; T is the temperature; $q_{J,i}$ is the partition function of a type J molecule in a type i cavity; λ_J is the absolute chemical activity of a guest molecule of type J; υ_i is the number of type i cavities per one water molecule; N_W is the number of host (water) molecules.

As an example, from the grand canonical partition function we may calculate the total number of guest molecules of type J over all the cavities i, equation 3.4.

$$N_J = \sum_{i} N_{J,i} = \lambda_J \left(\frac{\partial ln\Xi}{\partial \lambda_J}\right)_{T,V,N_W,\lambda_{k\neq J}} \tag{3.4}$$

Then the probability of finding a molecule of type J in a cavity of type i, or the occupancy fraction $\theta_{J,i}$, could be found as shown in equation 3.5.

$$\theta_{J,i} = \frac{N_{J,i}}{\upsilon_i N_W} = \frac{q_{J,i}\lambda_J}{1 + \sum_J q_{J,i}\lambda_J} \tag{3.5}$$

For each molecular type J and a cavity type i one collects the partition function and the absolute activity in a constant $C_{J,i} \equiv q_{J,i}\lambda_J/P_J$, with P_J being the partial pressure of J. Then, the occupancy fraction of the J type molecule in the i type cavity is expressed in the form of equation 3.6.

$$\theta_{J,i} = \frac{C_{J,i}P_J}{1 + \sum_J C_{J,i}P_J} \tag{3.6}$$

The chemical potential μ_W^H of water in hydrate may also be derived from the grand canonical partition function for water according to equation 3.7.

$$\mu_W^H = -kT\left(\frac{\partial ln\Xi}{\partial N_W}\right)_{T,V,\lambda_J} = \mu_W^\beta + kT\sum_i \upsilon_i ln\left(1 - \sum_J \theta_{J,i}\right) \tag{3.7}$$

In equation 3.7 μ_W^β is the chemical potential of water in the empty hydrate structure.

The combination of equations 3.6 and 3.7 forms the corner-stone of the method as the model equates the chemical potential of a component in different phases at given pressure and temperature. At equilibrium the chemical potential of water in hydrate phase is equal to that in other coexisting phases (ice, liquid water).

The Langmuir constants $C_{J,i}$ introduced in equation 3.6 depend on intermolecular interactions between the guest molecule and host molecules composing the cage. They may be found according to equation 3.8, if the cell potential $w(r)$ of a cage of radius R_c is known.

$$C_{J,i} = \frac{4\pi}{kT}\int_0^{R_c} \exp\left(-\frac{w(r)}{kT}\right) r^2 dr \tag{3.8}$$

To obtain $w(r)$ one starts from the Kihara potential to represent the interaction between a water molecule of the cavity wall and the guest molecule, eqn 3.9.

$$\begin{aligned} &\Phi(r) = \infty,\ r \leq 2a \\ &\Phi(r) = 4\epsilon\left[\left(\frac{\sigma}{r-2a}\right)^{12} - \left(\frac{\sigma}{r-2a}\right)^{6}\right],\ r > 2a \end{aligned} \tag{3.9}$$

In equation 3.9 ϵ is the depth of the Kihara potential; a is the radius of the spherical core representing the gas molecule; σ is the finite distance between cores at which the potential is zero, i.e. $\Phi(\sigma + 2a) = 0$.

The parameters $\epsilon,\ a,\ \sigma$ are obtained by fitting experimental data for clathrate dissociation. Integration of the potential over all host molecules of the cage results in equation 3.10 [104].

$$
\begin{aligned}
w(r) &= 2Z\epsilon \left[\frac{\sigma^{12}}{R_c^{11} r} \left(\delta^{10} + \frac{a}{R_c} \delta^{11} \right) - \frac{\sigma^{6}}{R_c^{5} r} \left(\delta^{4} + \frac{a}{R_c} \delta^{5} \right) \right], \\
\text{where } \delta^M &= \frac{1}{M} \left[\left(1 - \frac{r}{R_c} - \frac{a}{R_c} \right)^{-M} - \left(1 + \frac{r}{R_c} - \frac{a}{R_c} \right)^{-M} \right]
\end{aligned}
\tag{3.10}
$$

In equation 3.10 Z is the coordination number (number of host molecules in the cage).

3.4 Statistical Theory and Hydrogen Hydrates

Although the statistical theory of clathrate formation was proven to be adequate in prediction of formation conditions of hydrates of relatively large spherical (e.g. Xe) or quasispherical (e.g. CH_4) molecules, one would expect its failure in prediction of properties of hydrates of small molecules (e.g. H_2). The second assumption of the theory says that each cage contains at most one molecule, which is not true for hydrogen hydrates as the large cage contains up to four molecules. The fourth assumption of the theory excludes quantum effects from consideration which is not valid for the lightest molecule, hydrogen. In the work [105] the hydrate formation model based upon the statistical theory enabling description of hydrates formed from a mixture of gases has been used. The model parameters have been optimized for THF and H_2, which resulted in adequate thermodynamic predictions for binary THF-H_2 hydrates. The success may be assigned to the leading role of THF in stabilization of the hydrates. The molecules of THF fill in large cages and leave small ones to hydrogen, which preserves validity of the second assumption of the statistical theory and to some extent mitigates a violation of the fourth assumption by hydrogen. These advantageous properties of binary hydrates are absent in the case of pure hydrogen hydrates. Apart from this qualitative reasoning, quantitative arguments are required to demonstrate inability of the theory to predict stability of pure hydrogen hydrates.

In this section we apply the theory in an attempt to predict the dissociation pressure and hydration number of simple hydrate formers such as xenon, carbon dioxide, methane, ethane, propane, nitrogen, and hydrogen. This small illustration highlights the drawback of the model in description of pure hydrogen hydrates. As a foundation for this test we take an approach applied in [106], where the dissociation pressure of some hydrates was predicted using properties of the reference hydrate.

At equilibrium, the chemical potential of water in a hydrate phase is equal to that in ice $\mu_W^H = \mu_W^\alpha$, which allows expressing the chemical potential difference in the form of equation 3.11. We do calculations at the ice-point temperature and assume that liquid water phase is not present.

$$\triangle\mu_W^\alpha = \mu_W^\beta - \mu_W^H = \mu_W^\beta - \mu_W^\alpha \tag{3.11}$$

The calculated chemical potential difference is obtained from equations 3.6 and 3.7. To account for non-ideality of real gases, pressure in equation 3.6 was replaced with fugacity. The experimental chemical potential difference is calculated, in accordance with [106] and [107, pp. 248–253], from equations 3.12 and 3.13. The dissociation pressure is supposed to be found when both, calculated and experimental, chemical potential differences are equal.

$$\begin{aligned}\frac{\triangle\mu_W^\alpha(T,P_R)}{RT} &= \frac{\triangle\mu_W^\alpha(T_0,P_0)}{RT_0} - \int_{T_0}^{T}\frac{\triangle h_W^\alpha}{RT^2}dT + \int_{T_0}^{T}\frac{\triangle v_W^\alpha}{RT}\frac{dP}{dT}dT \\ &= \frac{\triangle\mu_W^\alpha(T_0,P_0)}{RT_0} - \int_{T_0}^{T}\frac{\triangle h_W^\alpha}{RT^2}dT + \int_{P_0}^{P_R}\frac{\triangle v_W^\alpha}{RT}dP\end{aligned} \tag{3.12}$$

$$\triangle\mu_W^\alpha(T,P) = \triangle\mu_W^\alpha(T,P_R) + \triangle v_W^\alpha(P-P_R) \tag{3.13}$$

In equations 3.12 and 3.13 P_R is the reference hydrate dissociation pressure; $\triangle\mu_W^\alpha(T_0,P_0)$ is the chemical potential difference at some reference temperature T_0 and pressure P_0, usually taken as 273.15 K and 1 atm, respectively [107, p. 250]; $\triangle h_W^\alpha$ and $\triangle v_W^\alpha$ are the molar differences in enthalpy and volume between the empty hydrate framework and ice, respectively.

The first integral in equation 3.12 is zero, as we are only interested in $T = T_0$, and the second integral is reduced to $\triangle v_W^\alpha(P_R - P_0)/RT$, as $\triangle v_W^\alpha$ is assumed to be constant. The required dissociation pressure for a reference hydrate is obtained from equation 3.14 [106].

$$lnP_R = A_R + B_R/T + C_R lnT \tag{3.14}$$

In equation 3.14 A_R, B_R, and C_R are constants fitted to represent the experimental data.

The fugacity was calculated from equation 3.15 [108, p. 280] with molar volume V_m obtained from the van der Waals equation of state, which was solved iteratively starting with the molar volume estimated according to the ideal gas law.

$$f = P\exp\left[\frac{1}{RT}\int_0^P\left(V_m - \frac{RT}{P}\right)dP\right] \tag{3.15}$$

For simple hydrates, when the occupancy fractions θ_i are known, the hydration number N_{HN} could be found from equation 3.16.

$$N_{HN} = N_W/\sum_i \upsilon_i N_W\theta_i = 1/\sum_i \upsilon_i\theta_i \tag{3.16}$$

Parameter*		Structure I	Structure II
$(\mu_W^\beta - \mu_W^\alpha)^\dagger$, cal/mol		302	211
$(v_W^\beta - v_W^\alpha)^\dagger$, cc/mol		3.0	3.4
For P_R in atm and T in K	A_R	-1212.2	-1023.14
	B_R	44344.0	34984.3
	C_R	187.719	159.923

*[106]; †At 0°C and 1 atm.

Table 3.2: Parameters required in equation 3.12, 3.13, and 3.14.

Component*	a, Å	σ, Å	ε/k, K
Xe†	0.2357	3.32968	193.708
CO_2	0.6805	2.9818	168.77
CH_4	0.3834	3.1650	154.54
C_2H_6	0.5651	3.2641	176.40
C_3H_8	0.6502	3.3093	203.31
$N_2^\ddagger$	0.3526	3.13512	127.426
$H_2^\ddagger$	0.1973	3.07838	80.424

*[107]; †[90]; ‡[105, supplementary data].

Table 3.3: Kihara potential parameters.

In equation 3.16 N_W is the number of water molecules per unit cell; υ_i is the number of type i cavities per one water molecule; $\upsilon_i N_W$ is the number of cavities of type i per unit cell.

The structural parameters of hydrates required in calculations are taken from table 3.2.1. The parameters required in equations 3.12, 3.13, and 3.14 are collected in table 3.4. The parameters of the Kihara potential used to evaluate the Langmuir constants are collected in table 3.4. The results of the calculations for a selected set of guests are compared with experimental data and presented in table 3.4.

For all considered gases apart from hydrogen, the predicted dissociation pressure and hydration number are in satisfactory to excellent agreement with the reported values. This simple illustration shows the model's potential in description of properties of hydrates. For hydrogen hydrates our calculations did not converge with the default convergence criterion for $\triangle\mu_W^\alpha/RT$, which was set to 10^{-9}. With the term $\triangle v_W^\alpha(P-P_R)$ in equation 3.13 taken into account this convergence criterion has been reduced to 10^{-6}. No difference in theoretical predictions for other hydrates has been observed with the less strict criterion. The experimental and calculated dissociation pressures of hydrogen hydrates differ by a factor of two with $\triangle v_W^\alpha(P-P_R)$ and by a factor of three without this term, which illustrates inapplicability of the model to hydrogen hydrates. The predicted hydration number is not expected to be correct as the model assumes single occupancy of the cages. Contrary, the experimental results show that at 1 kbar the large cage is doubly occupied up to a temperature 170 K. The occupancy remains quadruple at 2 kbar up to 180 K [83]. It should be

Guest molecule	Hydrate structure	Published data† T, °C; P, atm	Dissociation pressure¶, atm with △	Dissociation pressure¶, atm without △	Hydration number Published‡	Hydration number Calculated
Xe	I	0; 1.5	1.5	1.5	N/A	6.13
CO_2	I	0; 12.4	12.4	12.6	N/A	6.27
CH_4	I	-0.2; 25.3	28.6	28.5	6.00	6.05
C_2H_6	I	-0.03; 5.23	4.2	4.3	7.67	7.76
C_3H_8	II	0; 1.74	1.6	1.7	17.0	17.02
N_2	II	-1.3; 141.5	128.4	113.3	N/A	6.35
H_2	II	-3.15; 2072.5§	1087.1*	640.6	N/A	5.95*

†[90]; ¶Calculated at 273.15 K, $\triangle \equiv \triangle v_W^{\alpha}(P - P_R)$ in equation 3.13; ‡[110]; §[83]; *See text.

Table 3.4: Calculated and experimental dissociation pressures and hydration numbers of selected hydrates.

mentioned that recently there was an attempt to generalize the model in order to account for a multiple cage occupancy [109, pp. 19–25], but still without accounting for quantum effects, which are important for small molecules like hydrogen [96].

3.5 Conclusions

Clathrates could provide a desirable combination of weak and strong hydrogen binding forces. Experimental studies of hydrogen hydrates found that one and four hydrogen molecules could be enclosed in the small and large cages of structure II, respectively. This maximum occupancy results in only 3.8 wt% of H_2 stored under impractically high pressure and low temperature. Attempts to mitigate storage conditions lead to reduction of hydrogen capacity, which is already low. As it is seen from theoretical studies, especially from the works of Patchkovskii et al. and Bačić et al., the dynamics of a hydrogen molecule enclosed in the clathrate cages is to a large extent quantum mechanical. It is thus instructive for any approach aiming to predict the hydrogen clathrate stability zone to account for quantum effects. The commonly used statistical model does not take these effects into consideration. Moreover, it is its main assumption that no quantum effects are needed. Therefore, in further chapters not only the design of AB clathrates is proposed, but a model linking *ab-initio* intermolecular interactions and the PT stability of clathrates is developed, which takes into account the quantum nature of confined H_2 molecules.

Chapter 4

Theory and Computational Methods

4.1 Schrödinger Equation and Fundamental Approximations

4.1.1 Schrödinger Equation

The Schrödinger equation for N electrons having positions $\boldsymbol{r} = \{\boldsymbol{r}_1, \boldsymbol{r}_2, ...\boldsymbol{r}_i, ...\boldsymbol{r}_N\}$ and A nuclei with positions $\boldsymbol{R} = \{\boldsymbol{R}_1, \boldsymbol{R}_2, ...\boldsymbol{R}_I, ...\boldsymbol{R}_A\}$ reads, equation 4.1.

$$\hat{H}\Phi(\boldsymbol{r}, \boldsymbol{R}, t) = i\hbar\frac{\partial}{\partial t}\Phi(\boldsymbol{r}, \boldsymbol{R}, t) \tag{4.1}$$

In equation 4.1 $\hat{H}$ is the energy operator; $\Phi(\boldsymbol{r}, \boldsymbol{R}, t)$ is the wave function; t is time.

The energy operator or Hamiltonian, equation 4.2, includes terms accounting for the kinetic energy of nuclei $\hat{T}_{nuc}$ and electrons $\hat{T}_{elec}$, the potential energy of interactions between electrons and nuclei $\hat{V}_{elec-nuc}$, electrons and electrons $\hat{V}_{elec-elec}$, and nuclei $\hat{V}_{nuc-nuc}$. It may contain more terms when, for example, external electric or magnetic fields are present.

$$\begin{aligned}\hat{H} &= \hat{T}_{nuc} + \hat{T}_{elec} + \hat{V}_{elec-nuc} + \hat{V}_{elec-elec} + \hat{V}_{nuc-nuc} = \\ &= -\frac{\hbar^2}{2}\sum_I \frac{\nabla_I^2}{M_I} - \frac{\hbar^2}{2m_e}\sum_i \nabla_i^2 - \frac{e^2}{4\pi\epsilon_0}\sum_{i,I}\frac{Z_I}{|\boldsymbol{r}_i - \boldsymbol{R}_I|} + \\ &+ \frac{e^2}{4\pi\epsilon_0}\frac{1}{2}\sum_{i\neq j}\frac{1}{|\boldsymbol{r}_i - \boldsymbol{r}_j|} + \frac{e^2}{4\pi\epsilon_0}\frac{1}{2}\sum_{I\neq J}\frac{Z_I Z_J}{|\boldsymbol{R}_I - \boldsymbol{R}_J|}\end{aligned} \tag{4.2}$$

In equation 4.2 ∇ is the nabla operator; M and Z are the masses and atomic numbers of nuclei; m_e and e are the mass of an electron and the elementary charge, respectively; ϵ_0 is the permittivity of vacuum.

To solve a differential equation of such complexity as equation 4.1 with the Hamiltonian shown in equation 4.2 several approximations are required.

4.1.2 Born-Oppenheimer Approximation

In the Born-Oppenheimer approximation we first rewrite the total Hamiltonian as a sum of the kinetic energy of the nuclei and the electronic Hamiltonian, equation 4.3. We then suppose that solutions of the electronic Schrödinger equation for fixed nuclei, equation 4.4, are known and eigenfunctions of $\hat{H}_{elec}$ are orthonormalized, i.e. $\langle \Psi_k \mid \Psi_l \rangle = \delta_{kl}$.

$$\hat{H}(\boldsymbol{r}, \boldsymbol{R}) = \hat{T}_{nuc}(\boldsymbol{R}) + \hat{H}_{elec}(\boldsymbol{r}, \boldsymbol{R}) \tag{4.3}$$

$$\hat{H}_{elec}(\boldsymbol{r}, \boldsymbol{R})\Psi_k(\boldsymbol{r}, \boldsymbol{R}) = E_k(\boldsymbol{R})\Psi_k(\boldsymbol{r}, \boldsymbol{R}) \tag{4.4}$$

We then expand the total wave function $\Phi(\boldsymbol{r}, \boldsymbol{R}, t)$ in terms of the eigenfunctions of $\hat{H}_{elec}(\boldsymbol{r}, \boldsymbol{R})$, equation 4.5, and insert this expansion into equation 4.1. Multiplication from the left by $\Psi_k^*(\boldsymbol{r}, \boldsymbol{R})$ and integration over coordinates of all electrons results in equation 4.6.

$$\Phi(\boldsymbol{r}, \boldsymbol{R}, t) = \sum_l \Psi_l(\boldsymbol{r}, \boldsymbol{R})\chi_l(\boldsymbol{R}, t) \tag{4.5}$$

In equation 4.5 χ_l is the nuclear wave function in the lth electronic state.

$$\langle \Psi_k \mid \left(\hat{T}_{nuc} + \hat{H}_{elec}\right) \sum_l \Psi_l\chi_l \rangle = \langle \Psi_k \mid i\hbar \frac{\partial}{\partial t} \sum_l \Psi_l\chi_l \rangle \tag{4.6}$$

For clarity, the left hand side of equation 4.6 may be written in a form of equation 4.7, which finally results in a set of coupled differential equations, equation 4.8.

$$\begin{aligned}
&\langle \Psi_k \mid \left(\hat{T}_{nuc} + \hat{H}_{elec}\right) \sum_l \Psi_l\chi_l \rangle = \\
&= \langle \Psi_k \mid -\frac{\hbar^2}{2} \sum_{I=1}^{N} \frac{1}{M_I} \sum_l \left(\nabla_I^2 \Psi_l\chi_l + 2\nabla_I\Psi_l\nabla_I\chi_l + \Psi_l\nabla_I^2\chi_l\right) \rangle + \\
&+ \langle \Psi_k \mid \hat{H}_{elec} \sum_l \Psi_l\chi_l \rangle = \\
&= \sum_l \left[\langle \Psi_k \mid \hat{T}_{nuc}\Psi_l \rangle - \sum_{I=1}^{N} \frac{\hbar^2}{M_I} \langle \Psi_k \mid \nabla_I\Psi_l \rangle \nabla_I \right] \chi_l + \left[\hat{T}_{nuc} + E_k\right] \chi_k
\end{aligned} \tag{4.7}$$

$$\sum_l \left[\langle \Psi_k \mid \hat{T}_{nuc}\Psi_l \rangle - \sum_{I=1}^{N} \frac{\hbar^2}{M_I} \langle \Psi_k \mid \nabla_I\Psi_l \rangle \nabla_I \right] \chi_l + \left[\hat{T}_{nuc} + E_k\right] \chi_k = i\hbar \frac{\partial}{\partial t}\chi_k \tag{4.8}$$

If all coupling terms between different electronic states in equation 4.8 are ignored then one obtains the clumped nuclei or Born-Oppenheimer approximation [111], equation 4.9.

$$\left[\hat{T}_{nuc} + E_k\right] \chi_k = i\hbar \frac{\partial}{\partial t} \chi_k \tag{4.9}$$

In the following sections we primarily concentrate on solutions to the time independent electronic Schrödinger equation, equation 4.4, in the lowest energy state.

4.1.3 Variational Principle

The variational principle allows one to use an arbitrary or trial wave function $\widetilde{\Psi}$ to calculate the expectation value of the Hamiltonian and states that the energy found, $\widetilde{E}$, is never less than the true ground state energy E_0 of the system [112], equation 4.10.

$$\widetilde{E} = \frac{\langle \widetilde{\Psi} \mid \hat{H}_{elec} \widetilde{\Psi} \rangle}{\langle \widetilde{\Psi} \mid \widetilde{\Psi} \rangle} \geq E_0 \tag{4.10}$$

To prove the principle we first expand the trial wave function $\widetilde{\Psi}$ in terms of eigenfunctions of the Hamiltonian ψ_k, equation 4.11, satisfying the orthonormality condition, equation 4.12. We then find a difference $\widetilde{E} - E_0$, equation 4.13.

$$\widetilde{\Psi} = \sum_k C_k \psi_k \tag{4.11}$$

$$\langle \widetilde{\Psi} \mid \widetilde{\Psi} \rangle = \sum_{kl} C_l^* C_k \langle \psi_l \mid \psi_k \rangle = \sum_k C_k^* C_k = \sum_k |C_k|^2 = 1 \tag{4.12}$$

$$\begin{aligned} \widetilde{E} - E_0 &= \langle \widetilde{\Psi} \mid \hat{H}_{elec} \widetilde{\Psi} \rangle - E_0 = \langle \sum_l C_l \psi_l \mid \hat{H}_{elec} \sum_k C_k \psi_k \rangle - E_0 = \\ &= \langle \sum_l C_l \psi_l \mid \sum_k C_k E_k \psi_k \rangle - E_0 = \sum_{kl} E_k C_l^* C_k \langle \psi_l \mid \psi_k \rangle - E_0 \cdot 1 = \\ &= \sum_k E_k |C_k|^2 - E_0 \sum_k |C_k|^2 = \sum_k |C_k|^2 (E_k - E_0) \geq 0 \end{aligned} \tag{4.13}$$

The fact that the difference $\widetilde{E} - E_0$ is greater than zero proves the variational principle. The difference could only be equal to zero if the exact ground state function was used as the trial function.

4.1.4 Perturbation Method

In perturbation method the Hamiltonian $\hat{H}_{elec}$, equation 4.4, is divided into two parts: the reference Hamiltonian $\hat{H}^{(0)}$ and the perturbation $\hat{H}^{(1)}$, equation 4.14.

The solutions of the reference Schrödinger equation, equation 4.15, are assumed to be known.

$$\hat{H}_{elec} = \hat{H}^{(0)} + \lambda \hat{H}^{(1)} \tag{4.14}$$

In equation 4.14 $\lambda \in [0, 1]$ is a variable parameter defining strength of the perturbation.

$$\hat{H}^{(0)} \Psi_k^{(0)} = E_k^{(0)} \Psi_k^{(0)} \tag{4.15}$$

For the sake of simple notation we only consider the ground state solution of equation 4.4. We expand the perturbed energy and wave function in powers of the perturbation parameter, equation 4.16.

$$\begin{aligned} E &= \lambda^0 E^{(0)} + \lambda^1 E^{(1)} + \lambda^2 E^{(2)} + ... \\ \Psi &= \lambda^0 \Psi^{(0)} + \lambda^1 \Psi^{(1)} + \lambda^2 \Psi^{(2)} + ... \end{aligned} \tag{4.16}$$

Upon substitution of equation 4.14 and equation 4.16 into equation 4.4 and equating coefficients of the same power in λ, one obtains perturbation equations [112, 113], equation 4.17.

$$\begin{aligned} \lambda^0 &: \hat{H}^{(0)} \Psi^{(0)} = E^{(0)} \Psi^{(0)} \\ \lambda^1 &: \hat{H}^{(0)} \Psi^{(1)} + \hat{H}^{(1)} \Psi^{(0)} = E^{(0)} \Psi^{(1)} + E^{(1)} \Psi^{(0)} \\ \lambda^2 &: \hat{H}^{(0)} \Psi^{(2)} + \hat{H}^{(1)} \Psi^{(1)} = E^{(0)} \Psi^{(2)} + E^{(1)} \Psi^{(1)} + E^{(2)} \Psi^{(0)} \\ &... \\ \lambda^n (n > 0) &: \hat{H}^{(0)} \Psi^{(n)} + \hat{H}^{(1)} \Psi^{(n-1)} = \sum_{p=0}^{n} E^{(p)} \Psi^{(n-p)} \end{aligned} \tag{4.17}$$

The requirement of intermediate normalization leads to $\langle \Psi^{(0)} \mid \Psi^{(n)} \rangle = \delta_{0n}$. Next, we multiply the last expression of equation 4.17 from the left by $(\Psi^{(0)})^*$ and we integrate it to obtain an expression for the nth order corrections to the energy, equation 4.18. The first and the second order corrections to the energy are shown in equation 4.19.

$$\begin{aligned} &\langle \Psi^{(0)} \mid \hat{H}^{(0)} \Psi^{(n)} \rangle + \langle \Psi^{(0)} \mid \hat{H}^{(1)} \Psi^{(n-1)} \rangle = \langle \Psi^{(0)} \mid \sum_{p=0}^{n-1} E^{(p)} \Psi^{(n-p)} \rangle + E^{(n)} \langle \Psi^{(0)} \mid \Psi^{(0)} \rangle \\ &E^{(0)} \langle \Psi^{(0)} \mid \Psi^{(n)} \rangle + \langle \Psi^{(0)} \mid \hat{H}^{(1)} \Psi^{(n-1)} \rangle = E^{(n)} \langle \Psi^{(0)} \mid \Psi^{(0)} \rangle \\ &E^{(n)} (n > 0) = \langle \Psi^{(0)} \mid \hat{H}^{(1)} \Psi^{(n-1)} \rangle \end{aligned} \tag{4.18}$$

In equation 4.18 we used $\langle\Psi^{(0)} \mid \hat{H}^{(0)}\Psi^{(n)}\rangle = \langle\Psi^{(n)} \mid \hat{H}^{(0)}\Psi^{(0)}\rangle^* = E^{(0)}\langle\Psi^{(n)} \mid \Psi^{(0)}\rangle^* = E^{(0)}\langle\Psi^{(0)} \mid \Psi^{(n)}\rangle$.

$$\begin{aligned} E^{(1)} &= \langle\Psi^{(0)} \mid \hat{H}^{(1)}\Psi^{(0)}\rangle \\ E^{(2)} &= \langle\Psi^{(0)} \mid \hat{H}^{(1)}\Psi^{(1)}\rangle \end{aligned} \tag{4.19}$$

As it follows from equation 4.19, the first order correction to the energy is the expectation value of the perturbation with the unperturbed wave function and to find the second order correction to the energy the first order correction to the wave function is required. To determine this correction we expand $\Psi^{(1)}$ in terms of the basis functions $\Psi_k^{(0)}$, equation 4.20, which form a complete set. To find the C_k coefficients we substitute the expansion, equation 4.20, into the λ^1 expression in equation 4.17, multiply it from the left by $(\Psi_l^{(0)})^*$, and integrate it to obtain equation 4.21.

$$\Psi^{(1)} = \sum_{k\neq 0} C_k \Psi_k^{(0)} \tag{4.20}$$

In equation 4.20 the coefficient $C_0 = 0$ because of the intermediate normalization required earlier.

$$\begin{aligned} &\langle\Psi_l^{(0)} \mid \hat{H}^{(0)} \sum_{k\neq 0} C_k\Psi_k^{(0)}\rangle + \langle\Psi_l^{(0)} \mid \hat{H}^{(1)}\Psi^{(0)}\rangle = \\ &= E_0^{(0)}\langle\Psi_l^{(0)} \mid \sum_{k\neq 0} C_k\Psi_k^{(0)}\rangle + E_0^{(1)}\langle\Psi_l^{(0)} \mid \Psi^{(0)}\rangle \\ &\sum_{k\neq 0} C_k E_k^{(0)}\langle\Psi_l^{(0)} \mid \Psi_k^{(0)}\rangle + \langle\Psi_l^{(0)} \mid \hat{H}^{(1)}\Psi^{(0)}\rangle = E_0^{(0)}\sum_{k\neq 0} C_k\langle\Psi_l^{(0)} \mid \Psi_k^{(0)}\rangle \\ &C_l E_l^{(0)} + \langle\Psi_l^{(0)} \mid \hat{H}^{(1)}\Psi^{(0)}\rangle = E_0^{(0)} C_l \\ &C_l = \frac{\langle\Psi_l^{(0)} \mid \hat{H}^{(1)}\Psi^{(0)}\rangle}{E_0^{(0)} - E_l^{(0)}} \end{aligned} \tag{4.21}$$

Substitution of this result into equation 4.20 gives the first order correction to the wave function, equation 4.22, and the second order correction to the energy, equation 4.23. Higher order corrections are more complex and could be derived in a similar way.

$$\Psi^{(1)} = \sum_{k\neq 0} \frac{\langle\Psi_k^{(0)} \mid \hat{H}^{(1)}\Psi^{(0)}\rangle}{E^{(0)} - E_k^{(0)}}\Psi_k^{(0)} \tag{4.22}$$

$$E^{(2)} = \sum_{k\neq 0} \frac{\langle\Psi^{(0)} \mid \hat{H}^{(1)}\Psi_k^{(0)}\rangle\langle\Psi_k^{(0)} \mid \hat{H}^{(1)}\Psi^{(0)}\rangle}{E^{(0)} - E_k^{(0)}} \tag{4.23}$$

Before the perturbation equations could be applied to the real system, the reference Schrödinger equation must be solved exactly. This is accomplished by the Hartree-Fock (HF) method, which is discussed in the next section. An extension of this Self-Consistent Field (SCF) method, which includes electron correlation, is discussed in section 4.3.

4.2 Hartree-Fock Theory

The HF theory resolves two problems with the electronic Schrödinger equation: (i) it imposes proper antisymmetry on the wave function; and (ii) it separates the equation by replacing $\hat{V}_{elec-elec}$ with a one-electron additive operator – a mean field operator. In the HF method [112] the total wave function is represented as an antisymmetrized product of wave functions of individual electrons. The total wave function Ψ has a form of the Slater determinant, equation 4.24, and individual electron wave functions ϕ_i, molecular spinorbitals, equation 4.25, are orthonormal products of spin (α or β) and spatial (φ_i) functions.

$$\Psi = \frac{1}{\sqrt{N!}} \begin{vmatrix} \phi_1(x_1) & \phi_1(x_2) & \cdots & \phi_1(x_N) \\ \phi_2(x_1) & \phi_2(x_2) & \cdots & \phi_2(x_N) \\ \vdots & \vdots & \ddots & \vdots \\ \phi_N(x_1) & \phi_N(x_2) & \cdots & \phi_N(x_N) \end{vmatrix} \tag{4.24}$$

$$\phi_i(x_i) = \phi_i(\boldsymbol{r}_i, \sigma_i) = \varphi_{i1}(\boldsymbol{r}_i)\alpha(\sigma_i) + \varphi_{i2}(\boldsymbol{r}_i)\beta(\sigma_i) \tag{4.25}$$

In equation 4.25 $x_i \equiv \{\boldsymbol{r}_i, \sigma_i\}$ is a generalized coordinate, which includes position and spin; σ_i is the spin coordinate of an electron, and in the majority of calculations either $\varphi_{i1} = 0$ or $\varphi_{i2} = 0$.

To obtain the mean value of the electronic Hamiltonian $\hat{H}'_{elec}$, which does not have the nuclear repulsion term, the Slater-Condon rules for identical Slater determinants [112, p. 989], equation 4.26, are applied leading to equation 4.27 written in atomic units, which are used thereafter.

$$\begin{aligned} \langle \Psi \mid \hat{O}_1 \Psi \rangle &= \sum_i \langle \phi_i \mid \hat{o}_1 \phi_i \rangle \\ \langle \Psi \mid \hat{O}_2 \Psi \rangle &= \sum_{i<j} \left(\langle \phi_i \phi_j \mid \hat{o}_2 \phi_i \phi_j \rangle - \langle \phi_i \phi_j \mid \hat{o}_2 \phi_j \phi_i \rangle \right) \end{aligned} \tag{4.26}$$

In equation 4.26 $\hat{O}_1 = \sum_i \hat{o}_1(i)$ is the sum of one electron operators, with $\hat{o}_1(i)$ acting on the electron i; $\hat{O}_2 = \sum_{i<j} \hat{o}_2(i,j)$ is the sum of two electron operators, with $\hat{o}_2(i,j)$ acting on the electrons i and j.

$$
\begin{aligned}
&\langle \Psi \mid \hat{H}'_{elec}\Psi\rangle = \sum_i \langle \phi_i \mid \left[-\frac{1}{2}\nabla^2(i) - \sum_I \frac{Z_I}{|\boldsymbol{r}_i - \boldsymbol{R}_I|}\right]\phi_i\rangle + \\
&+ \sum_{i<j}\left(\langle \phi_i\phi_j \mid \frac{1}{r_{ij}}\phi_i\phi_j\rangle - \langle \phi_i\phi_j \mid \frac{1}{r_{ij}}\phi_j\phi_i\rangle\right) = \\
&= \sum_i \int \phi_i^*(x_i)\left[-\frac{1}{2}\nabla^2(i) - \sum_I \frac{Z_I}{|\boldsymbol{r}_i - \boldsymbol{R}_I|}\right]\phi_i(x_i)dx_i + \\
&+ \sum_{i<j}\int \phi_i^*(x_i)\phi_j^*(x_j)\frac{1}{r_{ij}}\left(\phi_i(x_i)\phi_j(x_j) - \phi_j(x_i)\phi_i(x_j)\right)dx_i dx_j
\end{aligned}
\tag{4.27}
$$

In equation 4.27 $r_{ij} \equiv |\boldsymbol{r}_i - \boldsymbol{r}_j|$.

To obtain HF equations, the energy $E_{\mathrm{HF}} = \langle \Psi \mid \hat{H}'_{elec}\Psi\rangle$ is minimized keeping the orthonormality constraints $\langle \phi_i \mid \phi_j\rangle - \delta_{ij} = 0$ of molecular orbitals. This constrained search for optimal orbitals leads to equation 4.28.

$$
\begin{aligned}
&\hat{f}\phi_i(x_i) + \sum_j \left(\int \phi_j^*(x_j)\frac{1}{r_{ij}}\phi_j(x_j)dx_j \cdot \phi_i(x_i) - \int \phi_j^*(x_j)\frac{1}{r_{ij}}\phi_i(x_j)dx_j \cdot \phi_j(x_i)\right) = \\
&= \hat{f}\phi_i(x_i) + \sum_j \left(\hat{J}_j - \hat{K}_j\right)\phi_i(x_i) = \hat{f}\phi_i(x_i) + \hat{V}_{\mathrm{HF}}\phi_i(x_i) = \\
&= \hat{F}\phi_i(x_i) = \varepsilon_i\phi_i(x_i)
\end{aligned}
\tag{4.28}
$$

In equation 4.28 $\hat{f}$ is the one electron operator accounting for electron kinetic energy and its interaction with nuclei; $\hat{J}$ and $\hat{K}$ are Coulomb and exchange operators; $\hat{V}_{\mathrm{HF}}$ is the HF mean field operator; $\hat{F}$ is the one electron Fock operator; ε_i is the energy of the spinorbital ϕ_i.

The sum of orbital energies is given by equation 4.29 and it is not equal to the HF energy, equation 4.27, as it double counts the Coulomb and exchange terms.

$$
\begin{aligned}
\sum_i \varepsilon_i &= \sum_i \langle \phi_i \mid \hat{F}\phi_i\rangle = \\
&= \sum_i \langle \phi_i \mid \hat{f}\phi_i\rangle + \sum_i\sum_j \left(\langle \phi_i\phi_j \mid \frac{1}{r_{ij}}\phi_i\phi_j\rangle - \langle \phi_i\phi_j \mid \frac{1}{r_{ij}}\phi_j\phi_i\rangle\right)
\end{aligned}
\tag{4.29}
$$

By comparison of equations 4.27 and 4.29 the correct expression for the HF energy of a system could be written in the form of equation 4.30.

$$
E_{\mathrm{HF}} = \frac{1}{2}\sum_i \varepsilon_i + \frac{1}{2}\sum_i \langle \phi_i \mid \hat{f}\phi_i\rangle \tag{4.30}
$$

4.3 Density Functional Theory

Let us consider some properties of the ground state electronic wave function $\Psi_0(\boldsymbol{r}, \boldsymbol{R})$, for now, disregarding its dependence on spin. In the radial part of the electronic Schrödinger equation written in spherical coordinates and centered at $\boldsymbol{R}_I = 0$, there are terms shown in equation 4.31, which lead to a nuclear cusp condition[1], equation 4.32, preventing singularities when an electron i is close to a nucleus I, [112, p. 506].

$$\left(-\frac{1}{\boldsymbol{r}_i}\frac{\partial}{\partial \boldsymbol{r}_i} - \frac{Z_I}{|\boldsymbol{r}_i - \boldsymbol{R}_I|}\right)\Psi_0(\boldsymbol{r}, \boldsymbol{R}) \tag{4.31}$$

$$\frac{\partial}{\partial \boldsymbol{r}_i}\Psi_0(\boldsymbol{r}, \boldsymbol{R})\Big|_{\boldsymbol{r}_i \to \boldsymbol{R}_I} = -Z_I\Psi_0(\boldsymbol{r}, \boldsymbol{R}) \tag{4.32}$$

When two electrons i and j are close to each other, a term shown in equation 4.33 would not result in a singularity if equation 4.34 holds.

$$\left(-2\frac{1}{\boldsymbol{r}_{ij}}\frac{\partial}{\partial \boldsymbol{r}_{ij}} + \frac{1}{\boldsymbol{r}_{ij}}\right)\Psi_0(\boldsymbol{r}, \boldsymbol{R}) \tag{4.33}$$

$$\frac{\partial}{\partial \boldsymbol{r}_{ij}}\Psi_0(\boldsymbol{r}, \boldsymbol{R})\Big|_{\boldsymbol{r}_{ij} \to 0} = \frac{1}{2}\Psi_0(\boldsymbol{r}, \boldsymbol{R}) \tag{4.34}$$

Let us now define the electron density as an integral of the wave function squared over spin coordinates of all electrons and over spatial coordinates of all but one electron, equation 4.35.

$$\rho(\boldsymbol{r}_1) = N\int \Psi_0^*(\boldsymbol{r}_1, \boldsymbol{r}_2, ...\boldsymbol{r}_N, \boldsymbol{R})\Psi_0(\boldsymbol{r}_1, \boldsymbol{r}_2, ...\boldsymbol{r}_N, \boldsymbol{R})d\boldsymbol{r}_2 d\boldsymbol{r}_3 ... d\boldsymbol{r}_N \tag{4.35}$$

Having this definition of electronic density it is easy to show that the nuclear cusp condition can be expressed in terms of electronic density according to equation 4.36.

$$\begin{aligned}\frac{\partial}{\partial \boldsymbol{r}_1}\rho(\boldsymbol{r}_1) &= N\int\left(\frac{\partial}{\partial \boldsymbol{r}_1}\Psi_0^*(\boldsymbol{r}, \boldsymbol{R})\Psi_0(\boldsymbol{r}, \boldsymbol{R}) + \Psi_0^*(\boldsymbol{r}, \boldsymbol{R})\frac{\partial}{\partial \boldsymbol{r}_1}\Psi_0(\boldsymbol{r}, \boldsymbol{R})\right)d\boldsymbol{r}_2 d\boldsymbol{r}_3 ... d\boldsymbol{r}_N = \\ &= -2Z_I N\int \Psi_0^*(\boldsymbol{r}, \boldsymbol{R})\Psi_0(\boldsymbol{r}, \boldsymbol{R})d\boldsymbol{r}_2 d\boldsymbol{r}_3 ... d\boldsymbol{r}_N = \\ &= -2Z_I\rho(\boldsymbol{r}_1)\end{aligned} \tag{4.36}$$

The equation 4.36 demonstrates that the ground state electronic density could be used to locate positions of nuclei (the cusps of the electron density) and their charges

[1]Shown in equation 4.31 terms are both proportional to $1/\boldsymbol{r}_i$ and must cancel out each other when $\boldsymbol{r}_i \to 0$.

("strength" of the cusps $-2Z_I$). Integration of the electronic density over the whole space results in the total number of electrons in a system. Thus there is enough information in the ground state electronic density to find N, $\boldsymbol{R}$, $\{Z_1, Z_2, ...Z_I, ...Z_A\}$, and to determine the electronic Hamiltonian.

Formal theoretical grounds for the Density Functional Theory (DFT) were established by two theorems of Hohenberg and Kohn (Hohenberg-Kohn (HK)) [114]. The first theorem states equivalence of the electronic wave function and electronic density [112]: The ground state electronic density $\rho_0(x)$ and the ground state wave function $\Psi_0(x_1, x_2, ...x_N)$ can be used alternatively as full descriptions of the ground state of a system. The second theorem states the existence of an energy functional minimized by $\rho = \rho_0$ [112]: For a given number of electrons and an external potential $u(r) \equiv u(x)$, there exists a functional of ρ, denoted by $E_u^{\mathrm{HK}}[\rho]$, for which the variational principle, equation 4.37, is satisfied. Here, and further on, r is used as a position vector and we omit the dependence of Ψ_0 on $\boldsymbol{R}$.

$$E_u^{\mathrm{HK}}[\rho] \geq E_u^{\mathrm{HK}}[\rho_0] = E_0 \tag{4.37}$$

For some external potential $u(x)$ defining the Hamiltonian and the ground state of a many electron system, the energy functional of electronic density could be written in a general form presented in equation 4.38.

$$E_u^{\mathrm{HK}}\left[\rho(x)\right] = T\left[\Psi_0\left[u\left[\rho(x)\right]\right]\right] + V\left[\Psi_0\left[u\left[\rho(x)\right]\right]\right] + \int u(x)\rho(x)dx \tag{4.38}$$

In equation 4.38 $T\left[\rho(x)\right]$ is the kinetic energy of the many electron system; $V\left[\rho(x)\right]$ is the electron-electron interaction energy; the last integral accounts for the interaction of electron density with the external potential.

The second HK theorem provides no information about the form of $T\left[\rho(x)\right]$ and $V\left[\rho(x)\right]$, it simply says they exist. To overcome the obstacle and to construct the functional, equation 4.38, Kohn and Sham introduced a fictitious system of non interacting electrons subjected to an external potential [115].

In the Kohn-Sham (KS) formalism the kinetic energy of a many electron system is evaluated as the kinetic energy of non interacting particles T_0, equation 4.39, and the particle density is defined as in the HF formalism, equation 4.35, where the ground state wave function Ψ_0 is a single Slater determinant. It could be shown, applying the Slater-Condon rule, equation 4.26 for a one electron operator, that equation 4.35 may be written in the form of equation 4.40, where the summation is also running over the spin coordinate.

$$T_0\left[\Psi_0\right] = \langle \Psi_0 \mid \hat{T}\Psi_0 \rangle = -\frac{1}{2}\sum_i \langle \phi_i \mid \nabla^2\phi_i \rangle = -\frac{1}{2}\sum_i \int \phi_i^*(x)\nabla^2\phi_i(x)dx \tag{4.39}$$

$$\rho(x) = \sum_i \phi_i^*(x)\phi_i(x) \tag{4.40}$$

For real interacting particles with the kinetic energy T, the usage of T_0 introduces an error which is assigned to an undefined part in the energy functional – exchange-correlation energy E_{XC}. The neglect of interactions also means that one particle wave functions are not true wave functions but some pseudofunctions or KS orbitals. The variational approach is applied to search for such pseudofunctions which minimize the energy functional equation 4.41.

$$E_u^{\mathrm{HK}}\left[\rho(x)\right] = T_0\left[\rho(x)\right] + \frac{1}{2}\int \frac{\rho(x)\rho(x')}{|r-r'|}dxdx' + E_{XC}\left[\rho(x)\right] + \int u(x)\rho(x)dx \tag{4.41}$$

In equation 4.41 the second term accounts for Coulomb interaction of electronic cloud with itself, including self-interaction; $E_{XC} = E'_{XC} + (T[\rho(x)] - T_0[\rho(x)])$ is the sum of exchange-correlation energy E'_{XC} and the difference of kinetic energies of the real system and model system of non-interacting particles.

Requiring variations of the total energy δE_u^{HK} due to variations $\delta\phi_i^*$ of the spinorbitals to be zero, equation 4.42, one obtains a system of equations, equation 4.43, analogous to the HF equations [116].

$$\frac{\delta}{\delta\phi_i^*}\left(E_u^{\mathrm{HK}} - \varepsilon_i\left[\int \rho(x)dx - N\right]\right) = 0 \tag{4.42}$$

In equation 4.42 $\int \rho(x)dx - N = 0$ is a normalization constraint on the electron density; ε_i are the Lagrange multipliers maintaining normalization of the density.

$$\left[-\frac{1}{2}\nabla^2 + \int \frac{\rho(x')}{|r-r'|}dx' + V_{XC}(x) + u(x)\right]\phi_i(x) = \varepsilon_i\phi_i(x) \tag{4.43}$$

In equation 4.43 V_{XC} is the exchange correlation potential, which depends on the density distribution in the whole space.

To find the total energy, equation 4.44, we substitute T_0 from equation 4.39 to equation 4.41 with the $-\frac{1}{2}\nabla^2\phi_i$ term found from equation 4.43.

$$\begin{aligned} E_u^{\mathrm{HK}}\left[\rho(x)\right] = &\sum_i \int \phi_i^*(x)\left[\varepsilon_i - \int \frac{\rho(x')}{|r-r'|}dx' - V_{XC}(x) - u(x)\right]\phi_i(x)dx + \\ &+ \frac{1}{2}\int \frac{\rho(x)\rho(x')}{|r-r'|}dxdx' + E_{XC}\left[\rho(x)\right] + \int u(x)\rho(x)dx = \\ &= \sum_i \varepsilon_i - \frac{1}{2}\int \frac{\rho(x)\rho(x')}{|r-r'|}dxdx' - \int V_{XC}(x)\rho(x)dx + E_{XC}\left[\rho(x)\right] \end{aligned} \tag{4.44}$$

In equation 4.44, ε_i's are the lowest eigenvalues of the KS equations, and are interpreted as the energies of KS orbitals.

The exact dependence of the exchange-correlation energy in equation 4.41 on the electronic density has not been identified in the work of Kohn and Sham and remains unknown up to now. There exist many approximations for this dependence, which could be categorized into two large groups: the Local Density Approximation (LDA) and the Generalized Gradient Approximation (GGA). In the LDA electronic properties (mostly the exchange and correlation energy but could be even kinetic energy like in the Thomas-Fermi model) are determined locally as functionals of the electronic density of a homogeneous electron system with $\rho = N/V$, where N is the total number of electrons and V is the volume. One example would be the Wigner correlation functional [117], equation 4.45.

$$E_C = -4a \int \frac{\rho_\alpha(r)\rho_\beta(r)}{\rho(r)} \left(\frac{1}{1 + b\rho^{-1/3}(r)} \right) dr \tag{4.45}$$

In equation 4.45 $\rho_\alpha(r)$ is the density of electrons with α spin; $\rho_\beta(r)$ is the density of electrons with β spin; $\rho(r) = \rho_\alpha(r) + \rho_\beta(r)$; a and b are parameters.

The exchange-correlation energy depends not only on local electronic density, an assumption of the LDA, but in general on the density in the whole space. An approach to somehow take nonlocality into account is to construct functionals which depend not only on the electronic density itself but also on its gradient. In contemporary computational chemistry and materials science this is known as the GGA. An example of this approach is the Perdew and Yue exchange functional [118], equation 4.46.

$$E_X = -\frac{3}{4} \left(\frac{3}{\pi} \right)^{1/3} \int \rho^{4/3} F(s) dr \tag{4.46}$$

In equation 4.46 $s = \frac{|\nabla\rho(r)|}{2k_F\rho}, k_F = (3\pi^2\rho)^{1/3}$; $F(s) = (1 + 1.296s^2 + 14s^4 + 0.2s^6)^{1/15}$.

4.4 Density Functional Theory with Empirical Dispersion Corrections

The standard KS DFT includes electron correlation effects only approximately and all GGA functionals are unable to describe dispersive interactions [119]. Taking into account that the DFT is an extensively used electronic structure calculation method and the fact that dispersion forces are pervasive and are responsible for structure of biomolecules, packing of crystals, and, most importantly for this work, they play a major role in stabilization of host-guest compounds, the deficiency of DFT in describing electron correlation has been attacked with a noticeable success [120]. According to Stefan Grimme all nonempirical approaches to include van der Waals interactions into the DFT would result in methods as complex and as demanding

computationally as the wave function methods like MP2, thus undermining the main advantage of DFT – its computational efficiency. The only practical scheme to maintain efficiency along with the accountability for dispersion is to add an empirical potential of the form $C_6 R^{-6}$, with C_6 being the dispersion coefficient and R being interatomic distance, to usual DFT [119], equation 4.47.

$$E_{\mathrm{DFT-D}} = E_{\mathrm{KS-DFT}} + E_{\mathrm{disp}} \tag{4.47}$$

The total energy $E_{\mathrm{DFT-D}}$ in equation 4.47 is the sum of the usual KS DFT electronic energy $E_{\mathrm{KS-DFT}}$ and an empirical dispersion correction E_{disp} given by equation 4.48.

$$E_{\mathrm{disp}} = -s_6 \sum_{i=1}^{N_{\mathrm{at}}-1} \sum_{j=i+1}^{N_{\mathrm{at}}} \frac{C_6^{ij}}{R_{ij}^6} f_{\mathrm{dmp}}(R_{ij}) \tag{4.48}$$

In equation 4.48 s_6 is a global scaling factor, which depends on the exchange-correlation functional; N_{at} is the number of atoms in the system; C_6^{ij} is the dispersion coefficient for an atom pair ij; R_{ij} is an interatomic distance; f_{dmp} is a damping function, which suppresses the dispersion correction at short distances between atoms.

The damping function, equation 4.49, allows avoiding near-singularities when R_{ij} is small and suppresses dispersion corrections at distances where usual DFT does reasonably well on its own.

$$f_{\mathrm{dmp}}(R_{ij}) = \frac{1}{1 + e^{-d(R_{ij}/R_r - 1)}} \tag{4.49}$$

In equation 4.49 d is a parameter determining the steepness of the damping function; R_r is the sum of atomic van der Waals radii.

The composed dispersion coefficients C_6^{ij} are found from atomic coefficients C_6^i as a geometric mean, equation 4.50.

$$C_6^{ij} = \sqrt{C_6^i C_6^j} \tag{4.50}$$

The usage of fixed C_6 coefficients obtained for free atoms is a significant limitation of the Density Functional Theory with empirical Dispersion corrections (DFT-D) approach. Changing of electronic character of an atom in its molecular environment requires, in principle, derivation of these coefficients from molecular properties [120].

4.5 Implementation of Calculation Methods

4.5.1 Reduction to Matrix Eigenvalue Problem

As similar approaches are used to solve both the HF and the KS equations we first show that equation 4.28 can be written in the form similar to equation 4.43 and

then we discuss practical solution methods for this general representation of the HF and the KS equations. The kinetic energy terms in both formalisms are equivalent and equivalence between the remaining terms is presented in equation 4.51.

$$\begin{aligned}
\int \frac{\rho(x')}{|r-r'|}dx'\phi_i(x) &\equiv \sum_j \left(\int \phi_j^*(x') \frac{1}{|r-r'|}\phi_j(x')dx' \cdot \phi_i(x) \right) \equiv \\
&\equiv \sum_j \left(\int \phi_j^*(x_j) \frac{1}{r_{ij}}\phi_j(x_j)dx_j \cdot \phi_i(x_i) \right) \\
V_{XC}\phi_i(x) &\equiv -\sum_j \left(\int \phi_j^*(x') \frac{1}{|r-r'|}\phi_i(x')dx' \cdot \phi_j(x) \right) \equiv \\
&\equiv -\sum_j \left(\int \phi_j^*(x_j) \frac{1}{r_{ij}}\phi_i(x_j)dx_j \cdot \phi_j(x_i) \right) \\
u(x)\phi_i(x) &\equiv -\sum_I \frac{Z_I}{|r-\boldsymbol{R}_I|}\phi_i(x) \equiv -\sum_I \frac{Z_I}{|\boldsymbol{r}_i-\boldsymbol{R}_I|}\phi_i(x_i)
\end{aligned} \tag{4.51}$$

Integro-differential equations of the kind presented in equations 4.28 and 4.43 may be reduced to a matrix eigenvalue problem by expanding one-electron functions over a limited set of known functions $\{\psi_p\}$ – a basis set, equation 4.52.

$$\phi_i(x) = \sum_p C_{ip}\psi_p(x) \tag{4.52}$$

In equation 4.52 C_{ip} are the expansion coefficients.

Substitution of equation 4.52 in equations 4.28 or 4.43 results in equation 4.53.

$$\sum_p C_{ip}\widetilde{H}\psi_p(x) = \varepsilon_i \sum_p C_{ip}\psi_p(x) \tag{4.53}$$

In equation 4.53 $\widetilde{H}$ is an effective one-electron Hamiltonian typical for the HF or the KS theory.

Multiplying equation 4.53 from the left by $\psi_q^*(x)$ and integrating over the whole space one obtains a system of algebraic equations in the expansion coefficients C_{ip}, equation 4.54, with the overlap matrix elements S_{qp} and the matrix elements of the Hamiltonian H_{qp} defined by equations 4.55 and 4.56, respectively [116].

$$\sum_p C_{ip} \int \psi_q^*(x)\widetilde{H}\psi_p(x)dx = \varepsilon_i \sum_p C_{ip} \int \psi_q^*(x)\psi_p(x)dx \tag{4.54}$$

$$S_{qp} \equiv \int \psi_q^*(x)\psi_p(x)dx \tag{4.55}$$

$$
\begin{aligned}
H_{qp} &\equiv \int \psi_q^*(x)\widetilde{H}\psi_p(x)dx = \\
&= \int \psi_q^*(x)\left[-\frac{1}{2}\nabla^2 + \int \frac{\rho(x')}{|r-r'|}dx' + V_{XC}(x) + u(x)\right]\psi_p(x)dx
\end{aligned}
\tag{4.56}
$$

By substituting equation 4.52 into equation 4.40 the density can be expressed in terms of expansion coefficients and basis functions, equation 4.57.

$$
\rho(x) = \sum_i \phi_i^*(x)\phi_i(x) = \sum_{pq}\left[\sum_i C_{iq}^* C_{ip}\right]\psi_q^*(x)\psi_p(x) \tag{4.57}
$$

In equation 4.57 $D_{pq} \equiv \sum_i C_{iq}^* C_{ip}$ is the density matrix.

The dependence of the effective Hamiltonian on unknown coefficients through ρ and V_{XC} allows only for an iterative solution of equation 4.54. For a trial set of coefficients one constructs the Hamiltonian and solves the resulting system of linear equations, equation 4.54, by diagonalization. The N lowest eigenvalues and related eigenvectors are then used for next iteration until convergence is reached. To prevent instability of expansion coefficients a damping parameter $\beta < 1$ is used to calculate the next set of expansion coefficients according to equation 4.58 [116].

$$
C^{next} = \beta C^{new} + (1-\beta)C^{old} \tag{4.58}
$$

4.5.2 Atom-Centered Basis Functions

Important and widely used analytical atom-centered basis functions are Slater-Type Orbitals (STOs) and Gaussian-Type Orbitals (GTOs). An advantage of STOs, equation 4.59, is that they may satisfy the nuclear cusp condition, equation 4.32, and decay with distance in a way similar to hydrogen atom orbitals [112].

$$
\psi_{\mathrm{STO}}(r, \boldsymbol{\theta}, \boldsymbol{\phi}) \sim f(r)e^{-\zeta r}Y_{lm}(\boldsymbol{\theta}, \boldsymbol{\phi}) \tag{4.59}
$$

In equation 4.59 $f(r)$ is a polynomial; ζ is an effective nuclear charge; $Y_{lm}(\boldsymbol{\theta}, \boldsymbol{\phi})$ is the spherical harmonic.

GTOs, equation 4.60, do not have correct cusps, but integrals involved in calculation of matrix elements can be evaluated analytically. Moreover, a product of two Gaussians is also a Gaussian, or a linear combination of Gaussians (Gaussian product rule) [112]. This feature of GTOs reduces evaluation of four-center integrals to a two-center problem.

$$
\psi_{\mathrm{GTO}}(r, \boldsymbol{\theta}, \boldsymbol{\phi}) \sim f(r)e^{-\alpha r^2}Y_{lm}(\boldsymbol{\theta}, \boldsymbol{\phi}) \tag{4.60}
$$

Neither STOs nor GTOs have the correct node structure of hydrogen-like or-

bitals, only a combination of several STOs with various exponents ζ's simulates the nodes [116]. These linear combinations are called "double-ζ", "triple-ζ", "quadruple-ζ" and so on, or "minimal basis" when only one exponent is included. The same terminology is applied to GTOs, though the convergence in terms of GTOs is slower than in STOs.

4.5.3 Plane Waves and Pseudopotentials

According to Bloch's theorem the wave function of an electron in a periodic crystal potential has the form of a plane wave multiplied by a prefactor with lattice periodicity, equation 4.61 [121].

$$\phi_j(r) = U_j(r)e^{i\mathbf{k}\cdot r} \tag{4.61}$$

In equation 4.61 $\mathbf{k}$ is the wave vector confined to the Brillouin zone (a primitive cell of the reciprocal lattice).

The periodic part of the wave function can be expanded in a discrete set of plane waves, the wave vectors of which are reciprocal lattice vectors of the crystal, equation 4.62.

$$U_j(r) = \sum_{\mathbf{G}} C_{j,\mathbf{G}} e^{i\mathbf{G}\cdot r} \tag{4.62}$$

In equation 4.62 $C_{j,\mathbf{G}}$ are the expansion coefficients; $\mathbf{G}$ are the reciprocal lattice vectors defined as $\mathbf{G}\cdot\boldsymbol{l} = 2\pi n$, where $\boldsymbol{l}$ is a lattice vector of the crystal and n is an integer.

A combination of equations 4.61 and 4.62 gives the electronic wave function expressed as a linear combination of plane waves, equation 4.63.

$$\phi_j(r) = \sum_{\mathbf{G}} C_{j,\mathbf{k}+\mathbf{G}} \frac{1}{\sqrt{\Omega}} e^{i(\mathbf{k}+\mathbf{G})\cdot r} \tag{4.63}$$

In equation 4.63 Ω is a volume of the unit cell, and $1/\sqrt{\Omega}$ is a normalization constant.

Substitution of equation 4.63 into equation 4.43 followed by multiplication from the left by $\frac{1}{\sqrt{\Omega}} e^{-i(\mathbf{k}+\mathbf{G}')\cdot r}$ and integration over r results in a plane wave representation of the Kohn-Sham equations, equation 4.64 [122]. Here we used orthonormality of plane waves $\langle \psi_{\mathbf{G}'} \mid \psi_{\mathbf{G}} \rangle = \delta_{\mathbf{G}'\mathbf{G}}$, where $\psi_{\mathbf{G}}(r) = \frac{1}{\sqrt{\Omega}} e^{i\mathbf{G}\cdot r}$.

$$\sum_{\mathbf{G}} \left[\frac{1}{2}|\mathbf{k}+\mathbf{G}'|^2 \delta_{\mathbf{G}'\mathbf{G}} + V_H(\mathbf{G}-\mathbf{G}') + V_{XC}(\mathbf{G}-\mathbf{G}') + u(\mathbf{G}-\mathbf{G}') \right] C_{j,\mathbf{k}+\mathbf{G}} = \\ = \varepsilon_j C_{j,\mathbf{k}+\mathbf{G}'} \tag{4.64}$$

In equation 4.64 $V_H(\mathbf{G}-\mathbf{G}')$, $V_{XC}(\mathbf{G}-\mathbf{G}')$, $u(\mathbf{G}-\mathbf{G}')$ are Fourier transforms of the Hartree, exchange-correlation, and ionic potentials, respectively.

Equation 4.64 is solved by diagonalization of a matrix with matrix elements $H^{\mathbf{k}}_{\mathbf{G}'\mathbf{G}}$ given by equation 4.65 [116].

$$H^{\mathbf{k}}_{\mathbf{G}'\mathbf{G}} = \frac{1}{2}|\mathbf{k}+\mathbf{G}'|^2\delta_{\mathbf{G}'\mathbf{G}} + \frac{1}{\Omega^2}\sum_{\mathbf{G}_1\mathbf{G}_2} D^{\mathbf{k}}_{\mathbf{G}_1\mathbf{G}_2}\int\int \frac{e^{i(\mathbf{G}-\mathbf{G}')r}e^{i(\mathbf{G}_2-\mathbf{G}_1)r'}}{|r-r'|}drdr' + \\ + \frac{1}{\Omega}\int e^{i(\mathbf{G}-\mathbf{G}')r}V_{XC}(r)dr + \frac{1}{\Omega}\int e^{i(\mathbf{G}-\mathbf{G}')r}u(r)dr \tag{4.65}$$

In equation 4.65 $D^{\mathbf{k}}_{\mathbf{G}_1\mathbf{G}_2}$ is the density matrix introduced in equation 4.57.

In accordance with the Bloch's theorem, an infinite number of plane waves from a discrete set are required to expand electronic wave functions at each $\mathbf{k}$ point, equation 4.63. Plane waves with small kinetic energy are more important and thus the plane wave basis set may be limited to plane waves with kinetic energy less than some threshold $\frac{1}{2}|\mathbf{k}+\mathbf{G}_C|^2$, where $\mathbf{G}_C$ is some cutoff value of $\mathbf{G}$. At each $\mathbf{k}$ point a finite number of electronic states is occupied. However, the number of $\mathbf{k}$ points in the Brillouin zone is infinite. Due to the fact that the electronic wave functions at close $\mathbf{k}$ points are very similar, calculations of the electronic states at some set of $\mathbf{k}$ points covering certain regions of the $\mathbf{k}$ space (reciprocal space) reduce the infinite problem to finite and tractable [122]. In practical calculations convergence tests are used to obtain optimum values for the kinetic energy cutoff and for the density of $\mathbf{k}$ points.

As a large number of plane waves is required to expand core orbitals and to reproduce shape of wave functions of valence electrons in the core region, further approximation is used to reduce the size of the plane wave basis set. Due to the fact that the core electrons are highly localized and chemically inert the pseudopotential approximation replaces them and strong ionic potentials with weaker (screened) pseudopotentials acting on pseudo wave functions of valence electrons. Beyond certain cutoff radius pseudo wave functions and pseudopotential are identical to true wave functions and true potentials. Within the cutoff radius, pseudo wave functions and pseudopotential are both smoother than the true ones and in addition pseudo wave functions do not have radial nodes, and pseudopotentials are more shallow.

Pseudopotentials are constructed in the following way. Firstly, valence electrons wave functions and eigenvalues are obtained from all-electron calculations for an atom in its ground state and in some excited states using certain exchange-correlation functional. Next, a form of an ionic pseudopotential (certain parameterization) is selected. Parameters of the selected form of pseudopotential are then adjusted, using the same exchange-correlation functional as for all-electron calculations, to get an agreement between pseudo wave functions and all-electron wave

functions beyond the cutoff radius and between pseudo eigenvalues and valence eigenvalues [122]. Obtained in such a way pseudopotential, along with the same exchange-correlation functional, is then used for electronic density calculations in any chemical environment without further modifications.

4.6 Correlated Methods

4.6.1 Møller-Plesset Perturbation Theory

In the Møller-Plesset (MP) version [123] of the Rayleigh-Schrödinger perturbation theory considered in section 4.1.4 the unperturbed operator is defined as a sum of the Fock operators, equation 4.66.

$$\hat{H}^{(0)}_{\mathrm{MP}} = \sum_i \hat{F}_i = \sum_i \left(\hat{f}_i + \sum_j \left(\hat{J}_j - \hat{K}_j \right) \right) \tag{4.66}$$

As follows from a comparison of equations 4.27 and 4.29, this sum double counts average (Hartree-Fock) electron-electron repulsion $\langle \hat{V}_{elec-elec} \rangle$. The perturbation $\hat{H}^{(1)}_{\mathrm{MP}}$ includes the exact electron-electron repulsion operator $\hat{V}_{elec-elec}$, equation 4.67, and standard Coulomb and exchange operators. Defined in such a way perturbation operator is called a fluctuation potential [113].

$$\hat{H}^{(1)}_{\mathrm{MP}} = \hat{H}'_{elec} - \hat{H}^{(0)}_{\mathrm{MP}} = \hat{V}_{elec-elec} - \sum_{ij} \left(\hat{J}_j - \hat{K}_j \right) \tag{4.67}$$

The zero order energy in the MP theory, equation 4.68, is just a sum of orbital energies and is totally analogous to equation 4.29. The first order correction to the energy $\triangle E_{\mathrm{MP1}}$ and the first order energy E_{MP1} are given in equation 4.69, where it is seen that the sum of the zero order energy and the first order correction yields the HF energy, equation 4.30.

$$E_{\mathrm{MP0}} = \langle \Psi_0 \mid \hat{H}^{(0)}_{\mathrm{MP}} \Psi_0 \rangle = \sum_i \langle \phi_i \mid \hat{F} \phi_i \rangle = \sum_i \varepsilon_i \tag{4.68}$$

$$\begin{aligned} \triangle E_{\mathrm{MP1}} &= \langle \Psi_0 \mid \hat{H}^{(1)}_{\mathrm{MP}} \Psi_0 \rangle = \\ &= \langle \Psi_0 \mid \hat{V}_{elec-elec} \Psi_0 \rangle - 2 \langle \hat{V}_{elec-elec} \rangle = - \langle \hat{V}_{elec-elec} \rangle \\ E_{\mathrm{MP1}} &= E_{\mathrm{MP0}} + \triangle E_{\mathrm{MP1}} = \sum_i \varepsilon_i - \langle \hat{V}_{elec-elec} \rangle = E_{\mathrm{HF}} \end{aligned} \tag{4.69}$$

In the MP theory electron correlation energy appears at the second order. To calculate the second order correction to the energy, matrix elements of the fluctuation potential between the reference wave function and all excited Slater determinants are required, equation 4.23. By virtue of the Slater-Condon rules all elements are equal

to zero, if the wave functions involved are different by three or more spinorbitals. This excludes triple and higher excitations. By virtue of the Brillouin's theorem all matrix elements of the form $\langle \Psi_0 \mid \hat{H}^{(1)}_{\mathrm{MP}} \Psi_1 \rangle$ are also zero. Thus the only elements left giving non zero contributions are matrix elements between the reference and doubly excited wave functions. The second order MP correction to the energy, $\triangle E_{\mathrm{MP2}}$, and the second order MP energy E_{MP2} are given in equation 4.70.

$$\begin{aligned} \triangle E_{\mathrm{MP2}} &= \sum_{i<j}^{\mathrm{occ}} \sum_{a<b}^{\mathrm{vir}} \frac{\langle \Psi_0 \mid \hat{H}^{(1)}_{\mathrm{MP}} \Psi^{ab}_{ij} \rangle \langle \Psi^{ab}_{ij} \mid \hat{H}^{(1)}_{\mathrm{MP}} \Psi_0 \rangle}{E_0 - E^{ab}_{ij}} \\ E_{\mathrm{MP2}} &= E_{\mathrm{MP0}} + \triangle E_{\mathrm{MP1}} + \triangle E_{\mathrm{MP2}} = \\ &= E_{\mathrm{HF}} + \sum_{i<j}^{\mathrm{occ}} \sum_{a<b}^{\mathrm{vir}} \frac{|\langle \phi_i \phi_j \mid \frac{1}{r_{ab}} \phi_a \phi_b \rangle - \langle \phi_i \phi_j \mid \frac{1}{r_{ab}} \phi_b \phi_a \rangle|^2}{\varepsilon_i + \varepsilon_j - \varepsilon_a - \varepsilon_b} \end{aligned} \tag{4.70}$$

In equation 4.70 "occ" denotes summation over occupied orbitals; "vir" denotes summation over virtual (unoccupied) orbitals. To get the explicit expression for $\triangle E_{\mathrm{MP2}}$ in terms of molecular orbitals we used the Slater-Condon rule for matrix elements, where the determinants involved are different by two orbitals.

4.6.2 Coupled Cluster Theory

In the Coupled Cluster (CC) theory the exact wave function of many electron system is expressed in the form of the following Ansatz, equation 4.71 [112, 124, 125].

$$\Psi_{\mathrm{CC}} = e^{\hat{\mathbf{T}}} \Psi_0 \tag{4.71}$$

In equation 4.71 $\hat{\mathbf{T}} = \hat{\mathbf{T}}_1 + \hat{\mathbf{T}}_2 + \hat{\mathbf{T}}_3 + ... + \hat{\mathbf{T}}_N$ is the cluster operator.

The operator $\hat{\mathbf{T}}_k$ generates all kth excitations upon acting on the ground state Slater determinant, equation 4.72.

$$\begin{aligned} \hat{\mathbf{T}}_1 \Psi_0 &= \sum_{i}^{\mathrm{occ}} \sum_{a}^{\mathrm{vir}} t^a_i \Psi^a_i \\ \hat{\mathbf{T}}_2 \Psi_0 &= \sum_{i<j}^{\mathrm{occ}} \sum_{a<b}^{\mathrm{vir}} t^{ab}_{ij} \Psi^{ab}_{ij} \\ &... \end{aligned} \tag{4.72}$$

In equation 4.72 $t^{ab\cdots}_{ij\ldots}$ are expansion coefficients, or cluster amplitudes.

In a search for the amplitudes $t^{ab\cdots}_{ij\ldots}$ we substitute the cluster operator into the Taylor expansion of the exponential function, which gives the following form of $e^{\hat{\mathbf{T}}}$, equation 4.73 [113].

$$
\begin{aligned}
e^{\hat{\mathbf{T}}} &= 1 + \hat{\mathbf{T}} + \frac{1}{2}\hat{\mathbf{T}}^2 + \frac{1}{6}\hat{\mathbf{T}}^3 + ... = \sum_{k=0}^{\infty} \frac{1}{k!}\hat{\mathbf{T}}^k = \\
&= 1 + \hat{\mathbf{T}}_1 + \left(\hat{\mathbf{T}}_2 + \frac{1}{2}\hat{\mathbf{T}}_1^2\right) + \left(\hat{\mathbf{T}}_3 + \hat{\mathbf{T}}_2\hat{\mathbf{T}}_1 + \frac{1}{6}\hat{\mathbf{T}}_1^3\right) + \\
&+ \left(\hat{\mathbf{T}}_4 + \hat{\mathbf{T}}_3\hat{\mathbf{T}}_1 + \frac{1}{2}\hat{\mathbf{T}}_2^2 + \frac{1}{2}\hat{\mathbf{T}}_2\hat{\mathbf{T}}_1^2 + \frac{1}{24}\hat{\mathbf{T}}_1^4\right) + ...
\end{aligned}
\tag{4.73}
$$

The electronic Schrödinger equation with the CC wave function reads, equation 4.74.

$$
\hat{H}'_{elec} e^{\hat{\mathbf{T}}} \Psi_0 = E_{\mathrm{CC}} e^{\hat{\mathbf{T}}} \Psi_0 \tag{4.74}
$$

Multiplication of equation 4.74 from the left by Ψ_0^* and integration result in equation 4.75.

$$
\begin{aligned}
\langle \Psi_0 \mid \hat{H}'_{elec} e^{\hat{\mathbf{T}}} \Psi_0 \rangle &= \langle \Psi_0 \mid E_{\mathrm{CC}} e^{\hat{\mathbf{T}}} \Psi_0 \rangle \\
\langle \Psi_0 \mid \hat{H}'_{elec} e^{\hat{\mathbf{T}}} \Psi_0 \rangle &= E_{\mathrm{CC}} \langle \Psi_0 \mid \left(1 + \hat{\mathbf{T}}_1 + \hat{\mathbf{T}}_2 + ...\right) \Psi_0 \rangle \\
E_{\mathrm{CC}} &= \langle \Psi_0 \mid \hat{H}'_{elec} e^{\hat{\mathbf{T}}} \Psi_0 \rangle
\end{aligned}
\tag{4.75}
$$

Upon substitution of equation 4.73 into the last expression of equation 4.75 and disregarding all matrix elements where the single determinant wave functions are different by three or more excitations (the Slater-Condon rules make these elements equal to zero) one obtains equation 4.76[2].

$$
\begin{aligned}
E_{\mathrm{CC}} &= \langle \Psi_0 \mid \hat{H}'_{elec} \left(1 + \hat{\mathbf{T}}_1 + \hat{\mathbf{T}}_2 + \frac{1}{2}\hat{\mathbf{T}}_1^2\right) \Psi_0 \rangle \\
E_{\mathrm{CC}} &= E_{\mathrm{HF}} + \sum_{i}^{\mathrm{occ}} \sum_{a}^{\mathrm{vir}} t_i^a \langle \Psi_0 \mid \hat{H}'_{elec} \Psi_i^a \rangle + \sum_{i<j}^{\mathrm{occ}} \sum_{a<b}^{\mathrm{vir}} \left(t_{ij}^{ab} + t_i^a t_j^b - t_i^b t_j^a\right) \langle \Psi_0 \mid \hat{H}'_{elec} \Psi_{ij}^{ab} \rangle \\
E_{\mathrm{CC}} &= E_{\mathrm{HF}} + \sum_{i<j}^{\mathrm{occ}} \sum_{a<b}^{\mathrm{vir}} \left(t_{ij}^{ab} + t_i^a t_j^b - t_i^b t_j^a\right) \left(\langle \phi_i \phi_j \mid \frac{1}{r_{ab}} \phi_a \phi_b \rangle - \langle \phi_i \phi_j \mid \frac{1}{r_{ab}} \phi_b \phi_a \rangle \right)
\end{aligned}
\tag{4.76}
$$

In equation 4.76 we used Brillouin's theorem, according to which $\langle \Psi_0 \mid \hat{H}'_{elec} \Psi_i^a \rangle = 0$, and explicit expressions for matrix elements involving determinants different by two orbitals were obtained according to the corresponding Slater-Condon rule.

[2] In equation 4.76 we used the symmetry of doubly excited Slater determinant $\Psi_{ij}^{ba} = -\Psi_{ij}^{ab}$ and $\hat{\mathbf{T}}_1^2 \Psi_0 = \sum_{i,j}^{\mathrm{occ}} \sum_{a,b}^{\mathrm{vir}} t_i^a t_j^b \Psi_{ij}^{ab} = \frac{1}{2}\left(\sum_{i,j}^{\mathrm{occ}} \sum_{a,b}^{\mathrm{vir}} t_i^a t_j^b \Psi_{ij}^{ab} + \sum_{i,j}^{\mathrm{occ}} \sum_{a,b}^{\mathrm{vir}} t_i^b t_j^a \Psi_{ij}^{ba}\right) =$
$\frac{1}{2}\left(4 \sum_{i<j}^{\mathrm{occ}} \sum_{a<b}^{\mathrm{vir}} t_i^a t_j^b \Psi_{ij}^{ab} + 4 \sum_{i<j}^{\mathrm{occ}} \sum_{a<b}^{\mathrm{vir}} t_i^b t_j^a \Psi_{ij}^{ba}\right) = 2 \sum_{i<j}^{\mathrm{occ}} \sum_{a<b}^{\mathrm{vir}} \left(t_i^a t_j^b - t_i^b t_j^a\right) \Psi_{ij}^{ab}$.

To derive equations for the CC amplitudes, one multiples equation 4.74 from the left by complex conjugate of excited determinants (singly, doubly, ...) and integration is done in a way in which equation 4.76 was derived. As an example, we obtain an equation for the amplitudes corresponding to singly excited wave functions Ψ_l^c, equation 4.77.

$$\begin{aligned}
\langle \Psi_l^c \mid \hat{H}'_{elec} e^{\hat{\mathbf{T}}} \Psi_0 \rangle &= \langle \Psi_l^c \mid E_{\mathrm{CC}} e^{\hat{\mathbf{T}}} \Psi_0 \rangle \\
\langle \Psi_l^c \mid E_{\mathrm{CC}} \hat{\mathbf{T}}_1 \Psi_0 \rangle &= \langle \Psi_l^c \mid \hat{H}'_{elec} e^{\hat{\mathbf{T}}} \Psi_0 \rangle \\
E_{\mathrm{CC}} \sum_i^{\mathrm{occ}} \sum_a^{\mathrm{vir}} \langle \Psi_l^c \mid t_i^a \Psi_i^a \rangle &= \langle \Psi_l^c \mid \hat{H}'_{elec} e^{\hat{\mathbf{T}}} \Psi_0 \rangle \\
t_l^c E_{\mathrm{CC}} &= \langle \Psi_l^c \mid \hat{H}'_{elec} \left(1 + \hat{\mathbf{T}}_1 + \hat{\mathbf{T}}_2 + \frac{1}{2}\hat{\mathbf{T}}_1^2 + \hat{\mathbf{T}}_3 + \hat{\mathbf{T}}_2\hat{\mathbf{T}}_1 + \frac{1}{6}\hat{\mathbf{T}}_1^3 \right) \Psi_0 \rangle
\end{aligned} \tag{4.77}$$

In the last line of equation 4.77, only the shown terms of the $e^{\hat{\mathbf{T}}}$ expansion would survive, as all others would generate matrix elements involving determinants different by three or more orbitals, which are zeros. The equations for the amplitudes are solved iteratively in conjunction with equation 4.76.

In practical calculations the cluster operator is truncated at some level of excitation. If $\hat{\mathbf{T}}$ includes excitations up to the second level only, $\hat{\mathbf{T}} = \hat{\mathbf{T}}_1 + \hat{\mathbf{T}}_2$, the method is referred to as Coupled Cluster method with Single and Double cluster amplitudes (CCSD). This particular truncation leads to the following form of the exponential operator, equation 4.78 [113].

$$e^{\hat{\mathbf{T}}} = 1 + \hat{\mathbf{T}}_1 + \left(\hat{\mathbf{T}}_2 + \frac{1}{2}\hat{\mathbf{T}}_1^2 \right) + \left(\hat{\mathbf{T}}_2\hat{\mathbf{T}}_1 + \frac{1}{6}\hat{\mathbf{T}}_1^3 \right) + \left(\frac{1}{2}\hat{\mathbf{T}}_2^2 + \frac{1}{2}\hat{\mathbf{T}}_2\hat{\mathbf{T}}_1^2 + \frac{1}{24}\hat{\mathbf{T}}_1^4 \right) + ... \tag{4.78}$$

Substitution of the truncated form of the exponential operator into equations for amplitudes leads to approximate equations, cf. equations 4.77 and 4.79. The energy calculated using a truncated form of the cluster operator is thus also approximate.

$$t_l^c E_{\mathrm{CCSD}} = \langle \Psi_l^c \mid \hat{H}'_{elec} \left(1 + \hat{\mathbf{T}}_1 + \hat{\mathbf{T}}_2 + \frac{1}{2}\hat{\mathbf{T}}_1^2 + \hat{\mathbf{T}}_2\hat{\mathbf{T}}_1 + \frac{1}{6}\hat{\mathbf{T}}_1^3 \right) \Psi_0 \rangle \tag{4.79}$$

4.7 Symmetry-Adapted Perturbation Theory

The Symmetry-Adapted Perturbation Theory (SAPT) [126, 127] is a double perturbation theory in which the MP fluctuation potentials for monomers along with the intermolecular interaction operator act as perturbations. For description of the theory we will utilize widely accepted shorthand notation for the operators being

used. The partitioning of the total Hamiltonian is done as $\hat{H} = \hat{F} + \hat{V} + \hat{W}$, where $\hat{F} = \hat{F}_A + \hat{F}_B$ is the sum of the Fock operators for the monomers A and B, $\hat{V}$ is the intermolecular interaction operator, $\hat{W} = \hat{W}_A + \hat{W}_B$ is the sum of the MP fluctuation operators for the monomers. The unperturbed wave function of a dimer is denoted as $\Phi_{AB}(0) = \Phi_A \Phi_B \equiv \Phi_0$. The unperturbed wave function with proper permutation symmetry is denoted as $\hat{A}\Phi_0$, with $\hat{A}$ being the antisymmetrizer.

The interaction energy in the SAPT is expanded in a double perturbation series, equation 4.80.

$$E_{int} = \sum_{n=1}^{\infty} \sum_{j=0}^{\infty} \left(E_{pol}^{(nj)} + E_{exch}^{(nj)} \right) \tag{4.80}$$

In equation 4.80 the orders in the operators $\hat{V}$ and $\hat{W}$ are denoted by n and j, respectively; $E_{pol}^{(nj)}$ are the polarization energies obtained as regular corrections from the Rayleigh-Schrödinger perturbation theory described in section 4.1.4; $E_{exch}^{(nj)}$ are the exchange corrections arising from the symmetry adaptation.

The most important are interaction energy terms of the zero order in $\hat{W}$ and they will be discussed from here on. One may write the first and the second order polarization energies in the $\hat{V}$, equation 4.81 and 4.82 [126], cf. equation 4.19 and 4.23.

$$E_{pol}^{(10)} = E_{elst}^{(10)} = \langle \Phi_0 \mid \hat{V} \Phi_0 \rangle \tag{4.81}$$

$$E_{pol}^{(20)} = -\sum_{m \neq 0} \frac{|\langle \Phi_0 \mid \hat{V} \Phi_m \rangle|^2}{E_m - E_0} = E_{ind}^{(20)} + E_{disp}^{(20)} \tag{4.82}$$

The meaning of the first order polarization energy is the energy of the electrostatic interaction of the monomers charge distributions, $E_{elst}^{(10)}$. The induction and dispersion energies could be obtained from the second order polarization energy. If the sum in equation 4.82 is limited to singly excited molecular functions of the form $\Phi_m = \Phi_A \Phi_B^{exc}$ and $\Phi_m = \Phi_A^{exc} \Phi_B$, where the superscript exc stands for an excited state, one obtains the induction energy. It thus follows that the second order induction energy $E_{ind}^{(20)}$ results from polarization of monomers by a static electric field of unperturbed partner. When summation in equation 4.82 is performed including doubly excited molecular states $\Phi_m = \Phi_A^{exc} \Phi_B^{exc}$ then the second order dispersion energy results. This term could be also defined as $E_{disp}^{(20)} = E_{pol}^{(20)} - E_{ind}^{(20)}$. The dispersion thus represents intermolecular correlations of instantaneous multipole moments of the monomers.

The first order interaction energy obtained with antisymmetrized wave function is given by equation 4.83 [126].

$$E_{int}^{(10)} = \frac{\langle \Phi_0 \mid \hat{V}\hat{A}\Phi_0 \rangle}{\langle \Phi_0 \mid \hat{A}\Phi_0 \rangle} \tag{4.83}$$

Having the interaction energy obtained with antisymmetric wave function, equation 4.83, exchange contribution to the energy could be calculated according to equation 4.80 as $E_{exch}^{(10)} = E_{int}^{(10)} - E_{pol}^{(10)}$, in the first order in $\hat{V}$ and analogously in higher orders. In second order in $\hat{V}$, the exchange energy is naturally divided into exchange-induction $E_{exch-ind}^{(20)}$ and exchange-dispersion $E_{exch-disp}^{(20)}$ energies, equation 4.84.

$$E_{exch}^{(20)} = E_{exch-ind}^{(20)} + E_{exch-disp}^{(20)} \tag{4.84}$$

In the SAPT estimation of high order induction and exchange-induction terms one frequently uses the supermolecular Hartree-Fock interaction energy, E_{int}^{HF}. A term $\triangle$HF is defined according to equation 4.85, where SAPT correction terms of the zero order in $\hat{W}$ are involved.

$$E_{int}^{\mathrm{HF}} = E_{elst}^{(10)} + E_{exch}^{(10)} + E_{ind}^{(20)} + E_{exch-ind}^{(20)} + \triangle\mathrm{HF} \tag{4.85}$$

If the $\triangle$HF term is included into the SAPT interaction energy it is called a hybrid SAPT approach. This was shown to be more accurate if one or both monomers are polar. However, for dispersion bound dimers, if third order SAPT corrections are calculated, it is advantageous to replace the $\triangle$HF term by the sum $E_{ind}^{(30)} + E_{exch-ind}^{(30)}$ [127].

4.8 Order-N Methods

The fact that electronic properties are to a large extent dependent on the nearest neighborhood was used by Walter Kohn to introduce a principle of "nearsightedness", which justifies a possibility of electronic structure methods that scale linearly with the number of atoms [128]. The principle is a manifestation of wave-mechanical destructive interference and is valid when large numbers of particles are present. For many particles at equilibrium moving in an external potential $u(r)$ without long range electric fields the principle is expressed as follows, after W. Kohn: "Let $F(r_1, r_2, ..., r_\nu)$ be a static property depending on ν coordinates $r_1, ..., r_\nu$, all within a restricted volume w of linear dimension $\sim \lambda$, a typical de Broglie wavelength occuring in the ground state wave function or finite T ensemble. [The density $n(r)$ and pair-correlation function $g(r, r')$ are examples.] Denote by $\overline{r}$ the center of mass, $\overline{r} \equiv \nu^{-1} \sum_1^\nu r_\mu$. Then, at fixed chemical potential μ, a change of the external potential $\Delta u(r')$, no matter how large, has a small effect on F, provided only that $\Delta u(r')$ is limited to a distant region, in the sense that for all r', $|r' - \overline{r}| \gg \lambda$. Thus F does not "see" $\Delta u(r')$ if r' is far."

The possibility of order-N methods follows from the nearsightedness. Suppose we divide a system of volume Ω into a number of subsystems of overlapping smaller volumes $\omega = (m\lambda)^3$ with m being about 100. The number of these small volumes is $\Omega/\omega \sim$ N. Because of the nearsightedness, a property F can now be calculated independently for each volume ω with a computational effort for the whole system scaling linearly with N, most likely with a large prefactor. W. Kohn regarded this case as an existence theorem for the possibility of order-N methods.

In this work we use the Spanish Initiative for Electronic Simulations with Thousands of Atoms (SIESTA) method for some calculations [129]. The order-N scaling of this approach results mainly from two features: confined Wannier-like electronic wave functions and the usage of an energy functional the minimization of which proceeds without the need to orthonormalize electronic states. Instead, correct orthonormal orbitals are produced as a result of the minimization. Our interest was limited to the first feature. According to W. Kohn, order-N methods can be divided into two categories: one-particle density matrix methods, where one neglects matrix elements beyond given distance, or Wannier function methods where orbitals are strictly zero beyond a certain radius. The SIESTA method thus falls into the second category. The approach has an advantage over the one-particle density matrix methods as it maintains the variational character of the total energy.

We illustrate how the confinement of orbitals is achieved in the SIESTA method in the case of a minimal basis set [130]. The basis functions are represented as the numerical angular momentum dependent eigenfunctions of atomic pseudopotentials. The energies of these functions are chosen in such a way that the first node coincides with the desired cutoff radius. Beyond this radius the basis functions are zero.

4.9 Conclusions

A variety of theoretical methods is available for simulation of materials. A reasonable compromise between accuracy and efficiency is achievable with the DFT, which is the method of choice in this work. In situations where DFT is known to fail, like weak intermolecular interactions, dispersion corrections could be introduced within the framework of the DFT-D or MP theory. High level theoretical methods, CC and perturbation theory, could be used to discriminate applicability of the DFT, DFT-D, and MP approaches. The SAPT could justify the method to be used in certain cases by determining the relative contributions from electrostatic, exchange, induction and dispersion components of the intermolecular interaction energy. For quick and preliminary studies of very large systems order-N methods could be applied. The performance of different methods for AB-H_2 systems is evaluated in the next chapter.

Chapter 5

Concept of Hierarchical Hydrogen Storage

5.1 Hierarchical Storage of Hydrogen

As chapter 2 has concluded, to overcome difficulties related to storage of hydrogen, weak and strong forces binding it in a material should be combined. From chapter 3 it follows that this combination could be found in hydrogen clathrates. However, clathrates with host molecules suitable for on-board hydrogen storage and release are unknown. To summarize our idea, we will formulate a concept of hierarchical hydrogen storage, which would be further implemented using a certain type of host molecules.

The concept of hierarchical hydrogen storage is represented in figure 5.1 and is based on hydrogen clathrates build of a Chemical Hydrogen Storage Medium (CHSM). The CHSM plays a role of host molecules of the hydrogen clathartes. It might be any chemical hydrogen storage material involving complementary Proton Donor (PD) and Proton Acceptor (PA) sites and therefore capable to form supramolecular hydrogen bonded networks. It is envisaged that kinetically easily

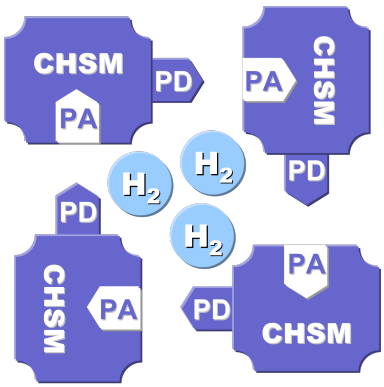

Hydrogen clathartes built of CHSM – Chemical Hydrogen Storage Medium; PD – Proton Donor; PA – Proton Acceptor.

Figure 5.1: Concept of hierarchical hydrogen storage.

accessible molecular hydrogen would fill in cages of the clathrate, further increasing the density of stored hydrogen.

The concept offers two layers of stored hydrogen. The first layer is the physisorbed hydrogen, which acts as guest molecules or clusters thereof. The second layer is the hydrogen chemically bound in the CHSM. A difference in rates of release of physisorbed and chemically bound hydrogen gives rise to the storage hierarchy. We expect hydrogen to be released in two stages: a fast release of guest hydrogen molecules and a slower release of hydrogen bound in the CHSM.

A potential CHSM should satisfy two requirements. Firstly, it should be a satisfactory hydrogen storage material, i.e., it should provide a significant density of recoverable hydrogen. Second, it should be able to form hydrogen or dihydrogen bonded networks via intrinsic PD and PA sites, in order to organize itself into porous clathrate-like structures. A reasonable choice of CHSM could be AB as it satisfies both formulated requirements. It has complementary PD and PA sites and it can form dihydrogen bonded networks, as it does in its molecular crystal incarnation. With 19.6 wt% of hydrogen it is recognized as one of the most promising hydrogen storage materials [15, 14].

5.2 Ammonia Borane as a Host Molecule

The strength of host-host and host-guest interactions is critical for clathrates stability. Intrinsic polarity of host molecules is a necessary requirement to be fulfilled in order to provide strong intermolecular interactions dominated by the electrostatic and induction terms. The significant polarity of an AB molecule results from very different electronegativities of boron and nitrogen. The molecule is characterized by a significant dipole moment of 5.216 D [15], with positively and negatively charged ends being on nitrogen and boron sides, respectively. Protic and hydridic hydrogens are bound to nitrogen and boron, respectively, in accordance with the charge distribution, figure 5.2(a). A large dipole moment is advantageous for any host component as it reflects an ability to polarize electronic clouds of neighbouring host and guest molecules, and thus an ability to be involved into permanent dipole – induced dipole (host-guest) and permanent dipole – permanent dipole (host-host) interactions. The polarity of AB is the main reason for the stability of its molecular crystal at ambient pressure and temperature. AB molecules in a crystalline phase form a network of non-covalent interactions – dihydrogen bonds, figure 5.2(b), with hydridic H(B) hydrogens acting as acceptors of protic H(N) hydrogens [131]. In the orthorhombic phase of AB each proton is involved into two dihydrogen bonds.

Apart from these qualitative arguments, it is sensible to make a quantitative comparison of intermolecular interactions occurring in the existing in nature water clathrates of hydrogen with analogous interactions in possible clathrates of AB.

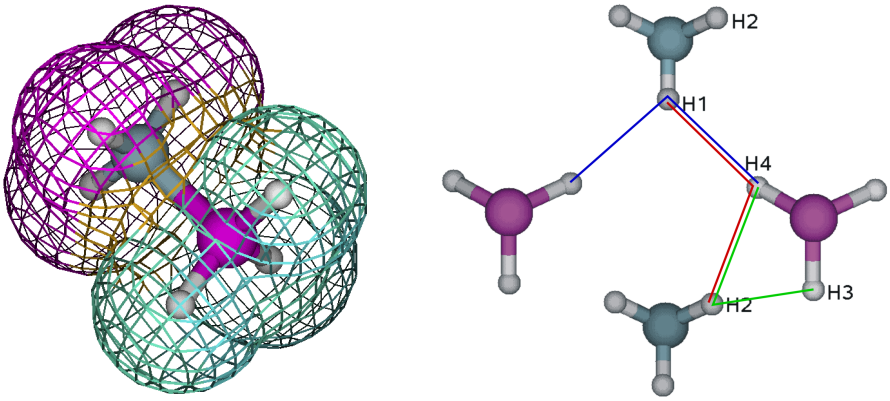

(a) Map of electrostatic potential of AB molecule (key for map – magenta: "+", aquamarine: "−"; key for molecule – aquamarine: nitrogen, magenta: boron, white: hydrogen).

(b) Dihydrogen bonded network in orthorhombic AB, view along N-B bond with NH_3 units looking up and BH_3 units looking down (dihydrogen bonds of H1: blue; H2: green; H4: red).

Figure 5.2: Polarity of AB molecule (a) and dihydrogen bonded network in orthorhombic AB (b).

There are two important types of intermolecular interactions in clathrates: host-host and host-guest. For simplicity, we consider optimized molecular configurations of binary complexes [132, 133]. As follows from figure 5.3, AB is involved in stronger interactions than water. For the host-guest case, figure 5.3(a), 5.3(b), 5.3(d), the interactions are two times stronger and for the host-host case, figure 5.3(c), 5.3(e), the interactions are more than three times stronger.

5.3 Weak Interactions in NH_3BH_3-H_2 and NH_3BH_3-NH_3BH_3 Systems

The promising conclusions of section 5.2 inspired an in-depth study of weak intermolecular interactions in the AB-H_2 and AB-AB systems within the framework of SAPT. This study serves three purposes. The first is to gain understanding of physical nature of these interactions, the second is to select and justify theoretical methods to be used in the design of AB clathrates, and the third is to apply the obtained *ab-initio* intermolecular potentials in the construction of spherically symmetric potentials of the interior of AB clathrate cages.

Molecular configurations considered in this study are shown in figures 5.4, 5.5, and 5.6. There are four configurations for the AB dimer, and three configurations for the AB-H_2 system and the H_2 dimer. The distance between molecules (separation) is defined here as follows. For the AB dimer the distance is measured between middle points of segments connecting boron and nitrogen atoms in each AB molecule. For the AB-H_2 system the distance is measured between the middle point of a segment, which connects boron and nitrogen in AB and the middle point of a segment, which

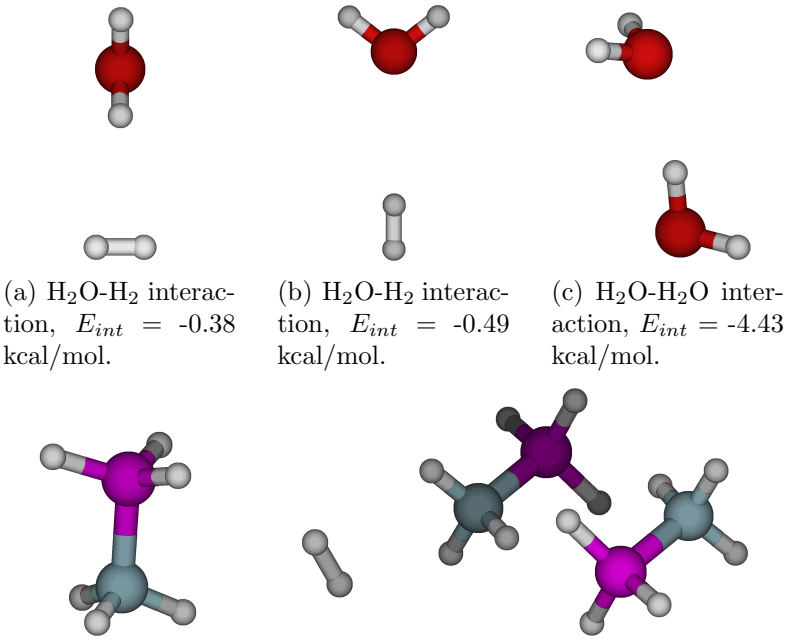

(a) H_2O-H_2 interaction, E_{int} = -0.38 kcal/mol.

(b) H_2O-H_2 interaction, E_{int} = -0.49 kcal/mol.

(c) H_2O-H_2O interaction, E_{int} = -4.43 kcal/mol.

(d) NH_3BH_3-H_2 interaction, E_{int} = -0.98 kcal/mol.

(e) NH_3BH_3-NH_3BH_3 interaction, E_{int} = -14.14 kcal/mol.

Interaction energies E_{int} calculated at MP2/aug-cc-pVDZ level of theory and corrected for BSSE.

Figure 5.3: Host-guest and host-host interactions in water and AB systems.

connects two hydrogen atoms in H_2. For the H_2 dimer the distance is measured between middle points of segments, which connect two hydrogen atoms in each H_2. For MP2 calculations, each monomer was initially optimized at the MP2/aug-cc-pVTZ level of theory. For the DFT, Coupled Cluster method with Single, Double and non-iterative Triple cluster amplitudes (CCSD(T)), and SAPT calculations, each monomer was initially optimized at the CCSD(T)/aug-cc-pVTZ level of theory.

For the AB dimer, the second order SAPT corrections were calculated along with the HF correction term ($\triangle$HF), the so-called hybrid SAPT approach. For the AB-H_2 and H_2 dimers, corrections up to the third order in perturbation were calculated. The AB-H_2 system was treated within the hybrid approach and the H_2 dimer was treated within the pure SAPT approach [127]. The basis-set used for SAPT calculations was 6-311++G** with a mid-bond 3322 (3s3p2d2f) set placed at the center of the separation, the so-called dimer-centered basis set (DC+BS) approach. The addition of the bond functions yields better description of the dispersion energy [134, 135]. The calculations were done using the SAPT2006 package with the Atmol code as a front-end SCF program.

A decomposition of interaction energy into physically meaningful contributions is shown in figure 5.7 for the AB dimer, and in figure 5.8 for the AB-H_2 system and the H_2 dimer. A comparison of the MP2 intermolecular potentials with the SAPT and CCSD(T) potentials for the AB dimer is presented in figure 5.9. A comparison of the DFT intermolecular potentials with the MP2 and CCSD(T) potentials is depicted in figure 5.10. A comparison of the MP2 intermolecular potentials with the SAPT

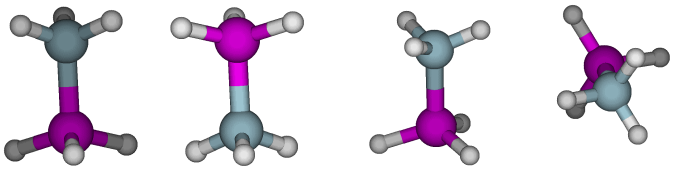

(a) Configuration A. (b) Configuration B.

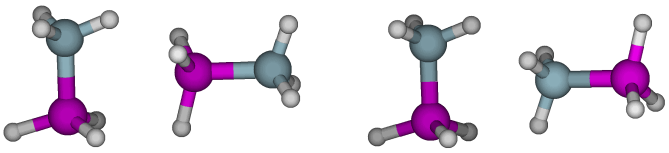

(c) Configuration C. (d) Configuration D.

Figure 5.4: Studied molecular configurations of AB dimer.

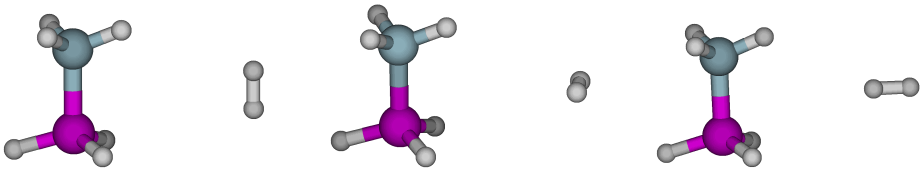

(a) Configuration A. (b) Configuration B. (c) Configuration C.

Figure 5.5: Studied molecular configurations of AB-H_2 system.

and CCSD(T) potentials for the AB-H_2 system and the H_2 dimer is presented in figure 5.11.

As figure 5.7 demonstrates for the A configuration of AB_2, the dominant part of attractive interaction energy, more than 30% at equilibrium geometry, results from the electrostatic component, table 5.3. For other configurations the dispersion becomes the dominant part, about 30% of the interaction energy, with non negligible contributions from the electrostatic and induction components, table 5.3. Agreement between the SAPT intermolecular potentials and potentials obtained at the MP2 level of theory is at least fairly good and sometimes excellent, figure 5.9. However, more important is the performance of DFT. The electrostatic and induction terms are dominant for the most important configuration A and relevant for all other configurations. Thus the DFT potentials might be physically meaningful. There are two $NH_3^{\delta+}...^{\delta-}H_3B$ motifs in configuration A, which could be met in crystal structures of AB, figure 5.2(b), and later on in clathrates of AB. If energetics of this configuration is well reproduced the involved functional can be used in further studies of extended AB systems. Fortunately, all DFT functionals perform well for this configuration when compared with the MP2 and the

(a) Configuration A. (b) Configuration B. (c) Configuration C.

Figure 5.6: Studied molecular configurations of H_2 dimer.

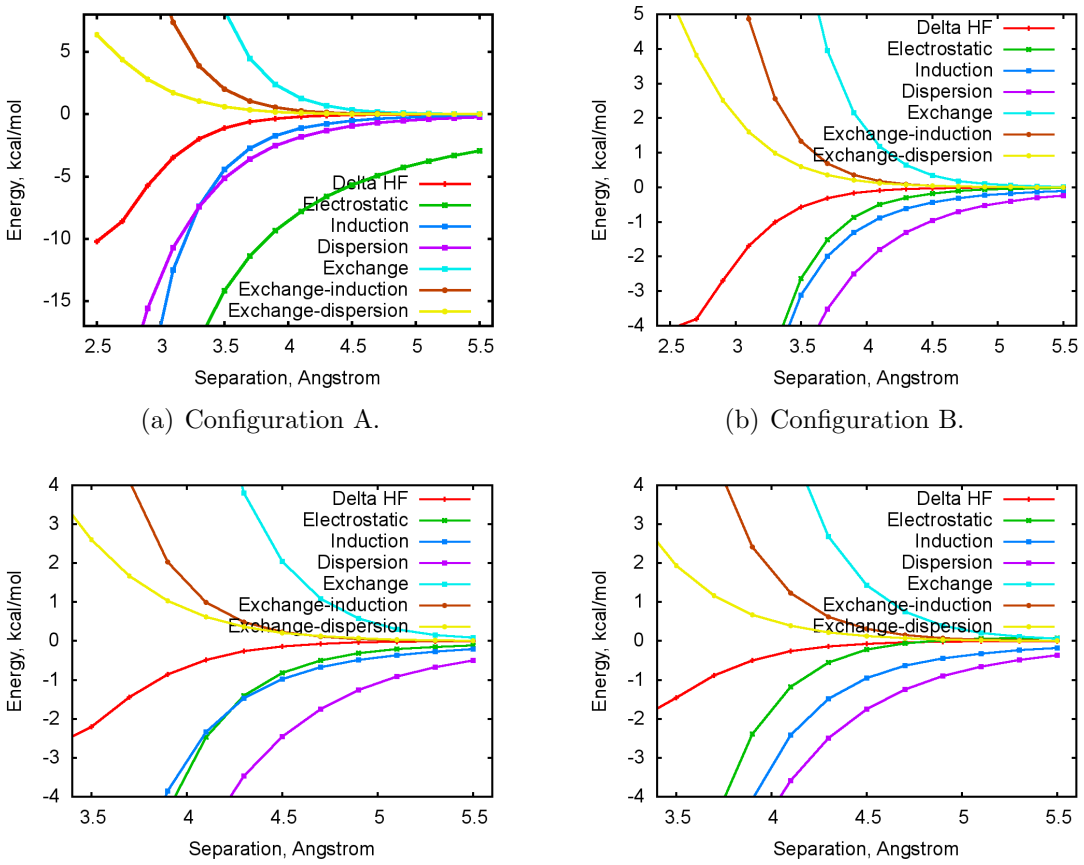

(a) Configuration A.

(b) Configuration B.

(c) Configuration C.

(d) Configuration D.

Figure 5.7: Decomposition of interaction energy for AB dimer.

Configuration	R_{eqlb}, Å	E_{eqlb}, kcal/mol	The most important relative contributions to the interaction energy, %			
			Electrostatic	Induction	Dispersion	Exchange
A	3.3	-14.59	32.84	13.33	13.41	27.91
B	3.7	-2.34	12.26	16.17	28.56	32.02
C	4.3	-1.97	12.51	13.10	30.81	33.77
D	4.3	-1.14	6.68	18.16	30.48	32.80

Table 5.1: Equilibrium geometry parameters for AB dimer, the SAPT data.

Configuration	R_{eqlb}, Å	E_{eqlb}, kcal/mol	The most important relative contributions to the interaction energy, %			
			Electrostatic	Induction	Dispersion	Exchange
A	3.3	-0.50	7.26	14.07	32.66	32.82
B	3.3	-0.59	12.36	11.66	31.62	31.66
C	3.5	-0.42	4.65	12.84	37.41	31.74

Table 5.2: Equilibrium geometry parameters for AB-H_2 system, the SAPT data.

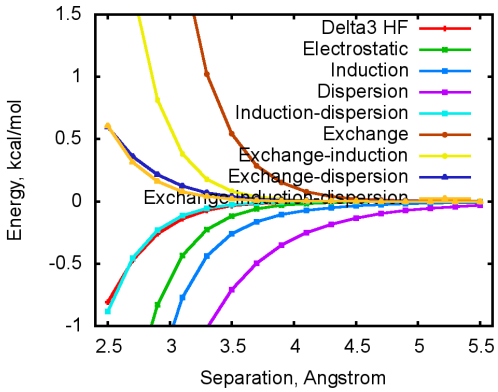

(a) AB-H_2 system, configuration A.

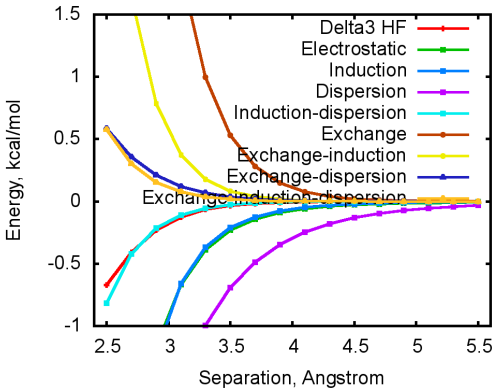

(b) AB-H_2 system, configuration B.

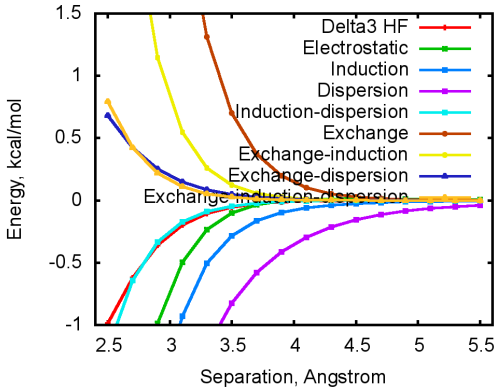

(c) AB-H_2 system, configuration C.

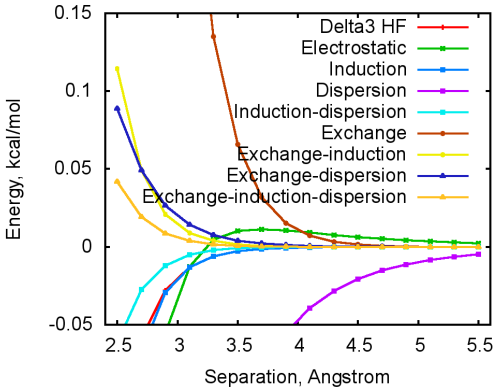

(d) H_2 dimer, configuration A.

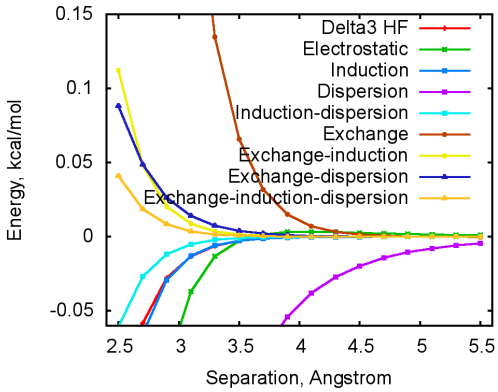

(e) H_2 dimer, configuration B.

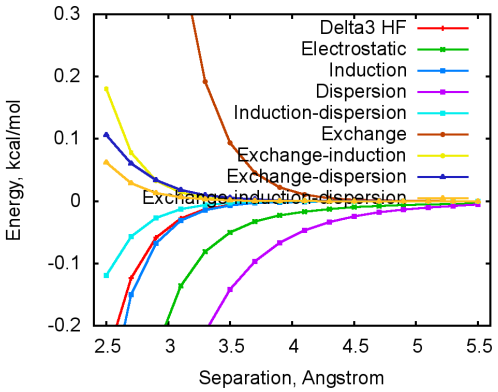

(f) H_2 dimer, configuration C.

Figure 5.8: Decomposition of interaction energy for AB-H_2 system and H_2 dimer.

Configuration	R_{eqlb}, Å	E_{eqlb}, kcal/mol	The most important relative contributions to the interaction energy, %			
			Electrostatic	Induction	Dispersion	Exchange
A	3.5	-0.04	5.16	1.36	57.07	32.81
B	3.5	-0.05	1.38	1.41	59.07	34.48
C	3.3	-0.10	15.52	2.72	40.28	36.82

Table 5.3: Equilibrium geometry parameters for H_2 dimer, the SAPT data.

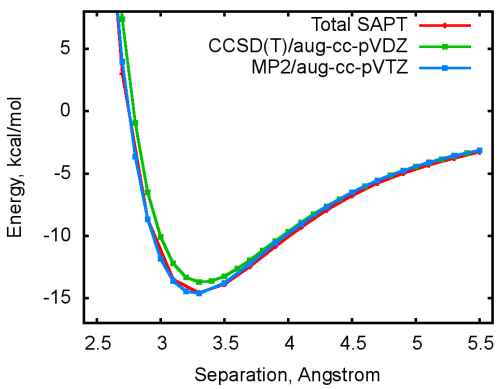

(a) Configuration A.

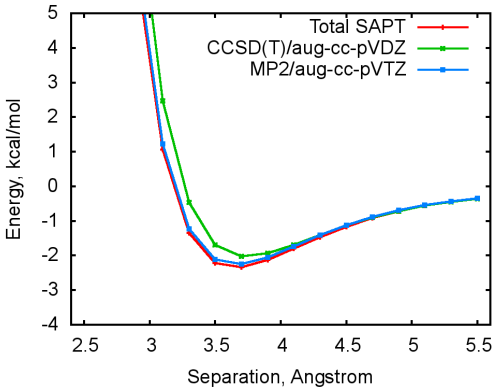

(b) Configuration B.

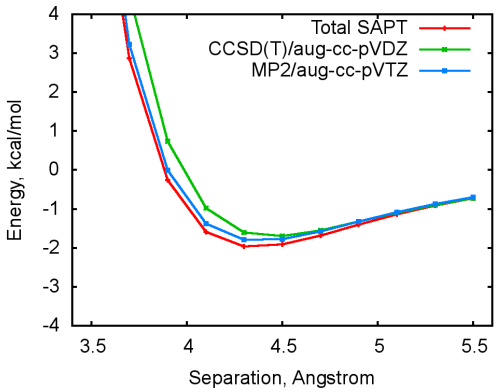

(c) Configuration C.

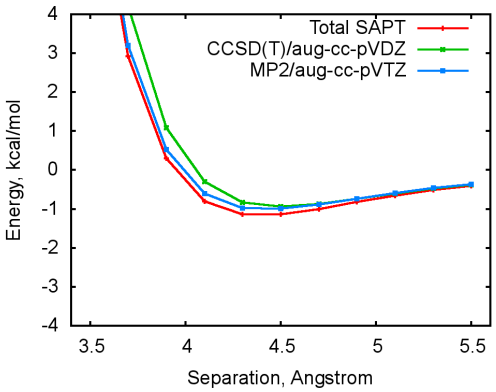

(d) Configuration D.

Figure 5.9: Performance of MP2 against the SAPT and the CCSD(T) methods for AB dimer interactions.

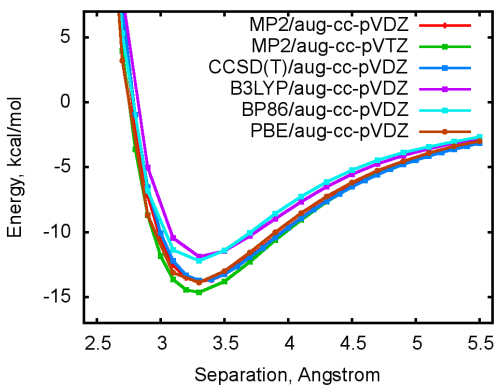

(a) Configuration A.

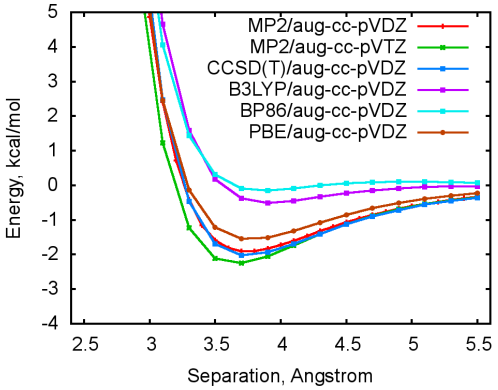

(b) Configuration B.

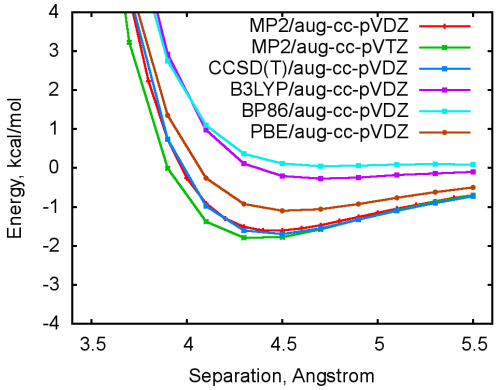

(c) Configuration C.

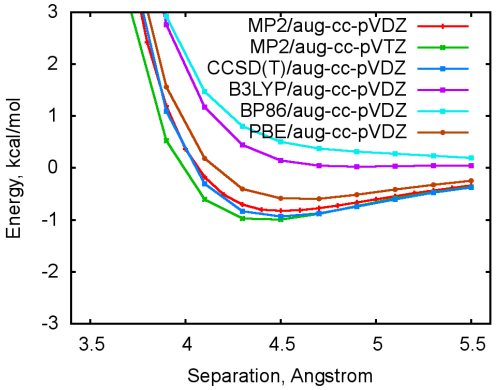

(d) Configuration D.

Figure 5.10: Performance of DFT against the MP2 and the CCSD(T) methods for AB dimer interactions.

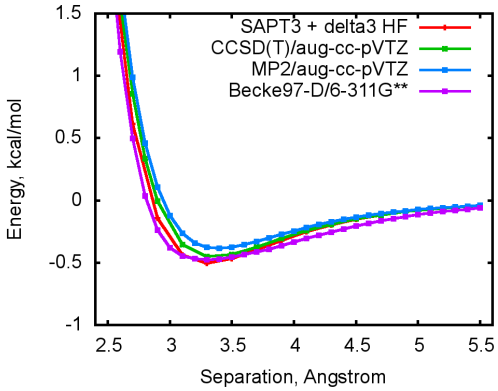

(a) AB-H_2 system, configuration A.

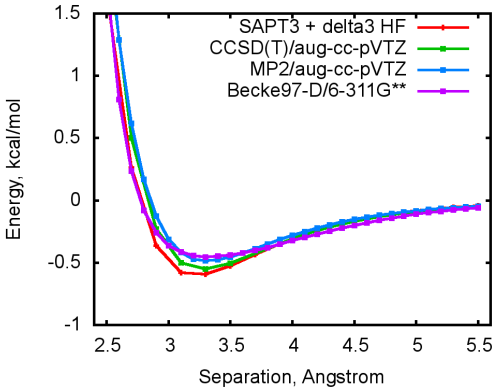

(b) AB-H_2 system, configuration B.

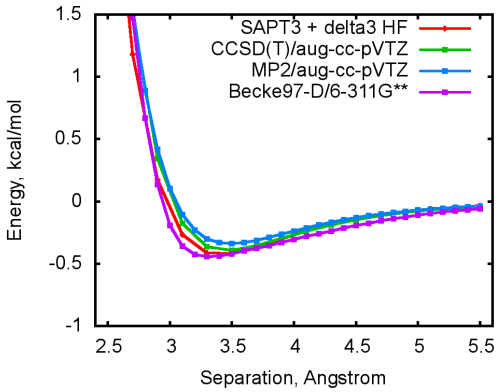

(c) AB-H_2 system, configuration C.

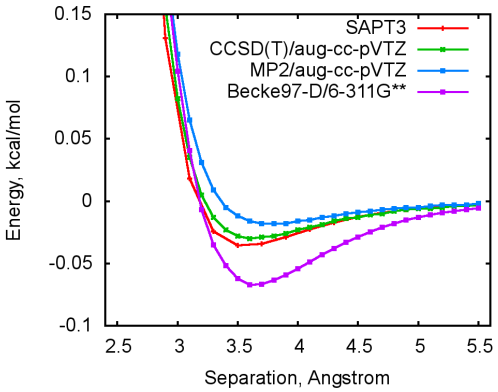

(d) H_2 dimer, configuration A.

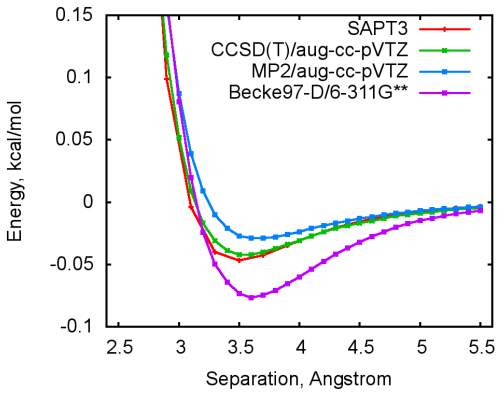

(e) H_2 dimer, configuration B.

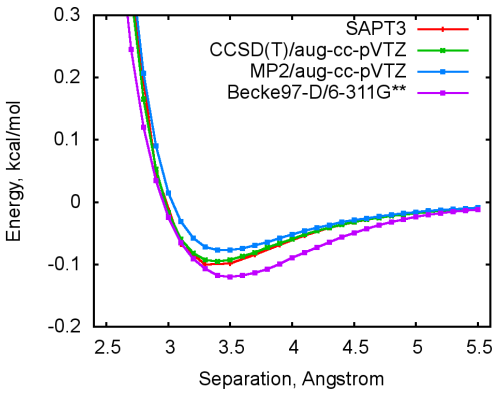

(f) H_2 dimer, configuration C.

Figure 5.11: Performance of MP2 and DFT-D against the SAPT and the CCSD(T) methods for AB-H_2 and H_2 dimer interactions.

CCSD(T) methods, figure 5.10(a), with relative errors less than 15% for the equilibrium geometry. This means that any DFT functional tested here (Becke 3-parameter exchange, Lee, Yang and Parr correlation (B3LYP) [136, 137, 138, 139]; Becke exchange, Perdew 1986 correlation (BP86) [140, 141]; and Perdew-Burke-Ernzerhof exchange and correlation (PBE) [142]) could be applied to study empty cages and frameworks of AB clathrates, with a preference given to the PBE functional. Even for configurations dominated by the dispersion interaction (configurations B, C, and D), the performance of PBE is satisfactory in comparision with the MP2 and CCSD(T) methods, figure 5.10. It is possible to distinguish pronounced minima in intermolecular potential curves produced with the PBE functional. The results obtained with other functionals are less accurate.

As is shown in figures 5.8(a)-5.8(c), the dominant part of attractive interaction energy for the AB-H_2 system results from the dispersion, more than 30% at equilibrium geometries for all considered configurations, table 5.3. The relative contributions from electrostatic and induction components are still important, although smaller than in case of the AB dimer. With intermolecular interaction energies about half a kcal/mol and large contributions from the dispersion term, table 5.3, only correlated methods could provide accurate results for the AB-H_2 system. The MP2 intermolecular potential is in good agreement with the CCSD(T) potential, with the largest relative error at equilibrium geometries less than 15%, figures 5.11(a)-5.11(c). The results suggest using the MP2 method for estimation of hydrogen capacity of various cages of AB clathrates.

The intermolecular forces for H_2 dimer are strongly dominated by dispersion, figures 5.8(d)-5.8(f), which contributes from 40% to almost 60% to the interaction energy at equilibrium geometries of all considered configurations, table 5.3. The electrostatic and induction components are practically negligible for all but one configuration, C. The interaction energy is never larger than 0.1 kcal/mol and even the MP2 intermolecular potentials deviate from higher level potentials, figures 5.11(d)-5.11(f). This deficiency of MP2 is reflected in a decrease of the interaction energy and in an increase of the equilibrium intermolecular separation in comparison with the CCSD(T) potential curves. Such a behavior is favorable for further studies with more than one hydrogen molecule enclosed in a cage of AB clathrates, as it would lead to underestimation rather than overestimation of the maximum number of entrapped guest molecules, and thus, provide a lower limit to the hydrogen density.

The size of clathrate systems requires using faster computational methods than MP2. The dispersion interaction energy could be recovered with the DFT-D method. Due to empirical nature of the dispersion correction in this method some tests have been performed for the AB-H_2 system and the H_2 dimer. It is seen from figures 5.11(a)-5.11(c) that the host-guest interactions are described very accurately. How-

ever, the guest-guest interactions, figures 5.11(d)-5.11(f), are reproduced less reliably. The minima of interaction potentials are shifted to the right, which gives a lower limit to the number of entrapped hydrogen molecules in one cage. In addition, the H_2-H_2 interaction energies are overestimated, which is interesting from the methodological perspective, but practically plays a very minor role, because the guest-guest interactions are one order of magnitude weaker than the host-guest interactions.

5.4 Conclusions

The concept of hierarchical hydrogen storage provides grounds for a desirable combination of weak and strong forces, which would bind hydrogen in one material. The concept could be realized by hydrogen clathrates of AB. A theoretical design and study of this material could be done applying certain methods, which were shown to be suitable. The DFT could be used to design empty cages and frameworks of the clathrates whereas the DFT-D, and MP2 methods should be used to estimate their hydrogen capacity. For AB dimer in geometry close to the global minimum or in other geometries, where interactions between AB molecules are dominated by the electrostatic component due to the presence of $NH_3^{\delta+}...^{\delta-}H_3B$ motifs, the DFT is applicable and may be used to design cages and frameworks of AB clathrates. At the same time the DFT could not be used to make conclusions about the magnitude of host-guest interactions due to its inability to reproduce the dispersion component of intermolecular forces. The lowest level *ab-initio* approach which recovers dispersion and could be used to estimate hydrogen occupancy of cages of AB clathrates is the MP2 method, although for large cages the DFT-D could be used instead.

Chapter 6

Cages of Ammonia Borane Clathrates

6.1 Construction Principles and Molecular Arrangements

Cages, which are formed by host molecules in clathrate structures, are thought of as building blocks of extended systems. These cages typically do not exist in nature as independent entities, but they are the simplest units of clathrate materials, which maintain their identity and compose periodic structures. From the theoretical point of view, cages are convenient targets. They are relatively small and could be studied with advanced theoretical methods, as clusters in the gas phase. When designing clathrates of AB it is reasonable to start from the cages, before one faces the challenge of 3D structures.

Common sense and available knowledge say that known clathrate cages are three dimensional convex polyhedrons, and we will make the same assumption about the cages of AB. Another appeal to common sense and analysis of the properties of an AB molecule (polarity, somewhat linear geometry) and a connectivity pattern in the molecular crystal of AB dictate that in order to form a stable spatial aggregate (a cage) the AB molecules should be oriented in such a way that the nitrogen end of one molecule is located somehow opposite to the boron end of another molecule. This allows avoiding repulsions of the B-H...H-B and N-H...H-N types and favors attractions of the B-H...H-N type (dihydrogen bonds).

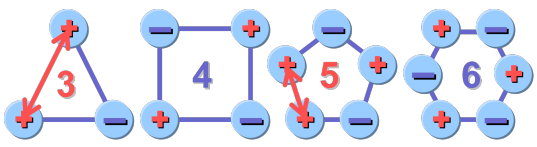

Red arrows indicate repulsion of like charges.

Figure 6.1: Structural stability of polygons.

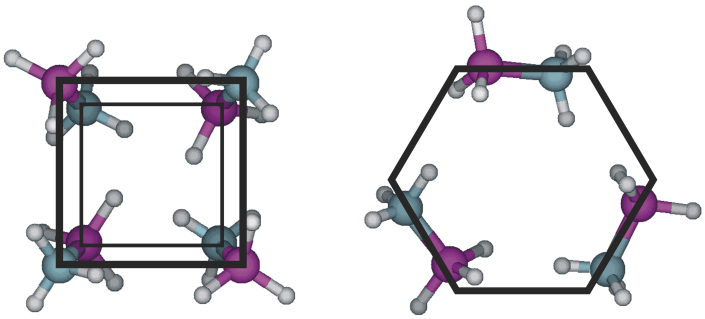

(a) Face perpendicular arrangement.

(b) Arrangement along face edges.

Figure 6.2: Possible arrangements of molecules in cages of AB clathrates.

In order to further formalize the task of construction of cages, we first invoke an analogy with ice and hydrates. The orientation of water molecules in hydrates and in different phases of ice obeys simple rules, which are known as ice rules or the Bernal-Fowler rules [79, 80]. According to these rules, water molecules in ice are arranged in such a way that each is surrounded by four others and it directs its two hydrogen atoms towards two of the four neighbours, i.e., it acts as a double proton donor. At the same time it acts as a proton acceptor when interacting with two other neighbouring water molecules (a double proton acceptor). "The orientations are further restricted by the requirement that only one hydrogen atom lies near each O-O axis", L. Pauling writes [80]. One might come up with analogous requirements for the crystal structure of AB, see figure 5.2(b).

We postulate that for hypothetical structures of AB clathrates to be similarly stable as the AB molecular crystal each proton should be engaged in two dihydrogen bonds. In addition, high polarity of an AB molecule, its intramolecular charge distribution, and its linear geometry enforce a constraint on the shape of possible cages. Each face (or polygon) of the cage (or polyhedron) must satisfy a structural stability criterion. Only when every single face of a polyhedron has an even number of vertices, the structural stability of alternating charges is guaranteed and contacts of likely charges (frustrations) are avoided, figure 6.1. As a culmination of these structural requirements, or construction principles, we are now able to arrange AB molecules on two-dimensional faces in physically meaningful ways, figure 6.2. A face perpendicular arrangement and an arrangement along face edges would not violate the structural stability for faces having an even number of vertices.

Before we consider three dimensional structures satisfying the construction principles, it should be mentioned that the rule of structural stability of polygons is critical. Its violation leads to structures, which are not local minima on potential energy surfaces. The second rule, that each protic hydrogen should be engaged in two dihydrogen bonds, is less strict. Its relaxation results in structures with less favourable networks of dihydrogen bonds, but this deficiency could be compensated by the strain-free nature of resulting structures or by favourable guest-host interac-

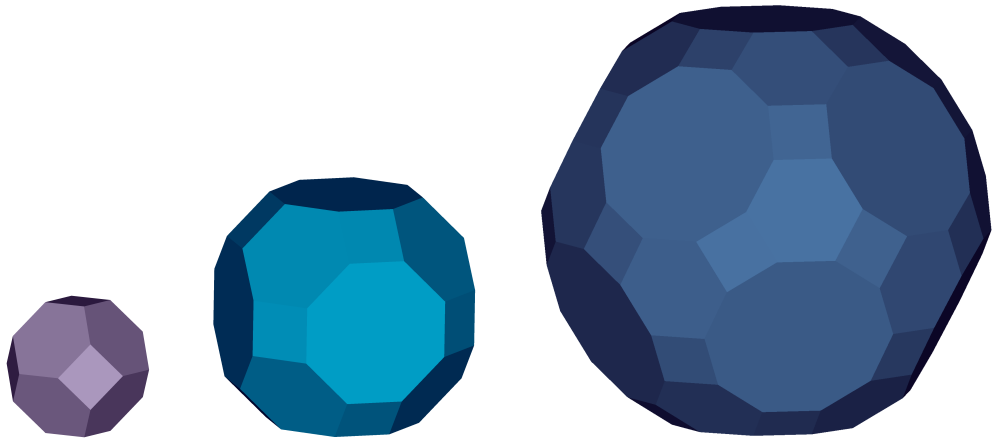

(a) Truncated octahedron. (b) Great rhombicuboctahedron. (c) Great rhombicosidodecahedron.

Figure 6.3: Polyhedrons satisfying structural stability.

Name	Configuration of vertex†	Specification	Faces	Edges	Vertices
Truncated octahedron	4, 6, 6	$4^6 6^8$	14 including 6 tetragonal, 8 hexagonal	36	24
Truncated cuboctahedron or great rhombicuboctahedron	4, 6, 8	$4^{12} 6^8 8^6$	26 including 12 tetragonal, 8 hexagonal, 6 octagonal	72	48
Truncated icosidodecahedron or great rhombicosidodecahedron	4, 6, 10	$4^{30} 6^{20} 10^{12}$	62 including 30 tetragonal, 20 hexagonal, 12 decagonal	180	120

†Number of edges of faces meeting at the vertex, the same for each vertex in uniform polyhedron; For further details on these polyhedrons see [143].

Table 6.1: Characteristics of polyhedrons complying with structural stability.

tions.

6.2 Three Types of Cages

In an attempt to generalize the construction principles to three dimensional case, we already mentioned that all faces of a cage of interest must have an even number of vertices in order to comply with the construction rule. There are several structures satisfying this requirement, which are Archimedean solids [143], namely a truncated octahedron, a truncated cuboctahedron or great rhombicuboctahedron, and a truncated icosidodecahedron or great rhombicosidodecahedron, figure 6.3 and table 6.2.

We now choose the smallest polyhedron to check which molecular arrangement is favorable. The arrangement of AB molecules along edges resulted in a stable structure without vibrational modes with imaginary frequencies. On the other hand, the perpendicular arrangement proved to be unstable. Our interpretation of these

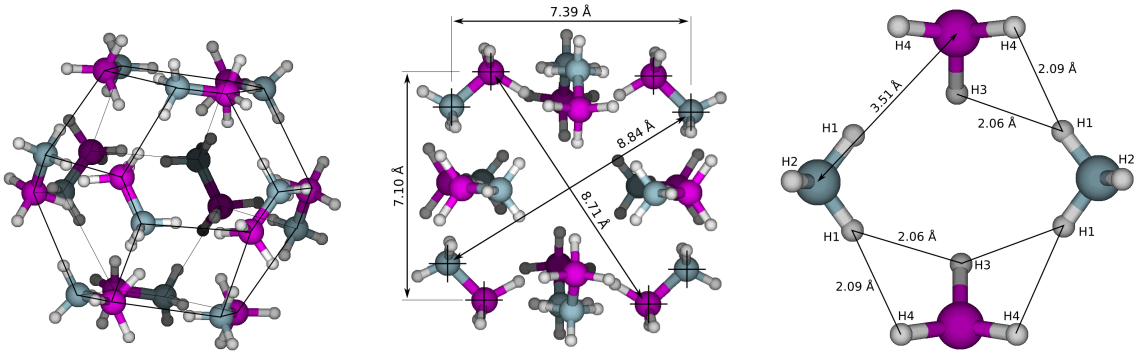

(a) Overview of Cage 12. (b) Dimensionality of Cage 12. (c) Network of dihydrogen bonds in Cage 12 (cf. figure 5.2(b)).

Figure 6.4: Geometry of Cage 12 and its network of dihydrogen bonds.

findings is the following. If a molecule is perpendicular to one face then it is not perpendicular to two other faces converging in the same vertex. This leads to strained dihydrogen bonds and reduces stability of a cage constructed in such a way. An arrangement along edges of faces offers equal footing for all participating molecules and could result in less strained dihydrogen bonds, if strained at all.

Two possible arrangements of AB molecules were rigorously tested at the B3LYP/6-311G** level of theory as implemented in the Gaussian 03 package [144]. Over the course of geometry optimization, the perpendicular arrangement resulted in opening up the cage and further developing a nearly planar structure of AB molecules, similar to a fragment in figure 6.2(a). The outcome of geometry optimization was the same with another initial structure, in which the AB molecules were not placed perpendicular to faces but rather along lines coming through the cage center and each vertex, to compensate for strain of dihydrogen bonds. On the other hand, an initial structure based on the arrangement along edges converged smoothly to a stable structure connected through dihydrogen bonds.

The identified AB clathrate cage, figure 6.4 and table 6.2[1], has a characteristic pattern of non covalent interactions, figure 6.4(c), similar to the one which exists in the dihydrogen bonded network of the AB molecular crystal, figure 5.2(b). The pattern is repeated six times on its tetragonal faces. Noticeable geometrical differences between an AB molecule bound within the cage and a free AB molecule, table 6.2, are: an elongation of the N-H and B-H bonds, a contraction of the B-N bond, and an opening up of the B-N-H and N-B-H angles.

The Basis Set Superposition Error (BSSE) corrected binding energy of an AB molecule in the cage was calculated using several functionals with the 6-311G** basis set and was found to be 11.59, 11.82, and 13.93 kcal/mol with the B3LYP, BP86, and PBE functionals, respectively. The Gaussian 03 package [144] has been used for the calculations. The energy is fairly insensitive to the functional used and is

[1]In figure 6.4 and table 6.2 we used a designation Cage 12 which stands for a AB clathrate cage containing twelve AB molecules. For larger cages a similar notation is going to be used further on.

Parameter*	Molecular NH_3BH_3		Parameter*	Molecular NH_3BH_3	
	Cage geometry	Gas phase geometry		Cage geometry	Gas phase geometry
N-H1, Å	1.0249	1.0174	B-N-H1, deg	111.99	111.12
N-H2, Å	1.0176	1.0174	B-N-H2, deg	111.60	111.12
B-H3, Å	1.2140	1.2087	N-B-H3, deg	106.12	104.91
B-H4, Å	1.2135	1.2087	N-B-H4, deg	107.72	104.91
B-N, Å	1.6153	1.6627	Cage volume†, Å^3	242.4	–

*Refer to figure 6.4(c); †Volume of truncated octahedron with heavy atoms being its vertices, figure 6.4(a). See appendix A for details.

Table 6.2: Geometrical parameters of molecular NH_3BH_3 in Cage 12.

significant, cf. the cohesive energy of the molecular crystal of AB is 21 kcal/mol (an estimation) [49]. It will be further shown that this cage immersed into a clathrate structure provides a similar stability as that of the AB molecular crystal. Below, we will provide a semi-quantitative estimation.

In the AB molecular crystal there are six effective dihydrogen bonds per molecule [49]. In gas phase structure of the cage each AB molecule is missing two dihydrogen bonds because of the absence of periodicity and the presence of dangling protons. There are eight dihydrogen bonds per each tetragonal face, the number of these faces is six, which gives four effective dihydrogen bonds per each AB molecule in the cage. Let us now estimate the energy of a single dihydrogen bond in the cage. The binding energy, averaged over the results obtained with different functionals, is 12.45 kcal/mol. Assuming that only four effective dihydrogen bonds contribute to this value, the energy of each bond would be 3.11 kcal/mol. Adding energies of two missing dihydrogen bonds to the binding energy of 12.45 kcal/mol we obtain an estimate of the cohesive energy of a hypothetical periodic structure of 18.67 kcal/mol, which is close to that of the AB molecular crystal. Even a higher value of 20.89 kcal/mol could be obtained with the PBE functional.

Before we consider larger polyhedrons we will criticize some other approaches to build AB clathrate cages. First, an arrangement of molecules shown in figure 6.2(a) may be regarded as the smallest possible cage of AB clathrates, which is consistent with the structural stability criterion. Unfortunately, the binding energy of an AB molecule in this cage is considerably smaller than that in Cage 12. BSSE corrected values of 9.09 kcal/mol and 9.53 kcal/mol have been obtained at the B3LYP/6-311G** and BP86/6-311G** levels of theory, respectively. Secondly, another possibility to arrange AB molecules along tetragonal faces of the truncated octahedron results in a distorted barrel like cage, the walls of which are built of AB dimers in geometry, which is presented in figure 5.4(a). We cannot envisage ways to build a periodic structure out of this cage, which would satisfy a construction principle requiring each proton to be engaged into formation of two dihydrogen bonds.

Name	Cage 12	Cage 24	Cage 60
Specification	$4^6 6^8$	$4^{12} 6^8 8^6$	$4^{30} 6^{20} 10^{12}$
AB molecules per cage	12	24	60
Circumsphere diameter†, Å	10.80	14.39	22.28
BSSE corrected binding energy, kcal/mol	11.82	11.90	11.54

†The longest distance between two atoms in the cage.

Table 6.3: Characteristics of possible AB clathrate cages.

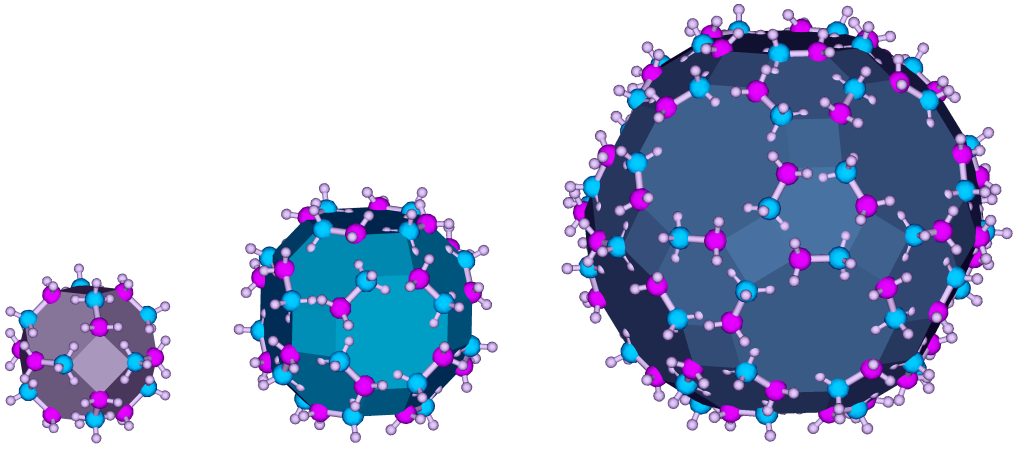

(a) Cage 12. (b) Cage 24. (c) Cage 60.

Figure 6.5: Possible AB clathrate cages.

In addition to this limitation, the cage is relatively unstable. The BSSE corrected binding energy of an AB molecule calculated with the 6-311G** basis set is 11.13 and 11.42 kcal/mol, obtained with the B3LYP and BP86 functionals, respectively. The energies are smaller than the corresponding values calculated for Cage 12 by about 0.5 kcal/mol. A geometry optimization performed with the PBE functional resulted in destruction of the cage structure. Due to the mentioned above reasons, these two cages were excluded from subsequent studies. Finally, another possibility is to rearrange Cage 12 by swapping heavy atoms within each AB molecule. There is no local minimum corresponding to this structure and geometry optimization of such an initial structure leads to the original Cage 12.

From this critique and from the previous discussion showing that a perpendicular arrangement of AB molecules is unfavorable, we conclude that we identified reasonable ways to construct cages of AB clathrates that satisfy the construction rules. It does not mean that we found for sure the most stable structures. If we did not, the stability of structures identified by us might be considered as a lower limit to the stability of real structures.

For the time being, we investigated a truncated octahedron and we formulated construction rules for cages built from AB molecules. Now, we will apply these rules to larger cages, Cages 24 and 60. A rigorous study of these cages, including Cage 12 for consistency, was done at the BP86/6-311G** level of theory. The forces

acting on atoms for Cages 12 and 24 were converged to $4.5 \cdot 10^{-4}$ Hartree/Bohr, for Cage 60 the forces were converged to $1.5 \cdot 10^{-3}$ Hartree/Bohr. No vibrational modes with imaginary frequencies were identified for the converged structures of Cages 12 and 24. Only geometrical optimization was done for Cage 60. The results are summarized in table 6.2 and the resulting cages are shown in figure 6.5. The stability of the cages is very similar, between 11.5 and 11.9 kcal/mol per one AB molecule. A smaller binding energy for Cage 60 could be an artifact of the less strict convergence criterion for forces. This criterion had to be relaxed for such a big system as convergence could not be achieved with the default value.

The knowledge of structure of possible cages of AB opens doors to further studies of clathrates of AB. The issue of solid state frameworks is addressed in chapter 7 and the hydrogen capacity of these cages is estimated in the following section.

6.3 Hydrogen Capacity of Cages

In this section we estimate the potential of Cages 12 and 24 for uptake of molecular hydrogen. Cage 60 seems to be less attractive for the formation of clathrates and storage of hydrogen. The task of finding a periodic structure, where each proton is involved into formation of two dihydrogen bonds, is far too complicated for Cage 60, although this structure may exist. The periodic structures identified by us that involve Cage 60 are less stable than those involving Cages 12 and 24 only, see chapter 7. Moreover, Cage 60 is not ideal for practical storage of hydrogen. Its large interior volume with a limited number of hydrogen binding sites localized on cage walls would encourage H_2-H_2 interactions between guest molecules, which are weak and characterized by a large equilibrium distance. This in turn would result in a less effective usage of the available space. It should be also said that the geometry optimizations for this cage loaded with H_2 would be extremely tedious due to the floppiness of the system.

As was demonstrated in a preliminary study of weak interactions in the NH_3BH_3-H_2 system, only methods accounting for dispersion may be used for the purpose of this estimation. For the sake of scientific curiosity and in order to have a reference point in the realm of known materials, we compare some results obtained for AB cages with analogous results obtained for water cages.

The hydrogen capacity of Cage 12 could be estimated by calculating the BSSE corrected interaction energy between the enclosed guest molecule(s) and the host molecules making up the cage. The number of guest molecules enclosed in the cage cannot increase beyond the point where the interaction becomes repulsive. The interaction energy between the host cage and a guest molecule, E_{HCG}, is found from equation 6.1.

Cage 12		Small water cage	
$1H_2$@Cage	$2H_2$@Cage	$1H_2$@Cage	$2H_2$@Cage
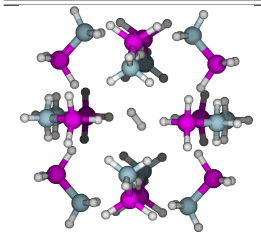	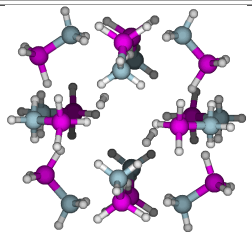	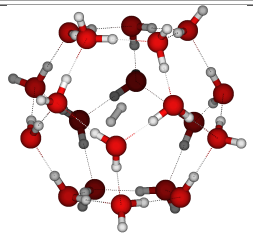	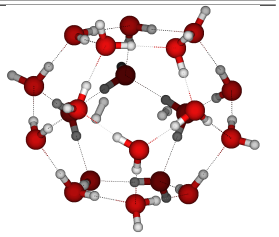
-1.24 kcal/mol	4.01 kcal/mol	-1.31 kcal/mol	1.13 kcal/mol

Table 6.4: Host cage-guest molecule(s) interaction energies in clathrates of AB and water.

$$E_{HCG} = E_{complex} - E_{cage} - E_{guest} + \triangle E_{cage} + \triangle E_{guest} \tag{6.1}$$

In equation 6.1 the first three terms are calculated with the basis set of the whole complex at the optimized geometry of the complex. The last two terms are one-body repulsive energies associated with a geometrical deformation of each monomer (cage or guest molecule) in the complex. They are calculated with the basis set of the monomer as a difference between the energy of the monomer at the complex geometry and its equilibrium geometry: $\triangle E_m = E_m(\text{complex geometry}) - E_m(\text{monomer equilibrium geometry})$.

The results of interaction energy calculations for Cage 12 and a small water cage of Structure II of hydrogen hydrates are summarized in table 6.3. The calculations were done at the MP2/aug-cc-pVDZ level of theory as implemented in the NWChem 5.1 package [145]. As it is seen, one hydrogen molecule could be stored attractively in Cage 12 and the interaction energy is comparable with that in the water cage. Two hydrogen molecules cannot be stored attractively in either cage. Hence, the hydrogen capacity of Cage 12 is one hydrogen molecule. It should also be mentioned that the result obtained for the water cage is consistent with experimental observations, which suggest that only one hydrogen molecule can be stored in the small water cage [83].

The hydrogen capacity of Cage 24 could be estimated using a similar approach to that used for Cage 12, although the number of attractively stored molecules might be larger than one. It is meaningful to recalculate the interaction energy per one guest molecule (specific interaction energy) and plot it against the number of these guests. One anticipates the following dependence of specific interaction energy on the number of enclosed hydrogen molecules. As the number of guests is small they essentially interact with cage walls only. As the number of guests is large enough they start to "feel" each other and the host-guest interactions are accompanied by guest-guest interactions and the specific interaction energy increases. As the number of guests increases further they begin to repel each other and are pushed close to

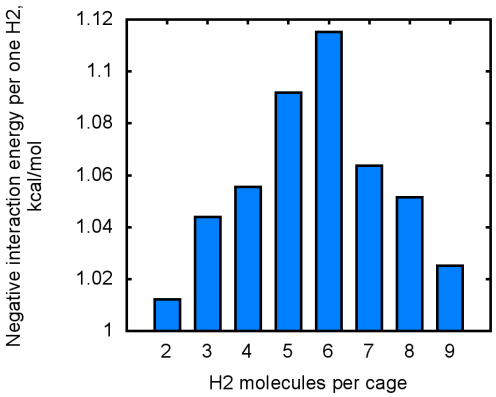

(a) Specific interaction energy of molecular hydrogen enclosed in Cage 24.

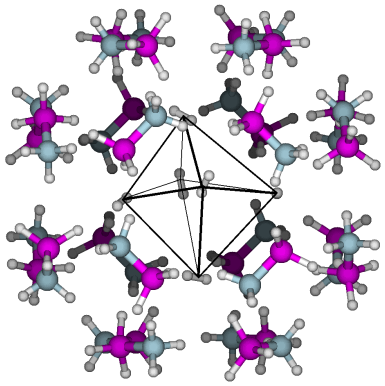

(b) Octahedral orientation of H_2 molecules enclosed in Cage 24.

Figure 6.6: Specific interaction energy of molecular hydrogen enclosed in Cage 24 and octahedral orientation of H_2 molecules enclosed in the cage.

the cage walls. In consequence, the specific interaction energy starts to decrease. We thus anticipate a maximum on the curve of specific interaction energy plotted against the number of guest molecules enclosed in the cage.

The size of the system under study forced us to apply the DFT-D instead of the MP2 theory. The results of calculations presented in figure 6.6 were obtained at the Becke97-D/6-311G** level of theory as implemented in the NWChem 5.1 package [145]. A maximum of the specific interaction energy of -1.12 kcal/mol is observed when six molecules are encapsulated in the cage, figure 6.6(a). An apparent observation from figure 6.6(b) is that six H_2 molecules are octahedrally arranged and are oriented towards octagonal faces of Cage 24; the number of these faces is also six. We thus must conclude that the most probable hydrogen capacity of this cage is six hydrogen molecules.

6.4 Conclusions

Principles governing orientation of AB molecules in possible clathrate structures have been derived. The first principle requires the structural stability of polygons to be satisfied, which is based on electrostatic arguments, and the second principle requires each proton of the molecule to be engaged in two dihydrogen bonds. On the basis of these principles three types of clathrate cages have been found, truncated octahedron, truncated cuboctahedron, and truncated icosidodecahedron. Two possible arrangements of AB molecules on faces of cages, along edges and face perpendicular, have been tested with a preferred arrangement being along edges. The binding energy of an AB molecule being a part of these cages and further immersed in a periodic structure was estimated to be comparable with the cohesive energy of the AB molecular crystal. The optimal number of hydrogen molecules encapsulated in Cages 12 and 24 was estimated to be one and six, respectively.

Chapter 7

Periodic Structures of Ammonia Borane Clathrates

7.1 Analysis of Space Filling Tessellations

We are now moving on from considering AB molecules as elementary building blocks to the treatment of AB clathrate cages as the simplest "bricks" of periodic structures. We approach the problem of construction of extended systems from formal grounds of geometry and we look at tessellations formed by the identified cages. The list of 28 known tilings of 3D space (honeycombs) was published in 1994 by B. Grünbaum acknowledging that the first correct enumeration of the tilings was done in 1991 by N. W. Johnson and independently by I. Alexeyev, [146] and references therein. In this list we encounter our cages several times. The truncated octahedron is found in items #10, #25, and #28, table 7.1. The truncated cuboctahedron is found in items #21, #25, and #27, table 7.1.

Let us first discuss in detail the tessellations of truncated octahedron, figure 7.1. The clathrates of AB could not exist in the form of a truncated alternated cubic structure shown in figure 7.1(a), #10 in the list, because it contains triangular faces violating the rule of structural stability of polygons, figure 6.1. Despite the absence of triangular faces in a bitruncated cubic honeycomb shown in figure 7.1(b),

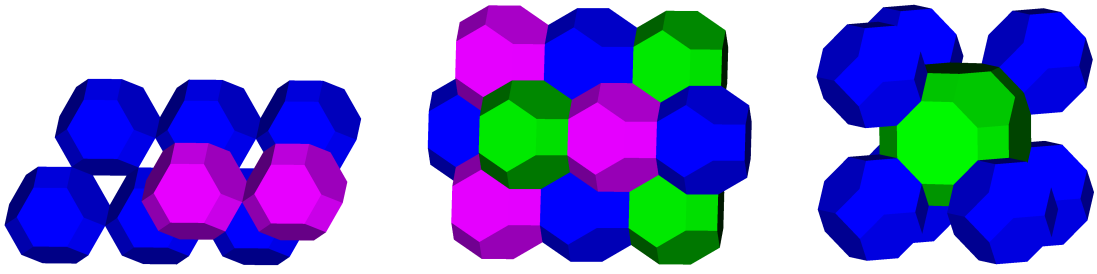

(a) Truncated alternated cubic honeycomb.

(b) Bitruncated cubic honeycomb.

(c) Cantitruncated cubic honeycomb.

Figure 7.1: Space filling tessellations of truncated octahedron.

Grünbaum's list # [146]	Honeycomb name	Polyhedrons meeting at each vertex of the tiling			Validity[§]
		Vertices configurations[†]	Names	Ratio[‡]	
#10	Truncated alternated cubic	(3, 4, 3, 4), $(3, 6, 6)^2$, $(4, 6, 6)^2$	Cuboctahedra, truncated tetrahedra, truncated octahedra	1:2:1	Not valid
#21	Cantitruncated alternated cubic	(3, 6, 6), (3, 8, 8), $(4, 6, 8)^2$	Truncated tetrahedra, truncated cubes, truncated cuboctahedra	2:1:1	Not valid
#25	Cantitruncated cubic	(4, 4, 4), (4, 6, 6), $(4, 6, 8)^2$	Cubes, truncated octahedra, truncated cuboctahedra	3:1:1	Valid
#27	Omnitruncated cubic	$(4, 4, 8)^2$, $(4, 6, 8)^2$	Octagonal prisms, truncated cuboctahedra	3:1	Valid
#28	Bitruncated cubic	$(4, 6, 6)^4$	Truncated octahedra	–	Not valid

[†]For definition see table 6.2, superscript indicates number of polyhedrons of certain kind meeting at each vertex of the tiling; [‡]Ratio of different polyhedrons in the tiling; [§]Validity for AB clathrates extended structure, see text for details.

Table 7.1: Uniform tilings formed with participation of truncated octahedron and truncated cuboctahedron.

#28 in the list, this structure could not be formed by AB either. The reason is the presence of shared tetragonal faces, which implies sharing of heavy atoms of two different molecules between each other. This could not be done without a chemical modification of AB itself. Item #25 of the list, a Cantitruncated Cubic Honeycomb (CCH) shown in figure 7.1(c), contains both cages of our interest, the truncated octahedron and the truncated cuboctahedron. This honeycomb does not violate the structural stability rules and does not have any other intrinsic defect preventing it from being formed by AB.

Let us continue with the tessellations of truncated cuboctahedron. In addition to the already discussed item #25 there are items #21 and #27, which are characterized in table 7.1. The honeycomb in item #21, which is called cantitruncated alternated cubic, contains triangular faces and thus violates the structural stability rule. The honeycomb in item #27, which is called the Omnitruncated Cubic Honeycomb (OCH), does not violate the structural stability rules and does not have any other intrinsic defect preventing it to be formed by AB. It will be considered in this chapter as a possible clathrate structure.

7.2 Other Hypothetical Clathrate Structures

In addition to rigorous geometrical considerations consistent with the construction principles formulated in chapter 6, the polarity and linear geometry of an AB molecule could be used to envisage and construct other extended structures of AB clathrates. We will look for such arrangements of cages where frustrations of the kind B-H...H-B and N-H...H-N are avoided. The number of possibilities is in prin-

ciple infinite and the search could hardly be formalized. We describe just several structures composed in this way, table 7.2, which were selected on the basis of our physicochemical intuition.

In the Shared Hexagonal Faces (SHF) structure two Cages 12 are connected through hexagonal faces in a way that AB molecules of one cage are shared with another cage giving a unit cell of the resulting periodic structure. In order to avoid frustrations and to enforce translational symmetry, the AB molecules on one hexagonal face of one of the cages are removed.

In the unit cell of the Not Shared Tetragonal Faces and Edges (NSTFE) structure two Cages 12 are connected through tetragonal faces, which are not shared between these cages. Unit cells in the resulting periodic structure are connected via edges of the cages, at which AB molecules interact with each other in a favorable arrangement similar to that shown in figure 5.4(a).

The unit cell of the Not Shared Hexagonal Faces (NSHF) structure contains one Cage 12 in a certain orientation, which by itself possesses translation symmetry. Unit cells in the resulting periodic structure are connected through hexagonal faces in one direction and via edges and through the B-H...H-N contacts in the other two directions.

The unit cell of the Not Shared Octagonal and Tetragonal Faces (NSOTF) structure contains one Cage 24 in a certain orientation, which by itself possesses translation symmetry. Unit cells in the resulting periodic structure are connected through octagonal faces in one direction and via tetragonal faces in the other two directions.

The unit cell of the Not Shared Tetragonal Faces (NSTF) structure contains one Cage 60 in a certain orientation, which by itself possesses translation symmetry. Unit cells in the periodic structure are connected via tetragonal faces of this cage in all three directions.

7.3 Screening of Periodic Structures

All seven hypothetical AB clathrate structures, two identified through space filling tessellations and five postulated on the basis of physicochemical intuition, were evaluated at the DFT level of theory, table 7.2. The calculations were performed for empty clathrate structures, i.e., guest hydrogen molecules were omitted at this stage. This approach was dictated by the inability of conventional DFT functionals to recover the dispersion dominated guest-host interactions. Of course, these interactions make the clathrate structure preferential over the molecular crystal plus gaseous hydrogen at certain conditions of pressure and temperature, see chapter 8 for details.

In table 7.2 we use a stability parameter. This is an increase in the ground state electronic energy per one AB molecule in a clathrate structure with respect to the

#	Name	Unit cell†	Periodic structure	Unit cell parameters‡	Stability§, kcal/mol
1	CCH	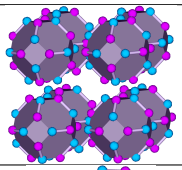	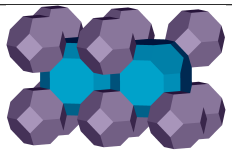	20.94 × 20.95 × 20.94 90.07 × 89.97 × 89.96 9186.55; 96	0.318
2	Shared Hexagonal Faces	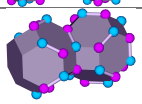	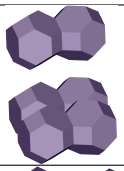	11.75 × 10.77 × 13.97 74.91 × 90.51 × 88.46 1706.22; 18	1.491
3	Not Shared Tetragonal Faces and Edges	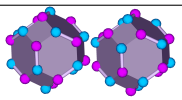	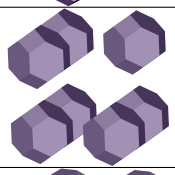	11.63 × 11.63 × 20.83 90.69 × 89.99 × 90.00 2817.25; 24	2.076
4	Not Shared Hexagonal Faces	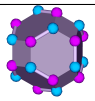	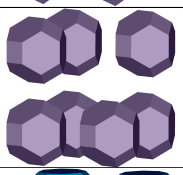	11.80 × 10.87 × 10.58 74.37 × 90.36 × 89.47 1307.51; 12	2.252
5	OCH	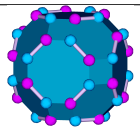	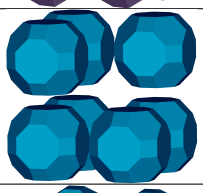	13.93 × 13.95 × 13.92 90.06 × 90.02 × 89.95 2704.22; 24	2.253
6	Not Shared Octagonal and Tetragonal Faces	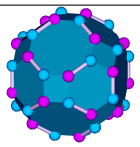	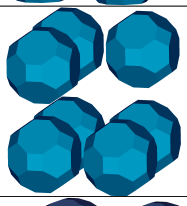	14.70 × 14.70 × 13.67 89.96 × 90.20 × 90.04 2953.73; 24	2.398
7	Not Shared Tetragonal Faces	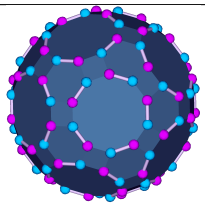	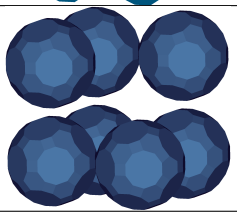	22.43 × 22.42 × 22.43 89.89 × 89.81 × 90.01 11275.52; 60	4.328

†Hydrogen atoms omitted for simplicity;

‡$a \times b \times c$, Å; $\alpha \times \beta \times \gamma$, deg; volume, Å^3; number of AB molecules;

§Increase in ground state electronic energy per one AB molecule with respect to molecular crystal.

Table 7.2: Possible periodic structures of AB clathrates and their characteristics.

analogous energy in the AB molecular crystal. The smaller the value the closer the clathrate structure energetically is to the AB molecular crystal. The stability defined in this way is a good figure of merit, which will be used to rank extended systems presented in table 7.2.

In initial calculations for empty clathrate structures we used the SIESTA method [129] with PBE functional, Double Zeta Polarized (DZP) basis set, $1 \times 1 \times 1$ k-points mesh density, 0.005 Ry for excitation energy of orbitals due to the confinement, and 200 Ry for kinetic energy of plane waves which could be represented on the grid without aliasing.

The CCH structure is significantly more stable than others. In this structure each protic hydrogen is engaged in two dihydrogen bonds, as in the molecular crystal of AB. For this structure, an increase in ground state electronic energy per one AB molecule with respect to the AB molecular crystal is only 0.32 kcal/mol. The same parameter calculated for the Structure II of hydrates, the structure of hydrogen hydrates with all protons placed according to the Bernal-Fowler rules, is 0.18 kcal/mol. This is an increase in the ground state electronic energy per one water molecule in the empty hydrate with respect to the ordinary ice Ih. These values are of the same order of magnitude and the accuracy of DFT, in particular its SIESTA implementation (*vide infra*), is not sufficient to reach any stronger conclusion. In addition, the CCH structure of AB is a hypothetical structure, while the Structure II of hydrates is real, i.e., experimentally confirmed. There might exist hydrogen clathrates of AB, which are more stable than the CCH structure.

Other clathrate structures, in particular those built from larger cages, are less stable than the CCH structure, though differences in the stability parameter are very small, 1.2–4.0 kcal/mol. The smaller stability results from the fact that not every protic hydrogen is engaged in two dihydrogen bonds, or these bonds must be distorted. The stability of structures designed on the basis of physicochemical intuition, e.g., the SHF structure, is surprisingly high. We conclude that there is some uncertainty left about the most stable clathrate structures of AB, which results from our search procedure, limitations of current DFT functional, and limited applicability of electronic energies at elevated temperatures and pressures. As for now, the CCH structure is the most promising. The structure has a cubic unit cell with lattice vectors of about 21 Å, which contains eight Cages 12, four Cages 24, and 96 AB molecules composing these cages, figure 7.2.

The similar stability of the molecular crystal of AB and the CCH structure was further exposed by performing more accurate DFT calculations using a conventional plane wave DFT implementation of the Vienna *Ab-Initio* Simulation Package (VASP) code [147, 148, 149, 150, 151, 152]. The PBE functional has been used with high precision turned on which results in a 30% increase of the default kinetic energy cutoff for plane waves. $1 \times 1 \times 1$ k-points mesh density has been used for both the

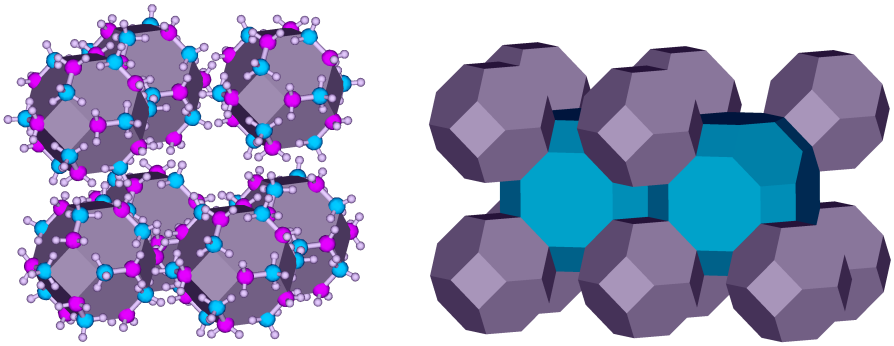

(a) Connection of cages in unit cell of the CCH structure of AB clathrates (one Cage 12 and faces of Cages 24 are removed).

(b) Periodic structure of the CCH framework of AB clathrates (all cages are shown explicitly).

Figure 7.2: Connection of cages in unit cell and periodic structure of the CCH framework of AB clathrates.

Parameter	AB crystal	CCH structure
NB, Å	1.595	1.595
NH, Å	1.030	1.031
BH, Å	1.223	1.224
NBH, deg.	108.381	107.955
BNH, deg.	111.698	112.223
NH...HB, Å	2.116	2.061

Table 7.3: Average inter- and intramolecular parameters of AB molecular crystal and the CCH structure of AB clathrates.

CCH structure and AB molecular crystal. A super cell $3\times3\times3$ has been constructed for the molecular crystal. Forces on atoms have been converged to 0.01 eV/Å. The electronic energy for the CCH structure has been found to be 0.5 kcal/mol lower per formula unit than that for the AB molecular crystal. The symmetry space group of the CCH structure was found to be Fm3c, with a cubic unit cell of dimension 21.31 Å.

Important structural parameters for both the AB molecular crystal and the CCH structure are summarized in table 7.3. There is practically no difference in intramolecular bond lengths. In the CCH structure the NBH angles are slightly closed and the BNH angles are slightly opened in comparison with the molecular crystal. There is also a slight contraction of dihydrogen bonds in the CCH structure.

Finite temperature effects might be critical for the relative stability of the CCH structure and AB molecular crystal. For this reason *ab-initio* dynamics simulations were performed at 3 K and 77 K. The unit cell of the CCH structure and a $3\times3\times3$ super cell of the AB molecular crystal have been used in these simulations. The free energy was calculated from the phonon density of states, which in turn was obtained from the Fourier transform of the atomic velocity autocorrelation function, see appendix B for details. The NVE microcanonical ensemble simulations with the

Material	Unit cell volume, Å^3	Unit cell formula	Density†, g/cm^3	Weakly bound H_2, wt%	Strongly bound H_2, wt%	Total H_2, wt%
CCH structure of AB clathrates‡	9677.2 (9186.6)	$32H_296NH_3BH_3$	0.52/0.11 (0.55/0.12)	2.1	19.2	21.3
Molecular crystal of AB	131.5	$2NH_3BH_3$	0.78/0.15	0	19.6	19.6

†Volumetric density of the material itself / of the hydrogen; ‡SIESTA estimations are shown in brackets.

Table 7.4: Bulk properties of the CCH structure of AB clathrates and AB molecular crystal.

CP2K code [153, 154, 155] were done using the triple-zeta quality basis set and the PBE functional. Dynamics of each system was recorded over 15 thousand of 0.5 femtosecond time steps. At 3 K the free energy of the CCH structure was found to be 1.8 kcal/mol lower per formula unit than that of the AB molecular crystal. However, at 77 K, stability of both systems is very similar as the difference in free energies is less than 0.5 kcal/mol per formula unit, with the AB molecular crystal being more stable. The value at 77 K corresponds to 3 kT and is smaller than the DFT methodological uncertainty.

7.4 Hydrogen Capacity

An estimation of hydrogen capacity of the CCH structure can be done straightforwardly under the assumption that the Cages 12 and 24 immersed in the condensed phase retain the same number of hydrogen molecules as they do in the gas phase, see section 6.3. We therefore expect six H_2 molecules enclosed in each Cage 24, the number of which is four in the unit cell, and one H_2 molecule enclosed in each Cage 12, the number of which is eight in the unit cell. The overall molecular hydrogen capacity of the unit cell is thus 32 H_2 molecules. Other important properties of the material and their comparison with those of the AB molecular crystal are summed up in table 7.4. The clathrate differs from the molecular crystal by a smaller overall material density and the hydrogen volumetric density. On the other hand, the clathrate is characterized by a larger gravimetric density of hydrogen, which is due to the presence of physically bound molecular H_2.

7.5 Conclusions

In this chapter we extended our study of gas phase structures of ammonia borane cages into the realm of condensed matter. Seven periodic structures of possible clathrates of AB have been identified based on the analysis of uniform tilings of 3D space and structural features and properties of AB molecules. The screening and evaluation of these structures has been performed at the DFT level of theory

resulting in the identification of the CCH structure of AB clathrates as being significantly more stable than others, even more stable than molecular crystal of AB at sufficiently low temperatures. The hydrogen capacity of the CCH structure was found to be 21 wt% out of which 2 wt% would be kinetically easily accessible.

Chapter 8

Thermodynamic Stability of Ammonia Borane Clathrates

8.1 Relationship Between Thermodynamic Stability of Clathrates and Host-Guest Intermolecular Interactions

As a preamble to this chapter some qualitative reasoning inspiring the development of a model discussed here should be mentioned. Observing hydrates formed in nature it is easy to note that those hydrates, where guest molecules interact with water hosts strongly, are more stable, i.e., they exist under lower pressures and higher temperatures, figure 8.1 [90, 83]. The hydrates of methane and hydrogen provide striking examples. In this chapter we develop a model, which represents this idea in quantitative terms.

In order to link the PT stability of clathrates with intermolecular interactions between host molecules of the clathrate cage and the enclosed guest molecule, we consider the change in free energy for the process shown in equation 8.1.

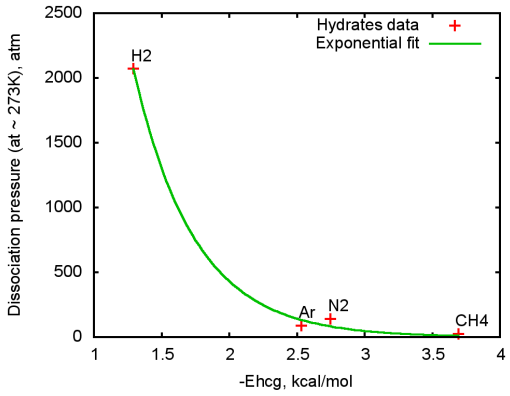

Figure 8.1: Hydrates dissociation pressures as a function of small host cage-guest molecule interaction energy calculated at the Becke97-D/6-311G** level of theory.

$$\text{Gas} + \text{Cage} \rightarrow \text{Gas@Cage} \tag{8.1}$$

We assume that the enthalpy change for the process of enclathration results solely from a stabilizing effect of host-guest interactions and the entropy change could be found as a difference between the translational entropy of a monatomic gas calculated from the Sackur-Tetrode equation and the entropy of a particle in a spherically symmetric rectangular potential well, the cage. The nonideality of real gases is taken into account at the stage of calculation of the Sackur-Tetrode entropy, where volume of one mole of the gas is calculated from the van der Waals equation of state. Under the above assumptions, the clathrate phase and the molecular crystal plus free gas are at equilibrium when a difference in free energy for the process 8.1 is zero, equation 8.2.

$$\begin{aligned} \triangle G = \triangle H - T\triangle S \approx \\ \approx E_{HCG} - T(S_{PSB} - S_{ST}) = 0 \end{aligned} \tag{8.2}$$

E_{HCG} is the interaction energy between the host cage and the guest molecule; S_{ST} is the Sackur-Tetrode entropy; S_{PSB} is the entropy of particles entrapped in spherically symmetric rectangular potential wells.

The interaction energy between the host cage and the guest molecule is found from *ab-initio* electronic structure calculations according to equation 6.1. For one mole of an ideal gas the entropy S_{ST} can be found from the Sackur-Tetrode equation, equation 8.3 [156, p. 580].

$$S_{ST} = R\ ln\left(\frac{e^{5/2}V}{N_A \Lambda^3}\right) \tag{8.3}$$

Here, $\Lambda = h/(2\pi mkT)^{1/2}$ is the thermal de Broglie wavelength of the molecule; V is the volume of one mole of gas.

The volume V is found from the van der Waals equation of state, equation 8.4 [156, p. 17], by solving it iteratively, with a starting volume obtained from the ideal gas law $V = RT/P$.

$$V = \frac{RT}{P + a/V^2} + b \tag{8.4}$$

The entropy of particles entrapped in spherically symmetric rectangular potential wells, S_{PSB}, is found from the canonical partition function Q according to equation 8.5 [156, p. 579].

$$S_{PSB} = \frac{U - U(0)}{T} + k\ lnQ \tag{8.5}$$

Here, $U(0)$ and U are internal energies of entrapped particles at 0 K and finite

T, respectively; $Q = q^N$ is the canonical partition function which can be found from the molecular partition function q of N distinguishable (by their positions, see comments below) particles.

$$U = U(0) - \left(\frac{\partial lnQ}{\partial \beta}\right)_V \tag{8.6}$$

Here, $\beta = 1/kT$ and for one mole of the gas, when $N \equiv N_A$, both equation 8.6 and equation 8.5 can be rewritten in a form of equation 8.7 and equation 8.8, respectively.

$$U - U(0) = -N_A \left(\frac{\partial lnq}{\partial \beta}\right)_V = -N_A \left[\frac{1}{q}\left(\frac{\partial q}{\partial \beta}\right)_V\right] \tag{8.7}$$

$$S_{PSB} = \frac{U - U(0)}{T} + kN_A\ lnq \tag{8.8}$$

The molecular partition function, q, is found from equation 8.9, where g_i is the degeneracy of the energy level E_i, [156, p. 564].

$$q = \sum_i g_i \exp\left(-\frac{E_i}{kT}\right) \tag{8.9}$$

To find the energy levels of a particle in a spherical potential well we consider the radial part of the Schrödinger equation describing particle's motion in a region, where the potential is finite, equation 8.10 [157, p. 125], which may be presented in the form of equation 8.11 [157, p. 126].

$$\left[\frac{\hbar^2}{2\mu}\frac{d^2}{dr^2} + E - \frac{\hbar^2 l(l+1)}{2\mu r^2}\right] rf(r) = 0 \tag{8.10}$$

$$\begin{gathered}\left[\frac{d^2}{dz^2} + \frac{2}{z}\frac{d}{dz} + 1 - \frac{l(l+1)}{z^2}\right] f(z) = 0, \\ \text{or } \left[z^2\frac{d^2}{dz^2} + 2z\frac{d}{dz} + z^2 - l(l+1)\right] f(z) = 0\end{gathered} \tag{8.11}$$

Here, $z = kr$ and $k^2 = 2\mu E/\hbar^2$, μ is the particle mass.

Equation 8.11 is the spherical Bessel differential equation, the general solution of which is a linear combination of the spherical Bessel $j_l(kr)$ and Neumann $\eta_l(kr)$ functions, equation 8.12.

$$f_l(r) = Aj_l(kr) + B\eta_l(kr) \tag{8.12}$$

By requiring a finite value of the wave function at the center of the well, we must set $B = 0$ as the spherical Neumann functions tend to minus infinity when r tends to zero. The value of A is determined from the normalization condition and the

total wave function is found from equation 8.13, with $Y_{lm}(\boldsymbol{\theta}, \boldsymbol{\phi})$ being the spherical harmonics, l being the orbital (angular momentum) quantum number, and m being the magnetic quantum number.

$$\psi_{klm}(r) = Aj_l(kr)Y_{lm}(\boldsymbol{\theta}, \boldsymbol{\phi}) \tag{8.13}$$

By requiring continuity of the wave function, which vanishes at $r = r_s$, r_s is the radius of the spherical potential, we set $j_l(kr_s) = 0$. Denoting the roots of the spherical Bessel function as X_{nl} we find that $k = X_{nl}/r_s$, from which it follows that the energy levels of a particle in the spherical potential well are given by equation 8.14 [157, p. 129]. Each energy level is $2l + 1$ degenerate, with l being the angular momentum quantum number.

$$E_{nl} = \frac{\hbar^2 X_{nl}^2}{2\mu r_s^2} \tag{8.14}$$

Here, X_{nl} is the n-th root of the spherical Bessel function $j_l(z)$ and n is the principal quantum number ($n = 1, 2, 3...$); l is the order of $j_l(z)$, the angular momentum quantum number ($l = 0, 1, 2...$); r_s is the radius of the spherical potential well.

The spherical Bessel functions [158] and their relation to the sinc function (known as the Rayleigh's formula) [159, p. 439] are given by equation 8.15. Appendix C gives details on numerical implementation of the spherical Bessel functions.

$$j_l(z) = 2^l z^l \sum_{p=0}^{\infty} \frac{(-1)^p (p+l)!}{p!(2p+2l+1)!} z^{2p} = z^l \left(-\frac{1}{z}\frac{d}{dz}\right)^l \frac{\sin z}{z} \tag{8.15}$$

To estimate the radius of the spherical potential well, r_s, we use an expression presented in equation 3.10, with parameters ϵ, a, σ obtained from *ab-initio* calculations. The actual value of r_s is taken as a solution of the equation $w(r) = 0$.

As the proposed model is based primarily on compensating the entropy term associated with enclathration, $T(S_{PSB} - S_{ST})$ with the enthalpy term, it is enough to consider the smallest cages only. Guest molecules in the smallest cages are well localized and are in the highest state of order (confinement). In consequence, these molecules are the most difficult to stabilize with attractive host cage-guest molecule interactions. At the conditions under which the smallest cages are stable, the large cages are stable by default, unless they are disfavoured by unexpectedly weak host-guest interactions. Another important point, as the small cages can accommodate one hydrogen molecule only, the canonical partition function for an ensemble of molecules entrapped in these cages can be approximated with $Q = q^N$.

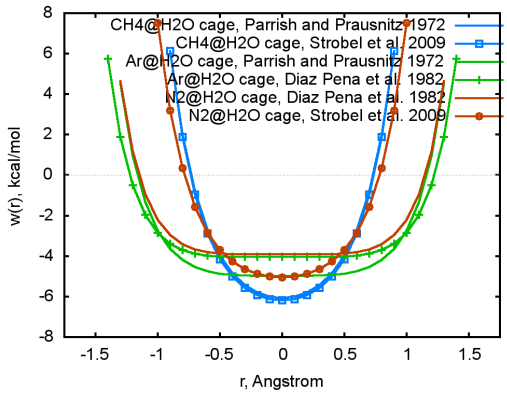

(a) Small cavity empirical potentials of CH_4, Ar, and N_2 hydrates [105, 106, 160].

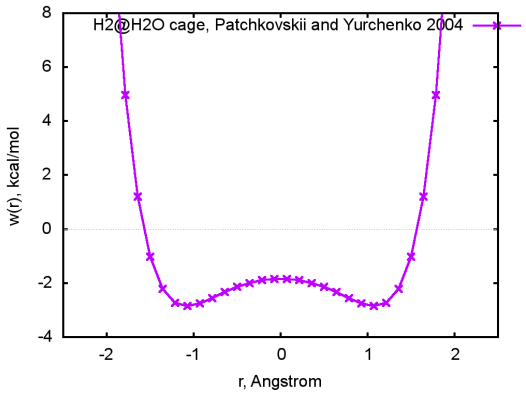

(b) Small cavity *ab-initio* potential of H_2 hydrates [96].

Figure 8.2: Small cavity potentials of CH_4, Ar, N_2, and H_2 hydrates.

8.2 Stability of Hydrates of CH_4, Ar, N_2, and H_2

To demonstrate the performance of the model we tested it on known hydrates of CH_4, Ar, N_2, and H_2. To estimate a radius of the potential well for the CH_4, Ar, and N_2 hydrates we constructed empirical cavity potentials using parameters of the Kihara intermolecular potentials published in refs. [105, 160]. These potentials and their comparison with earlier publications [106, 160] are presented in figure 8.2(a). As it is seen from the figure the values of r_s is fairly insensitive to the details of the potentials with an exception of N_2 hydrates. In the following we assume that the newer data are more accurate. To estimate r_s for the H_2 hydrates we use an *ab-initio* MP2/DZ potential, as published in [96], figure 8.2(b). The host cage-guest molecule interaction energies, E_{HCG}, for all hydrates are calculated at the Becke97-D/6-311G** level of theory with the NWChem 5.1 package [145]. For the H_2 hydrates this quantity is also calculated at the MP2/aug-cc-pVDZ level of theory.

The diagrams representing results, figure 8.3, show the $T(S_{ST} - S_{PSB})$ term as a function of pressure and temperature. The area where this term is counterbalanced by $E_{HCG} \pm 5\%$ is highlighted. A selection of $\pm 5\%$ is arbitrary and it reflects the inherent inaccuracy of electronic structure methods, in particular exchange-correlation functional, in determination of E_{HCG}. For comparison, experimental lines bordering the hydrate stability zones are also depicted, [82, 83, 161, 162, 163].

The model performance for hydrates of CH_4 is poor, figure 8.3(a). Even though the agreement with high temperature experimental data is satisfactory, the slope of the experimental line is very different from the slope of the calculated bordering line. A much better agreement, up to a constant shift, between the theoretical and experimental bordering lines could be observed for the Ar and N_2 hydrates, figures 8.3(b) and 8.3(c). The agreement becomes quantitative for the H_2 hydrates, figure 8.3(d). In this case the theoretical predictions are almost insensitive to the level of theory, cf. figures 8.3(d) and 8.3(e). The following observations can be

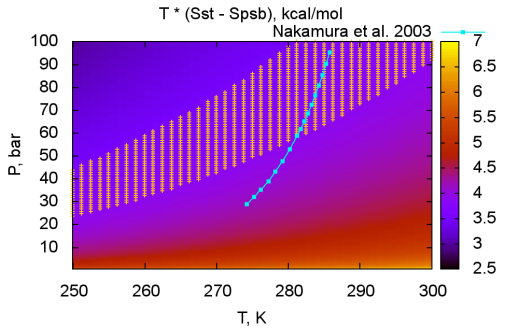

(a) Stability zone of CH_4 hydrates, [161].

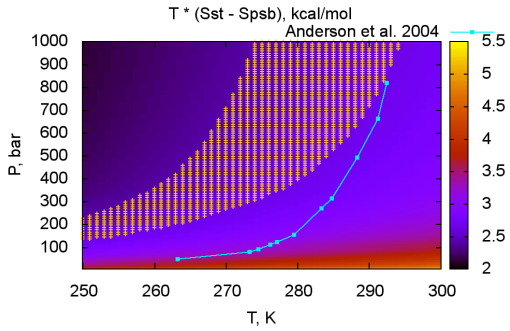

(b) Stability zone of Ar hydrates, [162].

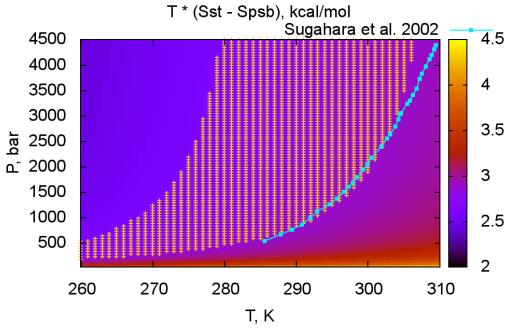

(c) Stability zone of N_2 hydrates, [163].

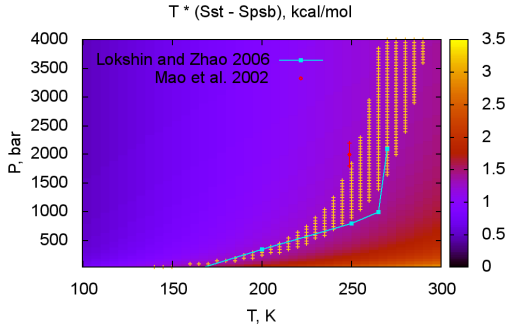

(d) Stability zone of H_2 hydrates (Becke97-D/6-311G**), [82, 83].

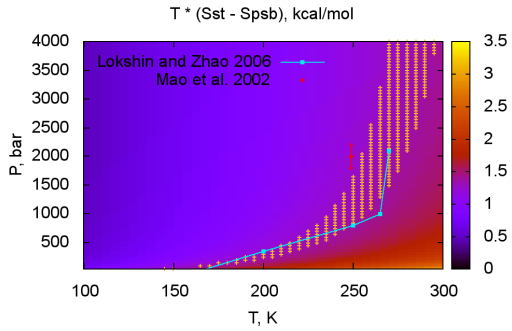

(e) Stability zone of H_2 hydrates (MP2/aug-cc-pVDZ), [82, 83].

Figure 8.3: Stability zones of CH_4, Ar, N_2, and H_2 hydrates predicted by the statistical model.

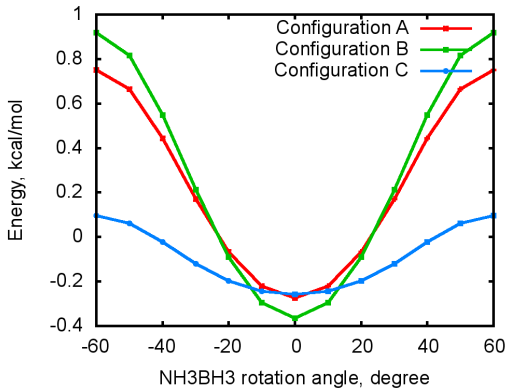

Configurations A, B, and C are presented in figure 5.5 and show relative molecular orientations when a rotation angle of NH_3BH_3 is zero. Separations of two molecules correspond to the minimum of intermolecular potential for a given configuration. The BSSE corrected interaction energies are computed at the MP2/aug-cc-pVDZ level of theory.

Figure 8.4: Sensitivity of AB-H_2 intermolecular potentials to rotation of AB molecule around BN axis.

made. Firstly, the smaller the molecule the better the agreement between experiment and theory. Secondly, a satisfactory performance of the model for hydrates can be expected below the ice melting point. For a further discussion of model's limitations see section 8.5.

8.3 Stability of H_2 Clathrates of Ammonia Borane

We now apply the model to estimate the PT stability zone of hypothetical clathrates of AB. To obtain a radius of the spherical potential well of the cage we consider a AB-H_2 intermolecular potential averaged over several configurations. In addition to the three configurations discussed in section 5.3, it is necessary to study other mutual arrangements of AB and H_2 due to sensitivity of the potential to rotations of the AB molecule, figure 8.4. Taking into account AB-H_2 orientations in cages of AB, configurations which are of particular interest are D, E, and F, figure 8.5. In these configurations one of hydridic hydrogens of AB is directed towards molecular hydrogen. For consistency, intermolecular potentials of these configurations and configurations A, B, and C have been calculated at the MP2/aug-cc-pVTZ level of theory with the Gaussian 03 package [144], figure 8.6.

The sensitivity of AB-H_2 intermolecular potentials to rotations of the AB molecule is reflected in the depth of these potentials and in positions of their minima, figure 8.6. The configurations D, E, and F are characterized by shallow potentials and more distant minima in comparison to the configurations A, B, and C. With regard to preferential orientation of AB molecules in cages of AB clathrates, the usage of the ABC or ABCDEF averaged intermolecular potentials would lead to unjustifiably

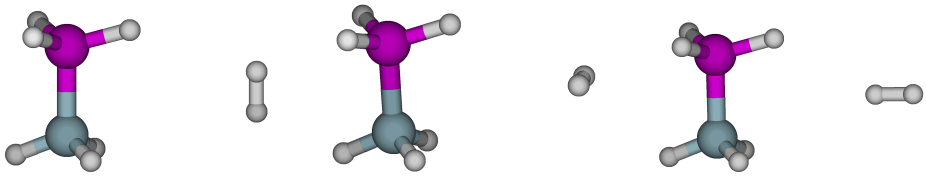

(a) Configuration D. (b) Configuration E. (c) Configuration F.

Figure 8.5: Studied molecular configurations of the AB-H_2 system.

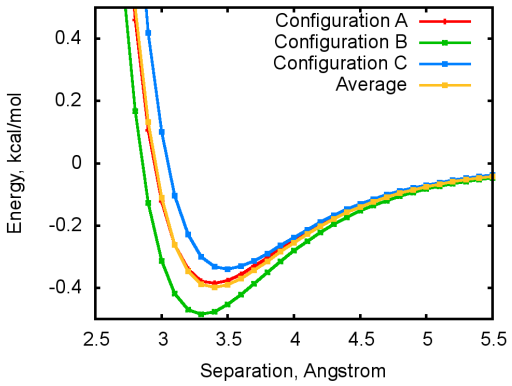

(a) Intermolecular potentials for configurations A, B, and C of the AB-H_2 system and their average.

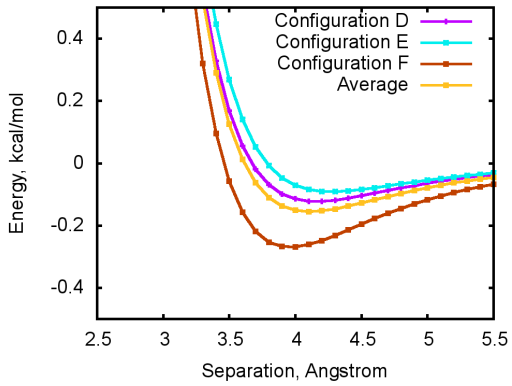

(b) Intermolecular potentials for configurations D, E, and F of the AB-H_2 system and their average.

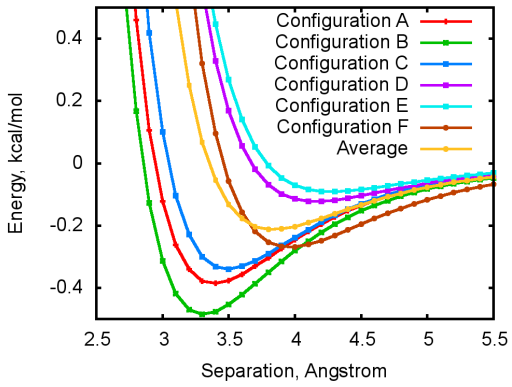

(c) Intermolecular potentials for configurations A, B, C, D, E, and F of the AB-H_2 system and their average.

The BSSE corrected interaction energies are computed at the MP2/aug-cc-pVTZ level of theory.

Figure 8.6: Intermolecular potentials and their averages for different configurations of the AB-H_2 system.

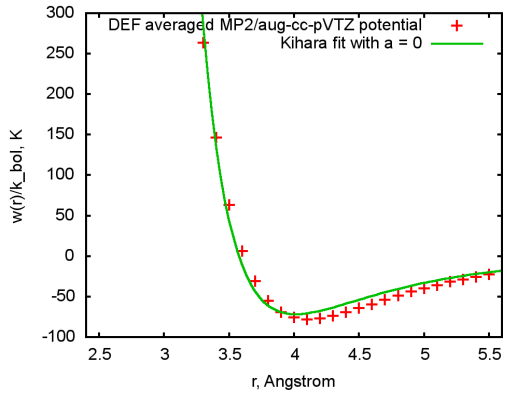

(a) Fitting of the Kihara potential to the DEF AB-H_2 averaged intermolecular potential.

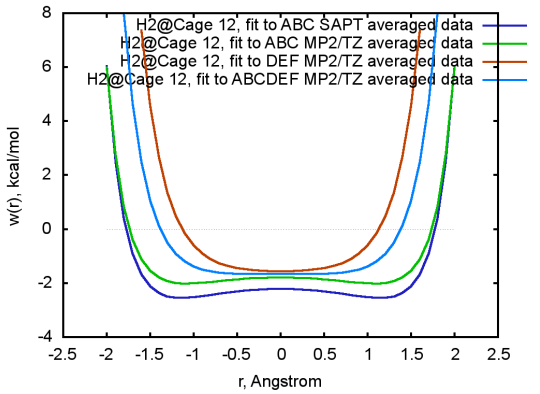

(b) Spherical Cage 12 potentials for the ABC, DEF, and ABCDEF configurations averaged data.

Figure 8.7: Kihara fit to the DEF averaged potential and spherical Cage 12 potentials.

deep potential and to an overestimation of the value of r_s. To construct realistic potentials for cages of AB to obtain meaningful values of r_s, it is more reasonable to use the DEF averaged potential.

Direct fitting of equation 3.9 to the DEF averaged potential gives a negative value for the radius a of the spherical core representing the gas molecule, which is unphysical. Setting a to zero reduces equation 3.9 to the Lennard-Jones potential but does not lead to unphysical results, figure 8.7(a). To get a spherical potential for Cage 12 one uses equation 3.10 together with the values of fitted parameters. The results and their comparison with the SAPT data are shown in figure 8.7(b). Different Kihara potentials obtained from fitting to the averaged ABC and ABCDEF potentials are given in appendix D. A comparison of the spherical potentials obtained from the SAPT and MP2 calculations for the ABC configurations shows that the SAPT potential is deeper but the r_s value is fairly insensitive to the level of theory. At the same time the value of r_s is very sensitive to the configurations used to construct the spherical potential and it, therefore, justifies the choice of the DEF configurations for obtaining the r_s value, due to their dominance in the clathrate cages of AB.

Spherical potentials for the three identified cages of AB are shown in figure 8.8. The figure clearly shows that the largest cage is not better for hydrogen storage than the smaller cages. The development of a hump at the center of the large cage suppresses binding of hydrogen molecules in this region and reduces the useful volume. Indeed, for Cage 60 the potential reaches practically zero in a wide region at the middle of the cage.

With the value of r_s found from the spherical potential for Cage 12, we represent the term $T(S_{ST} - S_{PSB})$ as a function of pressure and temperature in the same way as we did for hydrates, figure 8.9. The area where this term is balanced by $E_{HCG} \pm 5\%$ is highlighted.

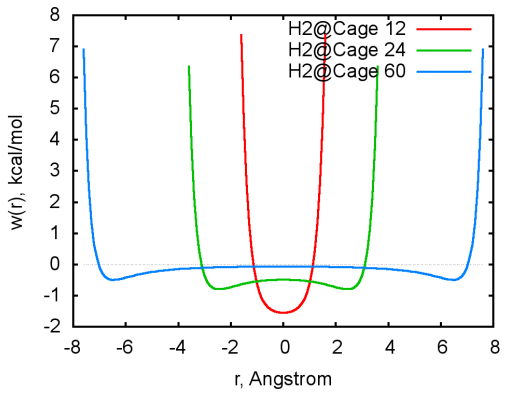

Figure 8.8: Spherical potentials of AB clathrate cages.

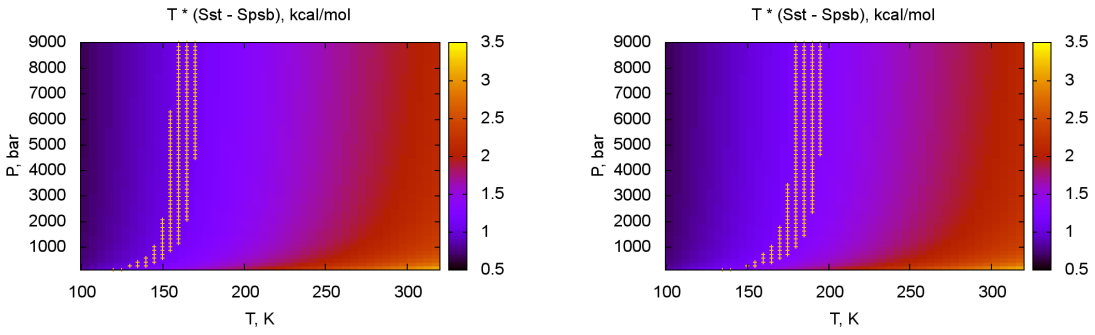

(a) $E_{HCG} \pm 5\%$ is calculated at Becke97-D/6-311G** level of theory.

(b) $E_{HCG} \pm 5\%$ is calculated at MP2/aug-cc-pVDZ level of theory.

Figure 8.9: Stability zone of H_2 clathrates of ammonia borane.

A relatively small radius of the spherical cavity for Cage 12, r_s = 1.13 Å, leads to localization of the enclosed molecular hydrogen and to relatively small values of S_{PSB}. In addition, the cage-guest molecule interactions are small, only -1.08 kcal/mol and -1.24 kcal/mol at the Becke97-D/6-311G** and MP2/aug-cc-pVDZ levels of theory, respectively. In consequence, very high pressures are required to stabilize the AB hydrogen clathrates at standard temperature. On the other hand, lowering the temperature has a profound effect on the stability of this hypothetical material, *vide infra*.

8.4 Effect of Pressure and Temperature on Stability of Clathrates

For a detailed study of pressure and temperature effects on the stability of hydrogen clathrates of water and AB, we consider the dependence of $T(S_{ST} - S_{PSB})$ upon one parameter with a fixed value of the other, figure 8.10. In this figure the horizontal lines show E_{HCG} calculated at the MP2 and DFT-D level of theory. Below these lines the entropic term is counterbalanced by the host cage-guest molecule interaction energy and the clathrate is stable. Above the lines the entropic term dominates over the host cage-guest molecule interaction energy and the clathrate is unstable.

As could be seen from figures 8.10(a) and 8.10(b), the effect of pressure on clathrate's stability becomes very minor after a certain threshold pressure around 1000–3000 bar. At pressures higher than the threshold value the term $T(S_{ST} - S_{PSB})$ remains practically unchanged. The stability of hydrates at lower pressures in comparison with the AB clathrates is a sole effect of the cage size, which is larger for water than for AB. Hydrogen in a larger cage is less localized and thus closer in entropy to gaseous hydrogen.

In contrast to pressure, the effect of temperature on the stability of clathrates is very significant over a wide range of T, figures 8.10(c) and 8.10(d). A reduction of temperature to 77 K stabilizes both types of clathrates at ambient pressure, figures 8.10(a) and 8.10(b). The differences in theoretical predictions based on DFT-D and MP2 are insignificant for hydrates and noticeable for clathrates of AB.

8.5 Critique of Proposed Statistical Model

Contrary to the van der Waals and Platteeuw model, which is based on the grand canonical partition function for water (host), the model proposed in this work is based on the properties of a guest molecule, the size of the smallest occupied cage in clathrate, and the energy of guest-host cage interaction.

In its current form the model neglects energy difference between an empty clathrate framework and the molecular crystal, which seems to be reasonable as

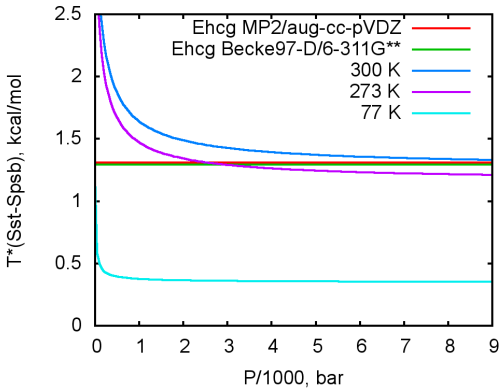

(a) Effect of pressure on stability of hydrogen hydrates.

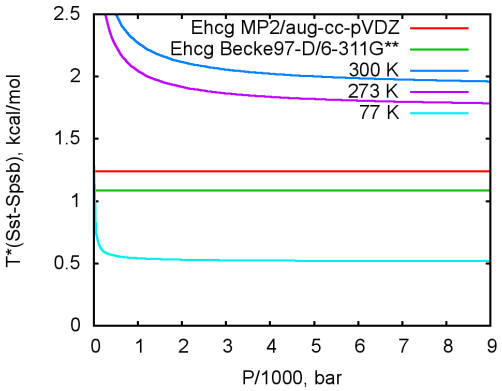

(b) Effect of pressure on stability of hydrogen clathrates of AB.

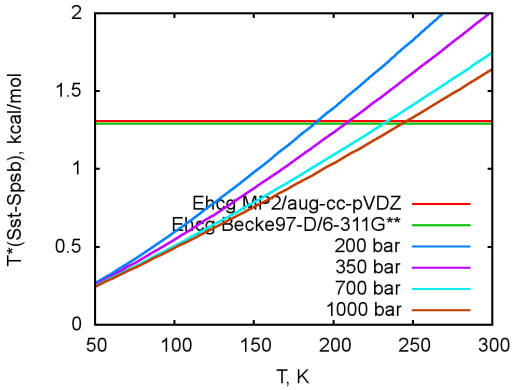

(c) Effect of temperature on stability of hydrogen hydrates.

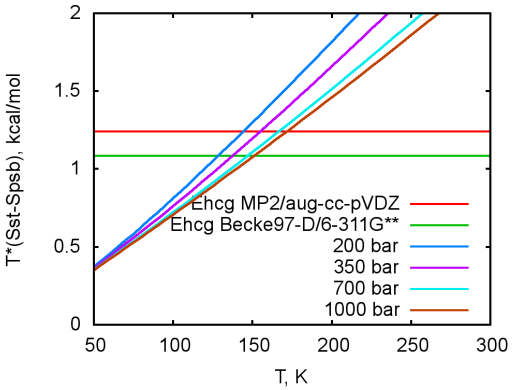

(d) Effect of temperature on stability of hydrogen clathrates of AB.

Figure 8.10: Effect of pressure and temperature on stability of hydrogen clathrates.

our results for the corresponding periodic structures demonstrate. In general, the model neglects existence of other phases of the host (molecular crystal, liquid) apart from the empty clathrate framework.

The model estimates the stability of clathrate structure on the basis of stability of its smallest occupied cage, which is the most difficult to stabilize from the entropic point of view. Entropy of guest molecules in larger cages is assumed to be higher, than that in the smallest cage. The model could not be applied if there is more than one guest molecule in the smallest cage.

Another approximation is that the entropy of gaseous species is calculated as the entropy of the ideal gas, volume of which is assumed to be equal to volume of the van der Waals gas.

The potential experienced by guest molecules inside cages is approximated by a spherically symmetrical infinite rectangular potential. This potential is used to calculate energy levels and entropy of enclathrated guest molecules. The guest molecule itself is assumed to be structureless. An experimental justification of this assumption, at least for molecular hydrogen, could be found in [99]: "The frequency of the hydrogen roton in the Raman spectrum of H_2 guest in the cages was found to be identical to that of free H_2. This indicates that the H_2 molecules in the clathrate cages are in free rotational states. It is thus a reasonable approximation to use the isotropic van der Waals potential to describe H_2-H_2 and H_2-H_2O interactions." An approximation of the real potential with an infinite spherical well could further be justified by demonstrating that numerical solutions of a one-dimensional, one-particle Schrödinger equation of the form 8.10 are similar when the infinite spherical well is replaced with the cage potential $w(r)$, equation 8.16.

$$\left[\frac{d^2}{dr^2} - \frac{l(l+1)}{r^2} + \frac{2\mu}{\hbar^2}\left(E - w(r)\right)\right] rf(r) = 0 \tag{8.16}$$

The Numerov method, see for example [164], to solve this special kind of the second order differential equations, which does not contain the first derivative, has been implemented and tested in [96]. We modified the existing code to account for the potential experienced by a hydrogen molecule in the AB cage. We found 121 energy levels with the ground state at -1.2 kcal/mol. The largest angular momentum quantum number considered was 22. These energy levels were then used to calculate the PT stability zone of the AB hydrogen clathrates. For hydrogen hydrates, the energy levels were taken from [96] and the stability zone has been calculated analogously, figure 8.11. Similarity of these diagrams to those presented before for hydrogen clathrates, with spherical potentials modelled with infinite wells, validates our original approach.

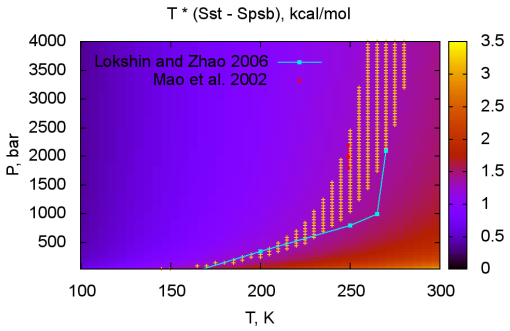

(a) $E_{HCG} \pm 5\%$ for hydrates is calculated at Becke97-D/6-311G** level of theory.

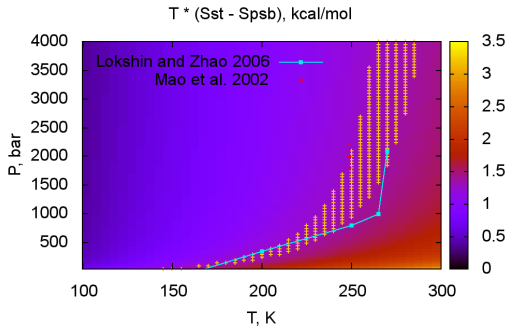

(b) $E_{HCG} \pm 5\%$ for hydrates is calculated at MP2/aug-cc-pVDZ level of theory.

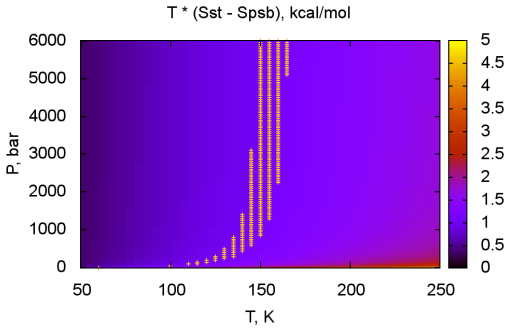

(c) $E_{HCG} \pm 5\%$ for AB clathrates is calculated at Becke97-D/6-311G** level of theory.

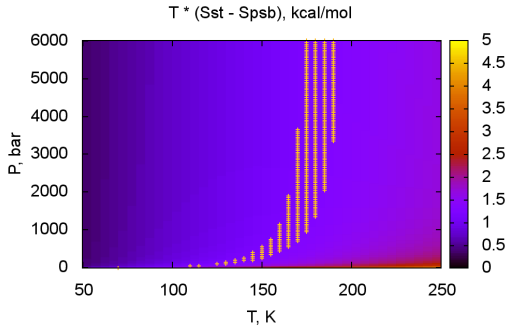

(d) $E_{HCG} \pm 5\%$ for AB clathrates is calculated at MP2/aug-cc-pVDZ level of theory.

Figure 8.11: Stability zones of H_2 clathrates calculated with more realistic potentials.

8.6 Conclusions

A statistical model of clathrates temperature-pressure phase equilibria, which is based on calculated guest-host interactions and entropy of guest molecules in spherical cages, has been developed. An application of the model to known hydrates showed quantitative agreement between experimental and theoretical data. An application of the model to hydrogen clathrates of ammonia borane shows that the pressures required for room temperature stability are practically unattainable. However, stabilization of this hypothetical material at ambient pressure could be achieved at 77 K.

Chapter 9

Summary and Conclusions

In this work a new method to store hydrogen hierarchically has been proposed and thoroughly studied. The method has been explored theoretically with Ammonia Borane (AB) as the host component of hydrogen clathrates.

On the basis of the review of hydrogen storage methodologies given in this dissertation one may conclude that storage of hydrogen in materials suffers from lack of simultaneous hydrogen accessibility and high gravimetric density. This drawback of known hydrogen storage materials could be overcome by novel hydrogen clathrates, where host molecules themselves are high density hydrogen storage materials. These hydrogen clathrates store hydrogen hierarchically at two levels. The first one is physisorbed and easily accessible molecular hydrogen and the second one is chemically bound hydrogen. This concept of hierarchical hydrogen storage has been formulated and implemented in this work in a form of hydrogen clathrates of AB.

In this study various theories and methods of computational chemistry and material science have been applied. Weak host-guest interactions have been analyzed with the aid of SAPT. The cages and periodic structures of AB clathrates have been studied within the framework of DFT. Hydrogen capacity of the clathrates has been estimated using the MP2 and the DFT-D approaches. Linear scaling DFT methods along with traditional calculation schemes have been used. In addition, we developed a model of clathrate phase equilibria, in which thermodynamic functions are determined from the properties derived from electronic structure calculations.

For hypothetical hydrogen clathrates of AB three types of cages and seven periodic structures have been identified. The screening of periodic structures with linear scaling DFT resulted in one structure, the CCH, being noticeably more stable than others. Calculations done for this structure applying an industrial standard of DFT, as implemented in the VASP code, demonstrated that the electronic structure energy per one AB molecule is lower than in the molecular crystal of AB. The empty clathrate structure remains more stable than the molecular crystal at sufficiently low temperatures (below 77 K), as *ab-initio* molecular dynamics study demonstrated. The estimated hydrogen capacity of the CCH structure of AB clathrates reaches

21 wt%, out of which 2 wt% are molecules of hydrogen enclosed in the cages.

The work has shown that the known van der Waals and Platteeuw model of hydrates phase equilibria fails for pure hydrogen hydrates due to peculiar nature of the guest molecule and thus should not be generalized to hydrogen clathrates of ammonia borane. A statistical model of clathrates phase equilibria has been proposed instead, which is based on calculated guest-host interactions, entropy of guest molecules in spherical cages, and corrections for nonideality of gases. Pressures required for room temperature hydrogen storage in clathrates of ammonia borane were found to be impractically high. However, the model predicts that clathrates of ammonia borane loaded with molecular hydrogen could be stabilized at ambient pressure by lowering temperature down to 77 K.

The reported results could be considered as a feasibility study on hydrogen clathrates of ammonia borane. Very promising and somewhat intriguing results of the dissertation might serve as a justification and a motivation for further experimental research on hydrogen clathrates of ammonia borane, which is currently in its early stage [165, 166]. Further improvement of the clathrates can be accomplished by using other guest molecules, in addition to molecular hydrogen, and/or by forming semi-clathrates that include ionic moieties in the host framework [91, 10].

Appendices

Appendix A

Cage 12 Volume Estimation

To find volume of Cage 12 we consider an irregular truncated octahedron shown in figure A.1. The volume of this irregular truncated octahedron, V_{TO}, is equal to the volume of a regular octahedron, V_{O}, minus six volumes of the pyramid V_{P}: $V_{\mathrm{TO}} = V_{\mathrm{O}} - 6V_{\mathrm{P}}$. The volume of a regular octahedron is $V_{\mathrm{O}} = 1/3\sqrt{2}\mathrm{a}^3$, with a = 2b + B-N. The volume of a pyramid is $V_{\mathrm{P}} = 1/3\mathrm{b}^2\mathrm{h}$, with $\mathrm{h} = \mathrm{b}/\sqrt{2}$. With b = 3.51 Å and B-N = 1.615 Å, see figure 6.4(c) and table 6.2, $V_{\mathrm{TO}} = 242.36$ Å^3.

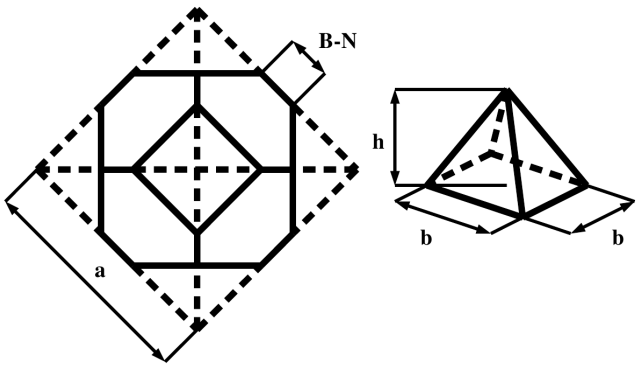

Figure A.1: Truncated octahedron constructed on heavy atoms of the Cage 12.

Appendix B

Calculation of the Free Energy From Phonon Density of States

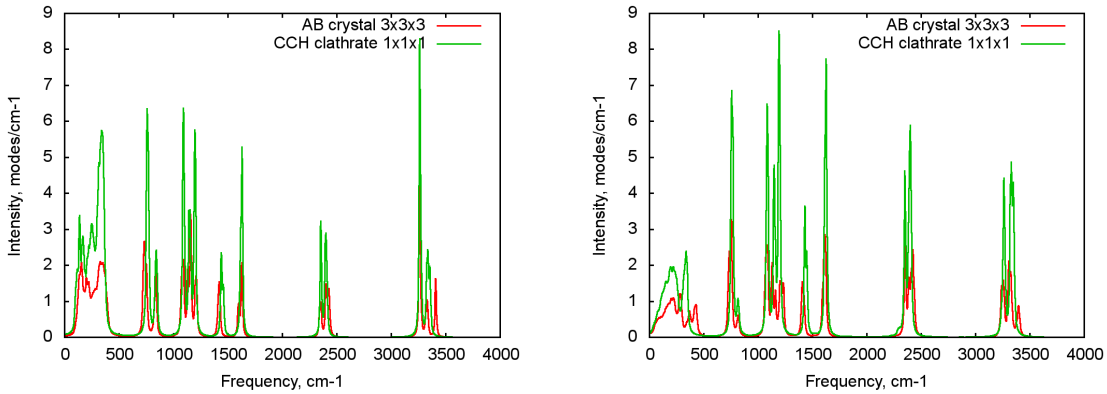

(a) Obtained from simulations done at 3 K.

(b) Obtained from simulations done at 77 K.

Figure B.1: Phonon densities of states of the CCH structure and AB molecular crystal.

Fourier transformed atomic velocity autocorrelation functions for the CCH structure and AB molecular crystal are shown in figure B.1. The free energy is calculated as follows, see for example [50] and references therein.

$$G(T) = H(T) - T \cdot S(T) \tag{B.1}$$

For solids, neglecting the pV term, the enthalpy can be written as in equation B.2.

$$H(T) = E_0 + E_{vib}(T) \tag{B.2}$$

Here, E_0 is the ground state electronic energy. Within the harmonic approximation, the vibrational contribution to enthalpy is given by equation B.3.

$$E_{vib}(T) = \frac{1}{2} m \int_0^\infty \hbar w g(w) coth\left(\frac{\hbar w}{2kT}\right) dw \tag{B.3}$$

Here, T is the temperature, m is the number of degrees of freedom, $\hbar$ is the reduced Planck's constant, w is the vibrational frequencies, $g(w)$ is the phonon density of states, and k is the Boltzmann's constant.

In the limit of zero temperature E_{vib} becomes the zero point energy, equation B.4, and the vibrational entropy is given by equation B.5.

$$E_{ZPE} = \frac{1}{2} m \int_0^\infty \hbar w g(w) dw \tag{B.4}$$

$$\begin{aligned} S(T) = mk \int_0^\infty g(w) \left(\frac{\hbar w}{2kT} \right) \left[coth \left(\frac{\hbar w}{2kT} \right) - 1 \right] - \\ - g(w) ln \left[1 - exp \left(- \frac{\hbar w}{kT} \right) \right] dw \end{aligned} \tag{B.5}$$

Appendix C

Note on Numerical Implementation of the Spherical Bessel Functions

The spherical Bessel functions used for calculations in chapter 8 were implemented according to the first term of equation 8.15. The implementation is numerically stable up to the argument value of 35 for all functions of the order 0–28, figure C.1. This covers principal quantum numbers 1–11 and angular momentum quantum numbers 0–28.

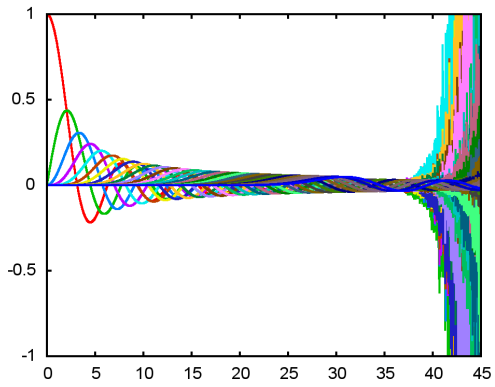

Figure C.1: The spherical Bessel functions of the order 0–28.

Appendix D

Kihara Fits to NH_3BH_3-H_2 Intermolecular Potentials

The fittings are given in figure D.1.

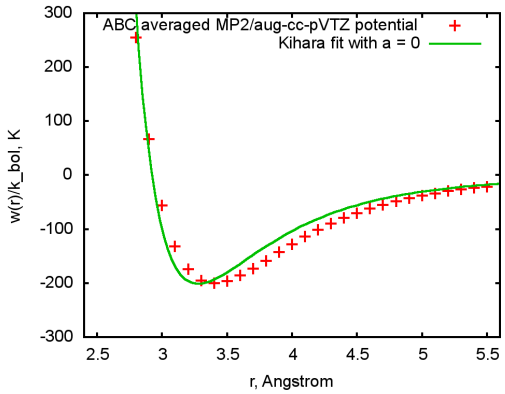

(a) Fitting of the Kihara potential to the ABC AB-H_2 MP2 averaged intermolecular potential.

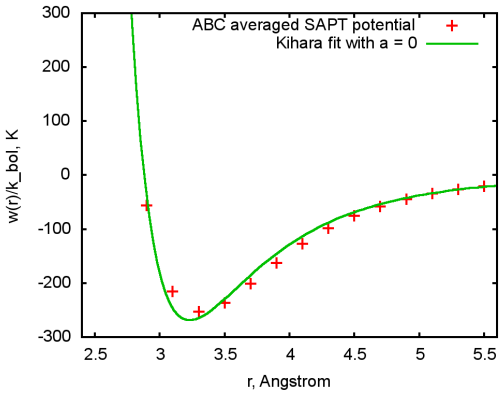

(b) Fitting of the Kihara potential to the ABC AB-H_2 SAPT averaged intermolecular potential.

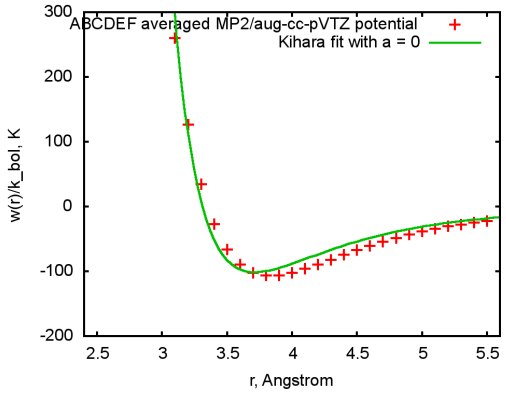

(c) Fitting of the Kihara potential to the ABC and DEF AB-H_2 MP2 averaged intermolecular potential.

Figure D.1: Kihara fits to the MP2 and the SAPT averaged potentials.

References

[1] Dunn, S. *Hydrogen Futures: Toward a Sustainable Energy System*. Worldwatch Institute, Washington DC, USA, (2001).

[2] Crabtree, G. W., Dresselhaus, M. S., and Buchanan, M. V. *Physics Today* , 39–44 December (2004).

[3] Stringer, J. and Horton, L. Basic research needs to assure a secure energy future, Oak Ridge National Laboratory, (2003). A Report for US DOE.

[4] The hydrogen, fuel cells & infrastructure technologies program. Multi-year research, development, and demonstration plan, US DOE, (2007).

[5] Gutowski, M. and Autrey, T. *Chemistry World* **3**, 44–48 (2006).

[6] Felderhoff, M., Weidenthaler, C., von Helmolt, R., and Eberle, U. *Physical Chemistry Chemical Physics* **9**, 2643–2653 (2007).

[7] Satyapal, S., Petrovic, J., Read, C., Thomas, G., and Ordaz, G. *Catalysis Today* **120**, 246–256 (2007).

[8] Bénard, P., Chahine, R., Chandonia, P., Cossement, D., Dorval-Douville, G., La, L., Lachance, P., Paggiaro, R., and Poirier, E. *Journal of Alloys and Compounds* **446-447**, 380–384 (2007). Proceedings of the International Symposium on Metal-Hydrogen Systems, Fundamentals and Applications (MH2006).

[9] Rowsell, J. L. C. and Yaghi, O. M. *Angewandte Chemie International Edition* **44**(30), 4670–4679 (2005).

[10] Struzhkin, V. V., Militzer, B., Mao, W. L., Mao, H.-k., and Hemley, R. J. *Chemical Reviews* **107**(10), 4133–4151 (2007).

[11] Zaluski, L., Zaluska, A., and Ström-Olsen, J. O. *Journal of Alloys and Compounds* **290**(1-2), 71–78 (1999).

[12] Balema, V. P., Pecharsky, V. K., and Dennis, K. W. *Journal of Alloys and Compounds* **313**(1-2), 69–74 (2000).

[13] Hanada, N., Ichikawa, T., and Fujii, H. *The Journal of Physical Chemistry B* **109**(15), 7188–7194 (2005).

[14] Marder, T. B. *Angewandte Chemie International Edition* **46**(43), 8116–8118 (2007).

[15] Stephens, F. H., Pons, V., and Baker, R. T. *Dalton Transactions* (25), 2613–2626 (2007).

[16] Klooster, W. T., Koetzle, T. F., Siegbahn, P. E. M., Richardson, T. B., and Crabtree, R. H. *Journal of the American Chemical Society* **121**(27), 6337–6343 (1999).

[17] Denney, M. C., Pons, V., Hebden, T. J., Heinekey, D. M., and Goldberg, K. I. *Journal of the American Chemical Society* **128**(37), 12048–12049 (2006).

[18] Bluhm, M. E., Bradley, M. G., Butterick, R., Kusari, U., and Sneddon, L. G. *Journal of the American Chemical Society* **128**(24), 7748–7749 (2006).

[19] Gutowska, A., Li, L., Shin, Y., Wang, C. M., Li, X. S., Linehan, J. C., Smith, R. S., Kay, B. D., Schmid, B., Shaw, W., Gutowski, M., and Autrey, T. *Angewandte Chemie International Edition* **44**(23), 3578–3582 (2005).

[20] Dyadin, Y. A., Larionov, E. G., Manakov, A. Y., Zhurko, F. V., Aladko, E. Y., Mikina, T. V., and Komarov, V. Y. *Mendeleev Communications* **5**, 209–210 (1999).

[21] Davy, H. *Philos. Trans. R. Soc. London* **101**, 155–162 (1811).

[22] Faraday, M. *Quarterly Journal of Science, Literature, and the Arts* **15**, 71–74 (1823).

[23] Dyadin, Y. A., Terekhova, I. S., Rodionova, T. V., and Soldatov, D. V. *Journal of Structural Chemistry* **40**(5), 645–653 (1999).

[24] Hammerschmidt, E. G. *Industrial and Engineering Chemistry* **26**(8), 851–855 (1934).

[25] Chatti, I., Delahaye, A., Fournaison, L., and Petitet, J.-P. *Energy Conversion and Management* **46**(9-10), 1333–1343 (2005).

[26] Powell, H. *J. Chem. Soc.* , 61–73 (1948).

[27] Chaplin, M. `http://www.lsbu.ac.uk/water/`, February (2008).

[28] Wöhler, F. *Liebigs Annalen der Chemie* **33**, 125 (1840).

[29] Wöhler, F. *Liebigs Annalen der Chemie* **69**, 297 (1849).

[30] Clemm, A. *Liebigs Annalen der Chemie* **110**, 357 (1859).

[31] Mylius, F. *Ber. Bunseng. Phys. Chem.* **19**, 999 (1886).

[32] Hofmann, K. and Küspert, K. *Z. Anorg. Allg. Chem.* **15**, 204–207 (1897).

[33] Dianin, A. *J. Russ. Phys. Chem. Soc.* **43**, 141 (1911).

[34] Dianin, A. *J. Russ. Phys. Chem. Soc.* **46**, 1310 (1914).

[35] Leung, W. B., March, N. H., and Motz, H. *Physics Letters* **56A**(6), 425–426 (1976).

[36] von Helmolt, R. and Eberle, U. *Journal of Power Sources* **165**, 833–843 (2007).

[37] DOE hydrogen program: Annual progress report – storage, US DOE, (2007).

[38] DOE hydrogen program: Annual progress report – storage, US DOE, (2005).

[39] Ahluwalia, R. and Peng, J. *International Journal of Hydrogen Energy* **33**(17), 4622–4633 (2008).

[40] Reilly, J. J. and Wiswall, R. H. *Inorganic Chemistry* **13**(1), 218–222 (1974).

[41] Noreus, D., Olsson, L. G., and Werner, P.-E. *Journal of Physics F: Metal Physics* **13**(4), 715–727 (1983).

[42] Los Alamos National Laboratory. `http://periodic.lanl.gov/default.htm`, April (2009).

[43] Bogdanović, B. and Schwickardi, M. *Journal of Alloys and Compounds* **253-254**, 1–9 (1997).

[44] Bogdanović, B. and Schwickardi, M. *Applied Physics A: Materials Science & Processing* **72**(2), 221–223 (2001).

[45] Ingersoll, J., Mani, N., Thenmozhiyal, J., and Muthaiah, A. *Journal of Power Sources* **173**(1), 450–457 (2007).

[46] Marrero-Alfonso, E. Y., Gray, J. R., Davis, T. A., and Matthews, M. A. *International Journal of Hydrogen Energy* **32**(18), 4717–4722 (2007).

[47] Vajo, J. J., Skeith, S. L., and Mertens, F. *The Journal of Physical Chemistry B* **109**(9), 3719–3722 (2005).

[48] Sandrock, G., Reilly, J., Graetz, J., Zhou, W.-M., Johnson, J., and Wegrzyn, J. *Applied Physics A: Materials Science & Processing* **80**(4), 687–690 (2005).

[49] Matus, M. H., Anderson, K. D., Camaioni, D. M., Autrey, S. T., and Dixon, D. A. *The Journal of Physical Chemistry A* **111**(20), 4411–4421 (2007).

[50] Miranda, C. R. and Ceder, G. *The Journal of Chemical Physics* **126**(18), 184703 (2007).

[51] Dixon, D. A. and Gutowski, M. *The Journal of Physical Chemistry A* **109**(23), 5129–5135 (2005).

[52] Cooper, A. C., Campbell, K. M., and Pez, G. P. 16th World Hydrogen Energy Conference, Lyon, France, June (2006).

[53] Sotoodeh, F. and Smith, K. J. *Industrial and Engineering Chemistry Research* (2009).

[54] Thomas, K. M. *Catalysis Today* **120**(3-4), 389–398 (2007).

[55] Nijkamp, M., Raaymakers, J., van Dillen, A., and de Jong, K. *Applied Physics A: Materials Science & Processing* **72**(5), 619–623 (2001).

[56] Hirscher, M., Becher, M., Haluska, M., Dettlaff-Weglikowska, U., Quintel, A., Duesberg, G. S., Choi, Y.-M., Downes, P., Hulman, M., Roth, S., Stepanek, I., and Berneir, P. *Applied Physics A: Materials Science & Processing* **72**(2), 129–132 (2001).

[57] Park, N., Hong, S., Kim, G., and Jhi, S.-H. *Journal of the American Chemical Society* **129**(29), 8999–9003 (2007).

[58] Patchkovskii, S., Tse, J. S., Yurchenko, S. N., Zhechkov, L., Heine, T., and Seifert, G. *Proceedings of the National Academy of Sciences of the United States of America* **102**(30), 10439–10444 (2005).

[59] Lin, X., Jia, J., Zhao, X., Thomas, K. M., J. Blake, A., Walker, G. S., Champness, N. R., Hubberstey, P., and Schröder, M. *Angewandte Chemie International Edition* **45**(44), 7358–7364 (2006).

[60] Lin, X., Telepeni, I., Blake, A. J., Dailly, A., Brown, C. M., Simmons, J. M., Zoppi, M., Walker, G. S., Thomas, K. M., Mays, T. J., Hubberstey, P., Champness, N. R., and Schröder, M. *Journal of the American Chemical Society* **131**(6), 2159–2171 (2009).

[61] Appl, M. *Ammonia: Principles and Industrial Practice*. WILEY-VCH, Weinheim, Germany, (1999).

[62] Klerke, A., Christensen, C. H., Norskov, J. K., and Vegge, T. *Journal of Materials Chemistry* **18**(20), 2304–2310 (2008).

[63] Christensen, C. H., Sorensen, R. Z., Johannessen, T., Quaade, U. J., Honkala, K., Elmoe, T. D., Kohler, R., and Norskov, J. K. *Journal of Materials Chemistry* **15**(38), 4106–4108 (2005).

[64] Chen, P., Xiong, Z., Luo, J., Lin, J., and Tan, K. L. *Nature* **420**, 302–304 (2002).

[65] Luo, W. *Journal of Alloys and Compounds* **381**(1-2), 284–287 (2004).

[66] Welch, G. C., Juan, R. R. S., Masuda, J. D., and Stephan, D. W. *Science* **314**(5802), 1124–1126 (2006).

[67] Lee, H., Choi, W. I., and Ihm, J. *Physical Review Letters* **97**(5), 056104 (2006).

[68] Li, S. and Jena, P. *Physical Review Letters* **97**(20), 209601 (2006).

[69] Davies, J. E. D. *Journal of Inclusion Phenomena and Macrocyclic Chemistry* **32**(4), 499–504 (1998).

[70] Dyadin, Y. A. and Guschin, A. L. *Soros Educational Journal* **6**(12), 40–47 (2000).

[71] Atwood, J. L. and Steed, J. W. *Encyclopedia of supramolecular chemistry.* CRC Press, (2004).

[72] Nishikiori, S.-i. and Iwamoto, T. *Chemistry Letters* **13**(3), 319–322 (1984).

[73] Imashiro, F., Yoshimura, M., and Fujiwara, T. *Acta Crystallographica* **C54**, 1357–1360 (1998).

[74] Selbo, J. G., Desper, J. M., and Eckhardt, C. J. *Journal of Inclusion Phenomena and Macrocyclic Chemistry* **45**(1-2), 73–78 (2003).

[75] Zakrzewski, M. and White, M. A. *J. Phys.: Condens. Matter* (3), 6703–6714 (1991).

[76] Claussen, W. F. *J. Chem. Phys.* **19**, 259, 662, 1425 (1951).

[77] Stackelberg, M. v. and Müller, H. R. *J. Chem. Phys.* **19**, 1319–1320 (1951).

[78] Pauling, L. and Marsh, R. E. *Proceedings of the National Academy of Sciences of the United States of America* **38**(2), 112–118 (1952).

[79] Bernal, J. D. and Fowler, R. H. *The Journal of Chemical Physics* **1**(8), 515–548 (1933).

[80] Pauling, L. *Journal of the American Chemical Society* **57**(12), 2680–2684 (1935).

[81] Kuhs, W. F., Chazallon, B., Radaelli, P. G., and Pauer, F. *Journal of Inclusion Phenomena and Macrocyclic Chemistry* **29**(1), 65–77 (1997).

[82] Mao, W. L., Mao, H.-k., Goncharov, A. F., Struzhkin, V. V., Guo, Q., Hu, J., Shu, J., Hemley, R. J., Somayazulu, M., and Zhao, Y. *Science* **297**(5590), 2247–2249 (2002).

[83] Lokshin, K. A. and Zhao, Y. *Los Alamos Science* (30), 138–145 (2006).

[84] Iro, N., Gautier, D., Hersant, F., Bockelée-Morvan, D., and Lunine, J. I. *Icarus* **161**(2), 511–532 (2003).

[85] Kieffer, S. W., Lu, X., Bethke, C. M., Spencer, J. R., Marshak, S., and Navrotsky, A. *Science* **314**(5806), 1764–1766 (2006).

[86] Miller, S. L. and Smythe, W. D. *Science* **170**(3957), 531–533 (1970).

[87] Tohidi, B. and Anderson, R. *Teaching Earth Sciences* **29**(3/4), 18–21 (2004).

[88] Bohrmann, G. and Torres, M. E. *Gas hydrates in marine sediments, In H.D. Schulz and M. Zabel Marine Geochemistry.* Springer, 2nd edition, (2000).

[89] Dutch, S. `http://www.uwgb.edu/dutchs/PETROLGY/Clathrate-0.HTM`, February (2008).

[90] Sloan, E. D. and Koh, C. A. *Clathrate Hydrates of Natural Gases.* CRC Press, 3rd edition, (2008).

[91] Anderson, R., Chapoy, A., and Tohidi, B. *Langmuir* **23**(6), 3440–3444 (2007).

[92] Chapoy, A., Anderson, R., and Tohidi, B. *Journal of the American Chemical Society* **129**(4), 746–747 (2007).

[93] Kim, D.-Y. and Lee, H. *Journal of the American Chemical Society* **127**(28), 9996–9997 (2005).

[94] Strobel, T. A., Koh, C. A., and Sloan, E. D. *The Journal of Physical Chemistry B* **112**(7), 1885–1887 (2008).

[95] Patchkovskii, S. and Tse, J. S. *Proceedings of the National Academy of Sciences of the United States of America* **100**(25), 14645–14650 (2003).

[96] Patchkovskii, S. and Yurchenko, S. N. *Physical Chemistry Chemical Physics* **6**(16), 4152–4155 (2004).

[97] Sluiter, M. H., Adachi, H., Belosludov, R. V., Belosludov, V. R., and Kawazoe, Y. *Materials Transactions* **45**(5), 1452–1454 (2004).

[98] Inerbaev, T. M., Belosludov, V. R., Belosludov, R. V., Sluiter, M., and Kawazoe, Y. *Computational Materials Science* **36**(1-2), 229–233 (2006).

[99] Alavi, S., Ripmeester, J. A., and Klug, D. D. *The Journal of Chemical Physics* **123**(2), 024507 (2005).

[100] Xu, M., Elmatad, Y. S., Sebastianelli, F., Moskowitz, J. W., and Bačić, Z. *The Journal of Physical Chemistry B* **110**(49), 24806–24811 (2006).

[101] Xu, M., Sebastianelli, F., and Bačić, Z. *The Journal of Physical Chemistry A* **111**(49), 12763–12771 (2007).

[102] Sebastianelli, F., Xu, M., Kanan, D. K., and Bačić, Z. *The Journal of Physical Chemistry A* **111**(28), 6115–6121 (2007).

[103] van der Waals, J. H. and Platteeuw, J. C. *Advances in Chemical Physics* **2**, 1–57 (1959).

[104] McKoy, V. and Sinanoğlu, O. *The Journal of Chemical Physics* **38**(12), 2946–2956 (1963).

[105] Strobel, T. A., Koh, C. A., and Sloan, E. D. *Fluid Phase Equilibria* **280**(1-2), 61–67 (2009).

[106] Parrish, W. R. and Prausnitz, J. M. *Industrial and Engineering Chemistry Process Design and Development* **11**(1), 26–35 (1972).

[107] Sloan, E. D. *Clathrate Hydrates of Natural Gases*. Marcel Dekker, New York, 2nd edition, (1998).

[108] Sandler, S. I. *Chemical and Engineering Thermodynamics*. Wiley, 3rd edition, (1999).

[109] Pomeransky, A. A. and Belosludov, V. R. *Advances in the Study of Gas Hydrates edited by Charles E. Taylor and Jonathan T. Kwan*. Springer, (2004).

[110] Handa, Y. P. *The Journal of Chemical Thermodynamics* **18**(10), 915–921 (1986).

[111] Doltsinis, N. L. and Marx, D. *Journal of Theoretical and Computational Chemistry* **1**(2), 319–349 (2002).

[112] Piela, L. *Ideas of Quantum Chemistry*. Elsevier, (2007).

[113] Jensen, F. *Introduction to Computational Chemistry*. Wiley, (1999).

[114] Hohenberg, P. and Kohn, W. *Phys. Rev.* **136**(3B), B864–B871 Nov (1964).

[115] Kohn, W. and Sham, L. J. *Phys. Rev.* **140**(4A), A1133–A1138 Nov (1965).

[116] Postnikov, A. `http://www.home.uni-osnabrueck.de/apostnik/lectures.html`, August (2009). Lectures on the Density Functional Theory.

[117] Gill, P. M. W. *Encyclopedia of Computational Chemistry, Vol. 1, John Wiley and Sons* **1**, 678–689 (1998).

[118] Parr, R. G. and Weitao, Y. *Density-Functional Theory of Atoms and Molecules*. Oxford University Press, (1989).

[119] Grimme, S. *Journal of Computational Chemistry* **25**(12), 1463–1473 (2004).

[120] Grimme, S. *Journal of Computational Chemistry* **27**(15), 1787–1799 (2006).

[121] Myers, H. P. *Introductory Solid State Physics*. Taylor & Francis, (1990).

[122] Payne, M. C., Teter, M. P., Allan, D. C., Arias, T. A., and Joannopoulos, J. D. *Rev. Mod. Phys.* **64**(4), 1045–1097 Oct (1992).

[123] Møller, C. and Plesset, M. S. *Phys. Rev.* **46**(7), 618–622 Oct (1934).

[124] Bartlett, R. J. *The Journal of Physical Chemistry* **93**, 1697–1708 (1989).

[125] Bartlett, R. J. and Musiał, M. *Reviews of Modern Physics* **79**(1), 291–352 (2007).

[126] Jeziorski, B., Moszynski, R., and Szalewicz, K. *Chemical Reviews* **94**(7), 1887–1930 (1994).

[127] Patkowski, K., Szalewicz, K., and Jeziorski, B. *The Journal of Chemical Physics* **125**(15), 154107 (2006).

[128] Kohn, W. *Phys. Rev. Lett.* **76**(17), 3168–3171 Apr (1996).

[129] Soler, J. M., Artacho, E., Gale, J. D., Garcia, A., Junquera, J., Ordejon, P., and Sanchez-Portal, D. *Journal of Physics: Condensed Matter* **14**(11), 2745–2779 (2002).

[130] Sánchez-Portal, D., Ordejón, P., Artacho, E., and Soler, J. M. *International Journal of Quantum Chemistry* **65**(5), 453–461 (1997).

[131] Bowden, M. E., Gainsford, G. J., and Robinson, W. T. *Australian Journal of Chemistry* **60**, 149–153 (2007).

[132] Xantheas, S. S. and Dunning Jr., T. H. *The Journal of Chemical Physics* **99**(11), 8774–8792 (1993).

[133] Gutowski, M., Bachorz, R., Autrey, T., and Linehan, J. *Prepr. Pap.-Am. Chem. Soc., Div. Fuel Chem.* **50**(2), 496–498 (2005).

[134] Jeziorska, M. g., Cencek, W., Patkowski, K., Jeziorski, B., and Szalewicz, K. *The Journal of Chemical Physics* **127**(12), 124303 (2007).

[135] Cybulski, H. and Sadlej, J. *Journal of Chemical Theory and Computation* **4**(6), 892–897 (2008).

[136] Becke, A. D. *The Journal of Chemical Physics* **98**(7), 5648–5652 (1993).

[137] Lee, C., Yang, W., and Parr, R. G. *Phys. Rev. B* **37**(2), 785–789 Jan (1988).

[138] Vosko, S. H., Wilk, L., and Nusair, M. *Canadian Journal of Physics* **58**, 1200–1211 (1980).

[139] Stephens, P. J., Devlin, F. J., Chabalowski, C. F., and Frisch, M. J. *The Journal of Physical Chemistry* **98**(45), 11623–11627 (1994).

[140] Becke, A. D. *Phys. Rev. A* **38**(6), 3098–3100 Sep (1988).

[141] Perdew, J. P. *Phys. Rev. B* **33**(12), 8822–8824 Jun (1986).

[142] Perdew, J. P., Burke, K., and Ernzerhof, M. *Phys. Rev. Lett.* **77**(18), 3865–3868 Oct (1996).

[143] Weisstein, E. W. `http://mathworld.wolfram.com/`, September (2009). `http://mathworld.wolfram.com/ArchimedeanSolid.html`.

[144] Frisch, M. J., Trucks, G. W., Schlegel, H. B., Scuseria, G. E., Robb, M. A., Cheeseman, J. R., Montgomery, J. A., Vreven, T., Kudin, K. N., Burant, J. C., Millam, J. M., Iyengar, S. S., Tomasi, J., Barone, V., Mennucci, B., Cossi, M., Scalmani, G., Rega, N., Petersson, G. A., Nakatsuji, H., Hada, M., Ehara, M., Toyota, K., Fukuda, R., Hasegawa, J., Ishida, M., Nakajima, T., Honda, Y., Kitao, O., Nakai, H., Klene, M., Li, X., Knox, J. E., Hratchian, H. P., Cross, J. B., Bakken, V., Adamo, C., Jaramillo, J., Gomperts, R., Stratmann, R. E., Yazyev, O., Austin, A. J., Cammi, R., Pomelli, C., Ochterski, J. W., Ayala, P. Y., Morokuma, K., Voth, G. A., Salvador, P., Dannenberg, J. J., Zakrzewski, V. G., Dapprich, S., Daniels, A. D., Strain, M. C., Farkas, O., Malick, D. K., Rabuck, A. D., Raghavachari, K., Foresman, J. B., Ortiz, J. V., Cui, Q., Baboul, A. G., Clifford, S., Cioslowski, J., Stefanov, B. B., Liu, G., Liashenko, A., Piskorz, P., Komaromi, I., Martin, R. L., Fox, D. J., Keith, T., Al-Laham, M. A., Peng, C. Y., Nanayakkara, A., Challacombe, M., Gill, P. M. W., Johnson, B., Chen, W., Wong, M. W., Gonzalez, C., and Pople, J. A. Gaussian 03, Revision D.01, Gaussian, Inc., Wallingford CT, USA, (2004).

[145] Bylaska, E. J., de Jong, W. A., Govind, N., Kowalski, K., Straatsma, T. P., Valiev, M., Wang, D., Apra, E., Windus, T. L., Hammond, J., Nichols, P., Hirata, S., Hackler, M. T., Zhao, Y., Fan, P.-D., Harrison, R. J., Dupuis, M., Smith, D. M. A., Nieplocha, J., Tipparaju, V., Krishnan, M., Wu, Q., Van Voorhis, T., Auer, A. A., Nooijen, M., Brown, E., Cisneros, G., Fann,

G. I., Fruchtl, H., Garza, J., Hirao, K., Kendall, R., Nichols, J. A., Tsemekhman, K., Wolinski, K., Anchell, J., Bernholdt, D., Borowski, P., Clark, T., Clerc, D., Dachsel, H., Deegan, M., Dyall, K., Elwood, D., Glendening, E., Gutowski, M., Hess, A., Jaffe, J., Johnson, B., Ju, J., Kobayashi, R., Kutteh, R., Lin, Z., Littlefield, R., Long, X., Meng, B., Nakajima, T., Niu, S., Pollack, L., Rosing, M., Sandrone, G., Stave, M., Taylor, H., Thomas, G., van Lenthe, J., Wong, A., and Zhang, Z. "NWChem, A Computational Chemistry Package for Parallel Computers, Version 5.1", Pacific Northwest National Laboratory, Richland, Washington 99352-0999, USA, (2007).

[146] Grünbaum, B. *Geombinatorics* (4), 49–56 (1994).

[147] Kresse, G. and Hafner, J. *Phys. Rev. B* **47**(1), 558–561 Jan (1993).

[148] Kresse, G. and Hafner, J. *Phys. Rev. B* **49**(20), 14251–14269 May (1994).

[149] Kresse, G. and Furthmüller, J. *Computational Materials Science* **6**(1), 15–50 (1996).

[150] Kresse, G. and Furthmüller, J. *Phys. Rev. B* **54**(16), 11169–11186 Oct (1996).

[151] Blöchl, P. E. *Phys. Rev. B* **50**(24), 17953–17979 Dec (1994).

[152] Kresse, G. and Joubert, D. *Phys. Rev. B* **59**(3), 1758–1775 Jan (1999).

[153] Lippert, G., Hutter, J., and Parrinello, M. *Theoretical Chemistry Accounts: Theory, Computation, and Modeling (Theoretica Chimica Acta)* **103**(2), 124–140 (1999).

[154] Laino, T., Mohamed, F., Laio, A., and Parrinello, M. *Journal of Chemical Theory and Computation* **1**(6), 1176–1184 (2005).

[155] Laino, T., Mohamed, F., Laio, A., and Parrinello, M. *Journal of Chemical Theory and Computation* **2**(5), 1370–1378 (2006).

[156] Atkins, P. and de Paula, J. *Atkins' Physical Chemistry.* Oxford, 8th edition, (2006).

[157] Davydov, A. S. *Quantum Mechanics.* Pergamon Press, (1965).

[158] Weisstein, E. W. `http://mathworld.wolfram.com/`, June (2009). `http://mathworld.wolfram.com/SphericalBesselFunctionoftheFirstKind.html`.

[159] Abramowitz, M. and Stegun, I. A. *Handbook of Mathematical Functions with Formulas, Graphs, and Mathematical Tables.* Dover, (1972).

[160] Diaz Peña, M., Pando, C., and Renuncio, J. A. R. *The Journal of Chemical Physics* **76**(1), 325–332 (1982).

[161] Nakamura, T., Makino, T., Sugahara, T., and Ohgaki, K. *Chemical Engineering Science* **58**(2), 269–273 (2003).

[162] Anderson, B. J., Tester, J. W., and Trout, B. L. *The Journal of Physical Chemistry B* **108**(48), 18705–18715 (2004).

[163] Sugahara, K., Tanaka, Y., Sugahara, T., and Ohgaki, K. *Journal of Supramolecular Chemistry* **2**(4-5), 365–368 (2002).

[164] Quiroz González, J. L. M. and Thompson, D. *Comput. Phys.* **11**(5), 514–515 (1997).

[165] Lin, Y., Mao, W. L., and Mao, H.-k. *Proceedings of the National Academy of Sciences* **106**(20), 8113–8116 (2009).

[166] Chellappa, R. S., Somayazulu, M., Struzhkin, V. V., Autrey, T., and Hemley, R. J. *The Journal of Chemical Physics* **131**(22), 224515 (2009).